UNIVERSITÀ DEGLI STUDI DI MILANO

Scuola di Dottorato in Fisica, Astrofisica e Fisica Applicata

Dipartimento di Fisica

Corso di Dottorato in Fisica, Astrofisica e Fisica Applicata

Ciclo XXXI

Microstructure and connectivity of the cerebellum with advanced diffusion MRI in health and pathology

Settore Scientifico Disciplinare FIS/07

Supervisore: Prof. Alessandro LASCIALFARI

Co-supervisore: Prof. Claudia A. M. GANDINI WHEELER-KINGSHOTT

Coordinatore: Prof. Francesco RAGUSA

Tesi di Dottorato di:

Giovanni SAVINI

Anno Accademico 2017/2018

External referees:

Michela TOSETTI, IRCCS Stella Maris Scientific Institute, Pisa, Italy

Nico PAPINUTTO, University of California San Francisco, San Francisco, CA, USA

Commission of the final examination:

Prof. Giuseppe BASELLI, Politecnico di Milano, Milano, Italy

Prof. Alessandra BERTOLDO, Università di Padova, Padova, Italy

Prof. Pasquina MARZOLA, Università di Verona, Verona, Italy

Final examination:

16th January 2019
Università degli Studi di Milano, Dipartimento di Fisica, Milano, Italy

Alla mia famiglia,
quella "vecchia" e quella "nuova"

Contents

List of Acronyms

AD	axial diffusivity
AK	axial kurtosis
BOLD	blood oxigenation level dependent
BPF	brain parenchymal fraction
BW	bandwidth
CBL-DMN	extended cerebellum-DMN network
CIMS	cognitively impaired MS patients
CNS	central nervous system
CO-ZOOM	contiguous-slice zonally oblique multislice
CPMS	cognitively preserved MS patients
CSD	constrained spherical deconvolution
CSF	cerebro spinal fluid
DCN	deep cerebellar nuclei
DCS	device coordinate system
DKI	diffusional kurtosis imaging
DMN	default mode network
dMRI	diffusion MRI
DTI	diffusion tensor imaging
EDSS	expanded disability status scale
EPI	echo planar imaging
FA	fractional anisotropy
FLAIR	fluid-attenuated inversion recovery
fMRI	functional MRI
FOV	field-of-view
FWHM	full width at half maximum
GE	global efficiency
GM	grey matter
GRE	gradient echo
HADS-D	hospital anxiety and depression scale - depression
HC	healthy control
HCP	Human Connectome Project
IV	inner volume
LCS	logical coordinate system
MB	multi-band
MD	mean diffusivity
MK	mean kurtosis
MNI	Montreal Neurological Institute
MRI	magnetic resonance imaging
MS	multiple sclerosis
NART	national adult reading test
NAWM	normal-appearing white

	matter
PD	proton density
PE	phase encoding
PP	primary progressive
PPF	phase partial fourier
RD	radial diffusivity
RF	radio frequency
RK	radial kurtosis
RO	readout
ROI	region of interest
RR	relapsing-remitting
SAR	specific absorption rate
SDMT	symbol digit modalities test
SE	spin echo
SMS	simultaneous multi-slice
SNR	signal-to-noise ratio
SP	secondary progressive
SS	slice selection
T1w	T_1-weighted
T2w	T_2-weighted
TB	transition band
TBW	time-bandwidth product
TDI	track density image
TE	echo time
TR	repetition time
UHF	ultra-high field
UI	user interface
WM	white matter
WM-FA	WM mean FA
WM-LL	WM lesion load
ZCS	zoom coordinate system
ZOOM	zonally-magnified oblique multislice

Introduction

The cerebellum contains the majority of the central nervous system (CNS) neurons, but despite this it has often been considered secondary to the brain in many respects. From a functional point of view, while brain functional topography has been extensively studied, the cerebellum is classically known to be a key region mainly supporting sensorimotor coordination and learning. However, in the last two decades its role in higher cognitive functions has been increasingly recognised, thus raising the interest of neuroscience and neuroimaging communities. Nowadays we think of the cerebellum as a powerful processing machine, which is organised in subunits that are connected to many specific nuclei and brain cortical regions and which is involved in different, spatially partially segregated, functional loops. Despite this, knowledge about cerebellar structure and function is still incomplete and the interpretation of experimental results often represents a hard task. For these and other technical reasons the cerebellum is still frequently disregarded in magnetic resonance imaging (MRI) studies: the size of its substructures and its proximity to noise sources, like large blood vessels and the oral cavity, limit the applicability and effectiveness of standard MRI acquisition techniques.

Therefore, the principal aim of this work was to use MRI to investigate cerebellar microstructure and macrostructural connectivity in health and pathology, focusing also on technical aspects of image acquisition. The cerebellum can represent a real challenge for current MRI analysis pipelines and acquisition techniques and, as a consequence, the starting point of each project described in the present thesis were techniques, models and sequences currently accepted in clinical practice. The meeting of inadequacies or problems of such techniques raised questions that pushed research to a more fundamental level.

This thesis has three main contributions. It starts with a clinical study of cerebellar involvement in processing speed deficits in Multiple Sclerosis (MS), highlighting the importance of the cerebellum for the well-being of subjects; then a deeper investigation of the cerebellar microstructure is performed to contribute to the understanding of this part of the brain; finally, the emerging technical problems that hamper the study of small structures within the cerebellum are tackled by developing dedicated acquisition methods.

In detail, in Chap. 1, given the cerebellar involvement in cognition and experimental evidences of its functional connectivity with brain cortical regions associated with the default mode network (DMN), a study of connectomics is presented. Here, cerebellar structural connectivity with DMN regions is reconstructed in patients affected by multiple sclerosis (MS) and healthy controls using diffusion MRI (dMRI) and tractography to evaluate the role of the cerebellum in information processing speed, which is considered one of the cognitive domains most frequently impaired in MS. This work has been submitted for publication in a special topic on the cerebellum in Frontiers in Cellular Neuroscience and is undergoing reviews. Part of this work was selected for an oral presentation at the 7^{th} Annual Meeting of the International Society for Magnetic Resonance in Medicine (ISMRM) Italian Chapter (Bologna, Italy 2016) and for an oral presentation at the ISMRM 24th Annual Meeting & Exhibition (Singapore 2016).

Studies of cerebellar histology, physiology, cellular morphology and molecular expression have reported the existence of microstructural inhomogeneities in the cerebellar cortex, which, until now, has always been considered uniform from a cyto-architectonic point of view. On the basis of these pieces of evidence I therefore investigated the microstructure of the cerebellum as described in Chap. 2. The aim of the study was to assess whether the sensitivity of a high quality $3\,\mathrm{T}$ MRI protocol, which included T_1-weighted (T1w), T_2-weighted (T2w) and diffusion sequences, was sufficient to detect significant differences in cyto-architecture between subregions of the cerebellar cortex, possibly related to the findings reported in histological studies. This work was presented at the School of Brain Cells and Circuits 2016 course[1], specific on the cerebellum (Erice, Italy) and it was selected for an oral presentation at the ISMRM 25th Annual Meeting & Exhibition (Honolulu, Hawai'i, USA 2017).

Starting from the technical limitations found in the study of cerebellar microstructure in terms of spatial resolution, which is not suited for the small size of cerebellar substructures, and distortions of echo planar imaging (EPI) images caused by the existence of magnetic susceptibility gradients in the proximity of the cerebellum, a reduced field-of-view (FOV) approach was implemented for diffusion and functional imaging of small structures of the CNS. Chap. 3 describes the implementation of ZOOM and CO-ZOOM EPI sequences for diffusion and functional imaging at $3\,\mathrm{T}$ and $7\,\mathrm{T}$ scanners, focusing on advantages and limitations of such acquisition strategies in relation to the target of the study. Preliminary results acquired in the cerebellum and the brainstem are reported. The brainstem data was presented in poster format at the Joint Annual Meeting ISMRM-ESMRMB 2018 (Paris, France).

Each chapter is self-contained. However, in App. A a brief overview about the cerebellum is provided to serve as reference for cerebellar anatomy, cyto-architecture and connectivity.

[1] http://www.erice-golgi.org/index.php/courses/previous-courses/programme-2016-edited/

CHAPTER 1

Cerebro-cerebellar connectivity with the default mode network in multiple sclerosis

The cerebellum has always been considered an organ underlying motor control and sensory systems only. However, in recent years consensus is being built on its role in cognition. Cerebellar involvement in neurological and psychiatric conditions like Alzheimer and Parkinson disease and autism has been proved and it was shown that MS lesions in cerebellum and in cortico-cerebellar pathways can result in cognitive deficits. Therefore, in this chapter we demonstrate why it is important to study the cerebellum in the first place by using standard methods in a clinical study of MS. Then, in subsequent chapters we go into details of the cerebellar microstructure 2 and of ways to sample the signal by manipulating pulse sequences that drive the scanner 3. This study has been submitted as a journal paper to Frontiers in Cellular Neuroscience as part of a special topic on the cerebellum.

dMRI can be used to probe the microstructure of neuronal tissue and this can be applied to the study of neurological conditions. Here, we focus on MS, a demyelinating disease of the CNS, which alters the tissue microstructural features. In this study we aim to assess the importance of cerebellar connectivity to the DMN in explaining cognitive clinical scores. This network underlies one of MS core cognitive deficits, information processing speed, which is commonly assessed by administering neuropsychological tests. The purpose of this study is to investigate whether the structural substrate of network derangement as measured by dMRI is associated with clinical outcome in MS-related cognitive impairment. In particular, we analyse the role of the cerebellum in cognitive processing deficit in MS.

1.1 Multiple sclerosis

Multiple sclerosis (MS) is a demyelinating and inflammatory disease of the CNS that leads to neurodegeneration. It is the most frequent non-traumatic cause of permanent neurological disability in young adults (Inglese, 2006). It is believed to be an immune-mediated disorder and that genetic factors and infectious agents may increase the risk of contracting it, but its cause remains unknown.

The clinical course of the disease is important for prognosis and treatment decision, but a definitive cure for MS is not known yet. In most cases (80-85%) the disease onset is

characterised by an acute neurological episode. It is commonly followed by periods of remission of variable duration and by relapses, whose moment of occurrence is unpredictable. During remission periods there is no sign of disease progression and neurological deficits occurring during relapses may even resolve. This relapsing-remitting (RR) phenotype usually evolves to a secondary progressive (SP) form, where progression of disability is observed also between relapses. If progressive neurological decline occurs also after the initial episodes the phenotype is defined primary progressive (PP) MS (Lublin & Reingold, 1996).

MS pathology is characterised by disruptions in the blood-brain barrier, which allow the infiltration of immune cells (T cells, or T lymphocytes). These cells attack the axonal myelin sheaths (which can be partially or completely lost), thus leading to inflammation, gliosis and formation of glial scars (or plaques) and to axonal loss. Myelin is an insulating lipid-rich substance that surrounds cell axons. Its main function is to speed up the transmission of electrical signals (action potentials) along the axons, thus reducing the communication time between regions of the nervous system. Therefore, MS pathology has the effect of reducing signal conduction, which can be lost. Remyelination have been shown to take place after attacks, but repeated relapses make this process less effective.

The resulting symptoms depend on lesion location and on the function of affected neurons. Most common symptoms include motor, sensory and visual deficits. However, it has been found that cognition is also affected in about 50% of MS patients (Chiaravalloti & DeLuca, 2008; Dineen et al., 2009; Hulst et al., 2013).

Diagnosis is based on a combination of clinical evaluation of signs and symptoms, laboratory analysis and medical imaging. MRI is now widely employed to diagnose MS, to monitor its progression, to test treatment effectiveness (also in clinical trials), to investigate disease mechanisms and to link them with emerging dysfunction. The confluence of demyelinated lesions in white and grey matter is visible on conventional T2w, T1w and fluid-attenuated inversion recovery (FLAIR) images used in clinical practice. However, it has been shown that damage occurs also outside visible lesions, in normal appearing tissue. dMRI has been shown to be sensitive to the microstructural alteration of neuronal tissue induced by MS pathology.

1.1.1 Information processing speed

Cognitive information processing (*i.e.* the ability to store and manipulate information for short periods of time) is considered one of the most frequently affected cognitive domains in MS (Inglese, 2006).

From a clinical point of view, information processing speed performance can be assessed by administering neuropsychological tests. In particular, the symbol digit modalities test (SDMT) (Smith, 1982) is increasingly used in clinical practice because of its ease and speed of administration. It has been shown to discriminate MS patients and healthy controls (HCs) better than other cognitive measures (Benedict et al., 2017; Strober et al., 2009). Moreover, it proved to be a sensitive measure of general cognitive impairment in MS: it has been proposed as a screening test showing up to 91% sensitivity and 60% specificity to cognitive impairment (Van Schependom et al., 2014; Parmenter et al., 2007).

Finally, it is also appreciated because it shows the strongest correlation with MRI measures (Benedict et al., 2017; Stankiewicz et al., 2011; Christodoulou et al., 2003; Rao et al., 2014).

From a functional point of view, information processing speed has been linked to activity in the DMN (Forn et al., 2013; Rocca et al., 2010; Sumowski et al., 2010; Bonavita et al., 2015), which deactivates when cognitively demanding tasks are performed (Broyd et al., 2009; Buckner et al., 2008). In Sec. 1.2 we provide a description of the DMN and focus on the importance of related cortico-cerebellar pathways.

1.2 Brain networks and graph theory

The brain is made of neurons that transmit information to each other in the form of electrical signals. Therefore, it can be convenient to represent the brain as a network.

Graph theory is a mathematical framework that studies the properties of networks and it has been adopted to the study the brain. A network is defined by a number of nodes and edges (or links), which can be respectively thought as the processing units of the brain and the wiring connecting them. Nodes and edges make the connectivity matrix of the network, which is used to compute metrics that summarise global or local properties of the network (Bullmore & Sporns, 2009; Rubinov & Sporns, 2010).

However, there is no univocal way to define the brain network. There are several possible definitions for link weights and nodes outline. These choices determine the type of information (*e.g.* structural or functional) provided by graph metrics and they influence the final results (Griffa et al., 2013). Link weights could reflect structural properties of the connection (like, for example, diffusion tensor metrics) or could be values of functional connectivity between regions. On the other hand, the atlas used to define brain regions can be based, for example, on anatomical or functional subdivisions. Moreover, also the number and size of regions affect the result (Kaiser, 2011).

This approach can be of particular interest in the study of MS. The effect of a lesion is not circumscribed to a region, but it extends beyond that, affecting also the neural circuit(s) to which the lesioned region belongs. Therefore, regional analysis may not completely capture the damage, while global approaches like network analysis may overcome its limits.

Brain functions are thought to be supported by specific sub-networks and, hence, the structural pathological correlates of specific symptoms are expected to lie in the corresponding sub-network (here and, within this context, in the following sections, the term sub-network indicates a brain network made of few specific nodes as it can be found, for example, from resting state functional MRI (fMRI); it is opposed to the network representing the whole brain with nodes covering all of its surface). Within this framework, local changes induced by disease in tissue microstructure may be linked to network dynamics and to emerging dysfunction (Griffa et al., 2013; Cercignani & Gandini Wheeler-Kingshott, 2018).

As mentioned above, information processing speed has been linked to activity in the DMN. Functional studies originally conducted with positron emission tomography (PET) and later with resting state fMRI identified its constituents. Brain regions clas-

sically considered nodes of the DMN are precuneus/posterior cingulate cortex, medial frontal cortex, middle temporal gyri and angular gyri. The cerebellum is known to be connected to the cerebral cortex through the dentatorubrothalamocortical and the cerebellothalamocortical tracts (D'Angelo & Casali, 2013). These pathways structurally link the cerebellum also to brain regions associated to the DMN. Moreover, some studies showed that the DMN functional network comprises also cerebellar nodes (CBL-DMN) that were found in the posterior lobe of the cerebellum, in particular in correspondence of Crus I and Crus II (Habas et al., 2009; Krienen & Buckner, 2009; Stoodley & Schmahmann, 2010; Buckner et al., 2011).

Graph theory network metrics provide different results depending on the nodes included in the network. Therefore, when investigating associations between network quantities and symptoms all functionally relevant regions should be included.

It has been proved that the cerebellum contributes to cognitive functions (Ramnani, 2006; Strick et al., 2009; Tedesco et al., 2011; D'Angelo & Casali, 2013; Koziol et al., 2014; Sokolov et al., 2017) and that it is involved in neurological and psychiatric conditions (Jacobs et al., 2018; Wu & Hallett, 2013; Fatemi et al., 2012; Weier et al., 2015). In particular, Weier et al. (2015) showed that MS lesions in cerebellum and in cortico-cerebellar pathways can result in cognitive deficits. Consequently, it would be important to know whether and how the connectivity between the cerebellum and cerebral DMN regions affects cognitive outcomes in neuropsychological tests.

This chapter illustrates how we used graph theory to investigate the cerebellar contribution to information processing speed within the CBL-DMN and the role of cortico-cerebellar connectivity in cognitive processing deficit caused by MS. In particular, we analysed the structural global efficiency (GE) of the network with and without the cerebellum and its capability to predict clinical outcomes as measured by SDMT.

1.3 Methods

1.3.1 Subjects and clinical assessment

For this study 68 patients with relapse-onset MS were selected. 22 HC with no known neurological or psychiatric condition were also enrolled. The study was approved by the local institutional ethics committee (NRES Committee London – Queen Square) and all subjects provided written informed consent.

The clinical and neuropsychological assessment was conducted by a certified neurologist, who administered a battery of tests including the SDMT, the Hospital Anxiety and Depression Scale (anxiety: HADS-A; depression: HADS-D) (Zigmond & Snaith, 1983) and the national adult reading test (NART). Expanded Disability Status Scale (EDSS) were also assessed.

The MS group was also divided in cognitively impaired MS patients (CIMS) and cognitively preserved MS patients (CPMS) (20 and 46 patients respectively). This was achieved by using a SDMT score of 40 points as cut-off value: this value was shown to be the optimal threshold to detect cognitive deficit in a cohort of 359 MS patients by Van Schependom et al. (2014).

	HC	MS	p	CIMS	CPMS	p
Participants (M / F)	10 / 12	24 / 44		7 / 13	16 / 30	
Age (yrs)	36.5 ± 10.8	46.7 ± 11.0	**	50.3 ± 10.6	45.3 ± 11.0	
Disease duration (yrs)	n.a.	16.7 ± 10.4	n.a.	21.9 ± 12.6	14.6 ± 8.5	*
Median EDSS (range)	n.a.	$4.5(1-8.5)$	n.a.	$6.0(1-8.5)$	$2.0(1-7.5)$	**
SDMT	62.6 ± 10.8	47.1 ± 12.5	**	32.1 ± 5.9	53.6 ± 8.3	n.a.
HADS-A	5.4 ± 4.2	6.6 ± 4.0		6.9 ± 4.0	6.3 ± 3.8	
HADS-D	3.0 ± 4.0	5.9 ± 3.6	**	6.8 ± 3.3	5.4 ± 3.6	
NART-predict	108.9 ± 9.3	107.4 ± 10.8		103.2 ± 9.8	109.2 ± 10.8	*

Tab. 1.1: Demographic and clinical data and neuropsychological scores. Results are shown as mean $\pm$ standard deviation unless otherwise reported. Statistical significance expressed by p-values refers to the values reported in the two columns at the left (* $p < 0.05$, ** $p < 0.01$).

Demographic and clinical data of all study participants are reported in Tab. 1.1.

1.3.2 MRI acquisition

Both MS patients and HC underwent a brain 3T MRI scan session using a 3T Philips Achieva MRI scanner (Philips Healthcare, Best, The Netherlands) with dual transmit and a 32-channel receive head-coil.

The MRI acquisition protocol included a sagittal high-resolution 3D T1w fast field echo scan ($\mathrm{TE} = 3.1\,\mathrm{ms}$, $\mathrm{TR} = 6.9\,\mathrm{ms}$, $\mathrm{TI} = 824\,\mathrm{ms}$, $1.0\,\mathrm{mm}$ isotropic resolution, 256×256 acquisition matrix, 180 sagittal slices) and an axial anterior commissure - posterior commissure oriented dual echo proton density (PD) / T2w scan ($\mathrm{TE} = 19/85\mathrm{ms}$, $\mathrm{TR} = 3500\,\mathrm{ms}$, $1.0 \times 1.0 \times 3.0\mathrm{mm}^3$ resolution, $\mathrm{FOV} = 240 \times 240\mathrm{mm}^2$).

Diffusion weighted images were acquired with a cardiac-gated axial spin echo (SE) EPI high angular resolution diffusion imaging (HARDI) scan aligned with the anterior commissure - posterior commissure line ($\mathrm{TE} = 68\,\mathrm{ms}$, $\mathrm{TR} \sim 24\,\mathrm{s}$ depending con cardiac rate, $2.0\,\mathrm{mm}$ isotropic resolution, 3.1 SENSE factor, 96×112 acquisition matrix, 112×112 reconstruction matrix, 72 slices with no gap, 61 isotropically distributed directions with $b = 1200\,\mathrm{s/mm}^2$ and 7 volumes with $b = 0\,\mathrm{s/mm}^2$).

1.3.3 Data processing

Image processing For data pre-processing of diffusion weighted images we used FSL[1] (Jenkinson et al., 2012). Pre-processing of diffusion images from all subjects included:

- eddy-currents distortions correction and diffusion vector realignment;
- brain extraction;
- diffusion tensor fit;

[1] `https://fsl.fmrib.ox.ac.uk/fsl/fslwiki`

- registration to Montreal Neurological Institute (MNI) 152 $1\,\mathrm{mm}$ standard space.

Image registration was performed using NiftyReg tools[2] following a validated pipeline (Muhlert et al., 2013), which involved both rigid and non-linear transformations.

For HC the following operations were also performed using MRtrix[3] (Tournier et al., 2012):

- fibre orientation distribution estimate using constrained spherical deconvolution (CSD) (Tournier et al., 2007);
- whole brain probabilistic tractography (2.5×10^{-6} tracks) (Tournier et al., 2012);
- generation of high resolution track density image (TDI) (Calamante et al., 2010).

TDI images provide improved resolution and contrast with respect to diffusion images: they were generated to help precise positioning of automatic and manually drawn regions of interest (ROI) .

JIM[4] was used to estimate the WM lesion load (WM-LL) from PD/T2w images of MS patients. 3D T1w images were used for tissue segmentation using SPM[5] and for estimate of the brain parenchymal fraction (BPF) (Rudick et al., 1999) using LEAP (Chard et al., 2010).

ROI selection A map of the DMN from existing literature was considered (Smith et al., 2009). The map, which was provided in MNI 152 at $2\,\mathrm{mm}$ spatial resolution, was divided in eight distinct binary ROIs corresponding to the nodes of the network:

- left and right medial frontal cortex;
- left and right angular gyrus;
- left and right precuneus/posterior cingulate cortex;
- left and right middle temporal gyrus.

Since cerebellar nodes were not considered in the map of the DMN, binary masks for left and right cerebellar hemispheres were obtained from the SUIT atlas (Diedrichsen, 2006; Diedrichsen et al., 2009). Therefore, the extended CBL-DMN consisted of the ten nodes shown in Fig 1.1.

Tractography and network analysis Probabilistic tractography (MRtrix) was used to reconstruct the edges of the network. In order to achieve an anatomically plausible reconstruction of all tracts, the following constraints were considered:

[2] `http://cmictig.cs.ucl.ac.uk/wiki/index.php/NiftyReg`
[3] `http://www.mrtrix.org`
[4] Xinapse Systems, `http://www.xinapse.com`
[5] `http://www.fil.ion.ucl.ac.uk/spm`

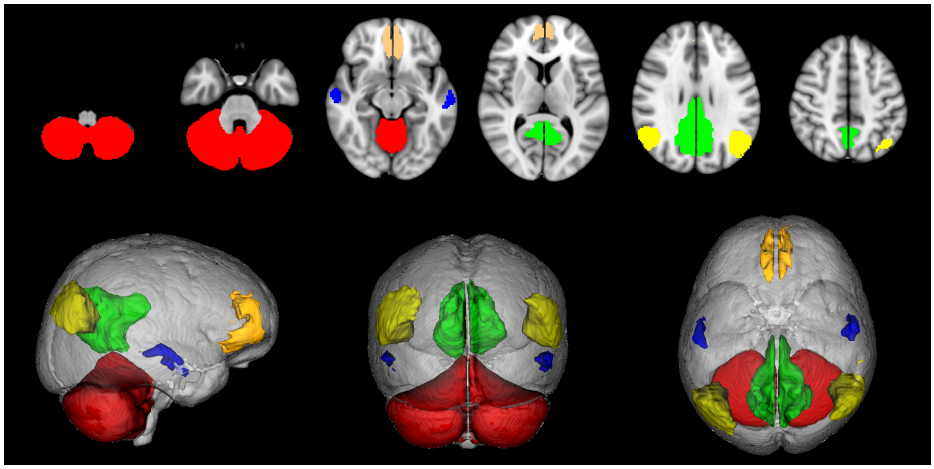

Fig. 1.1: Nodes of the extended CBL-DMN network. Medial frontal cortex (orange), angular gyri (yellow), precuneus/posterior cingulate cortex (green), middle temporal gyri (blue), cerebellum (red).

- fibres connecting pairs of homolateral brain cortex ROIs were reconstructed by seeding the smaller of the two; the cerebellum, the brainstem, the ventricles, the corpus callosum and the opposite cerebral hemisphere were considered as exclusion ROIs;
- fibres connecting pairs of contralateral brain cortex ROIs were reconstructed by seeding the corpus callosum; the cerebellum, the brainstem and the ventricles were considered as exclusion ROIs;
- fibres connecting contralateral middle temporal gyri were reconstructed by seeding the anterior commissure; the cerebellum, the brainstem and the ventricles were considered as exclusion ROIs;
- afferent fibres projecting from the cerebellum to the contralateral brain cortex areas were reconstructed by seeding the superior cerebellar peduncles and including the contralateral brain cortex ROIs (Palesi et al., 2015); with respect to the considered superior cerebellar peduncle the contralateral cerebellum, the homolateral red nucleus, the ventricles, the corpus callosum and the medulla oblongata were considered as exclusion ROIs;
- efferent fibres projecting from brain cortex areas to the contralateral cerebellum were reconstructed by seeding the cerebral peduncles and including the homolateral brain cortex ROIs and the contralateral middle cerebellar peduncles (Palesi et al., 2017); with respect to the considered cerebral peduncle the homolateral cerebellum, the ventricles, the corpus callosum and the medulla oblongata were considered as exclusion ROIs.

The resulting tracts obtained from HC were registered from each subject native space to the MNI 152 $1\,\mathrm{mm}$ standard space and binarised. The binary masks in the common

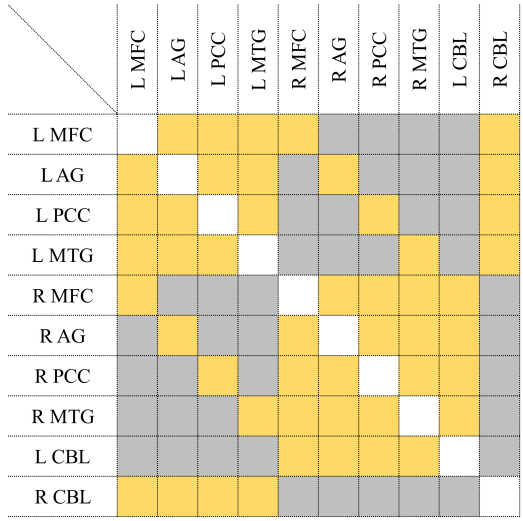

Fig. 1.2: Connectivity matrix of the CBL-DMN network. Tracts linking network nodes are shown in yellow, anatomically non existent connections between nodes are shown in grey and the elements along the principal diagonal that would represent self-connections are displayed in white. L/R = left/right. MFC = medial frontal cortex; AG = angular gyrus; PCC = precuneous/posterior cingulate cortex; MTG = middle temporal gyrus; CBL = cerebellum.

space were then averaged to create a population map of each tract. The final form of the tracts was obtained by selecting only voxels belonging to at least 50% of the subjects.

The thresholded masks were registered to fractional anisotropy (FA) maps of both MS patients and HCs and intersected with the white matter (WM) mask of the subject (Pagani et al., 2005; Rocca et al., 2007, 2010). Then, for each subject, we computed the 10×10 connectivity matrix, where each entry is mean FA of the tract linking the two corresponding nodes (see Fig. 1.2).

Connectivity matrices were analysed using the Brain Connectivity Toolbox (Rubinov & Sporns, 2010) as implemented in MATLAB[6]. The FA-weighted GE of the DMN and CBL-DMN networks was computed. Furthermore, the FA average value in the whole WM was computed for each subject (WM-FA) .

1.3.4 Statistical analysis

Statistical analysis of the data was performed using Statistical Package for Social Science (SPSS)[7]. First, outliers were identified by applying the standard Tukey's criterion (interquartile range multiplied by 1.5)(Tukey, 1977). Then, in order to assess significant difference in demographic data, clinical data, neuropsychological scores and MRI metrics between groups (MS *vs.* HC and CIMS *vs.* CPMS) T-tests were performed. Associations between metrics were examined by computing the Pearson correlation coefficients for the different groups. Resulting correlation coefficients were compared by applying

[6]The MathWorks, Inc., Natick, MA. `https://www.mathworks.com`
[7]IBM, Armonk, NY. `https://www.ibm.com`

	HC	MS	p	CIMS	CPMS	p
BPF	0.82 ± 0.02	0.80 ± 0.02	**	0.79 ± 0.02	0.80 ± 0.02	*
WM-LL (ml)	n.a.	8.08 ± 9.74	n.a.	11.85 ± 14.02	6.34 ± 6.72	
WM-FA	0.36 ± 0.04	0.24 ± 0.02	**	0.23 ± 0.03	0.24 ± 0.02	
GE(CBL-DMN)	0.33 ± 0.04	0.29 ± 0.03	**	0.28 ± 0.04	0.29 ± 0.02	
GE(DMN)	0.35 ± 0.04	0.29 ± 0.04	**	0.27 ± 0.04	0.30 ± 0.03	*

Tab. 1.2: MRI measures. Results are shown as mean $\pm$ standard deviation unless otherwise reported. Statistical significance expressed by p-values refers to the values reported in the two columns at the left (* $p < 0.05$, ** $p < 0.01$).

the Fisher z-transformation. Finally, MRI, demographic, clinical and neuropsychological variables were considered as predictors in a multiple regression analysis for CIMS and CPMS to evaluate their contribution to SDMT variation in a multivariable model.

1.4 Results

This work showed that the structural efficiency of the DMN is associated to SDMT performance in MS patients. In particular, GE(CBL-DMN) is the only significant predictor of cognitive processing impairment in multivariate model, while BPF and EDSS significantly contribute to SDMT in CPMS patients.

Here are reported all results starting from between-group comparison of metrics, to tractography results, to correlations between SDMT scores and MRI and clinical measures, to finish with results obtained from linear regression analysis.

Subjects demographics and group comparison of metrics Tab. 1.1 reports a summary of demographic and clinical data for the different groups of subjects. For one HC and two MS subjects not all tests could be administered.

The Tukey's criterion identified one HC outlier, which was removed from the subsequent data analysis that produced the results reported here. However, analysis was also performed including this subject, but results and conclusions did not significantly change.

In Tab. 1.1 and Fig. 1.3 significant differences in clinical scores between groups are highlighted (* for $p < 0.05$ and ** for $p < 0.01$). The main differences between HCs and MS patients were SDMT and hospital anxiety and depression scale - depression (HADS-D) scores, while CIMS and CPMS significantly differed in EDSS scores.

Tab. 1.2 and Fig. 1.4 report the group averaged MRI metrics. All these measures resulted to be significantly different between HCs and MS patients. On the other hand, the only measures that could significantly distinguish CIMS from CPMS subjects were BPF and GE(DMN).

Tractography All expected cortico-cerebellar and cortico-cortical connections were reconstructed with success, resulting in 32 tracts (see Fig. 1.5). However, some of the tracts

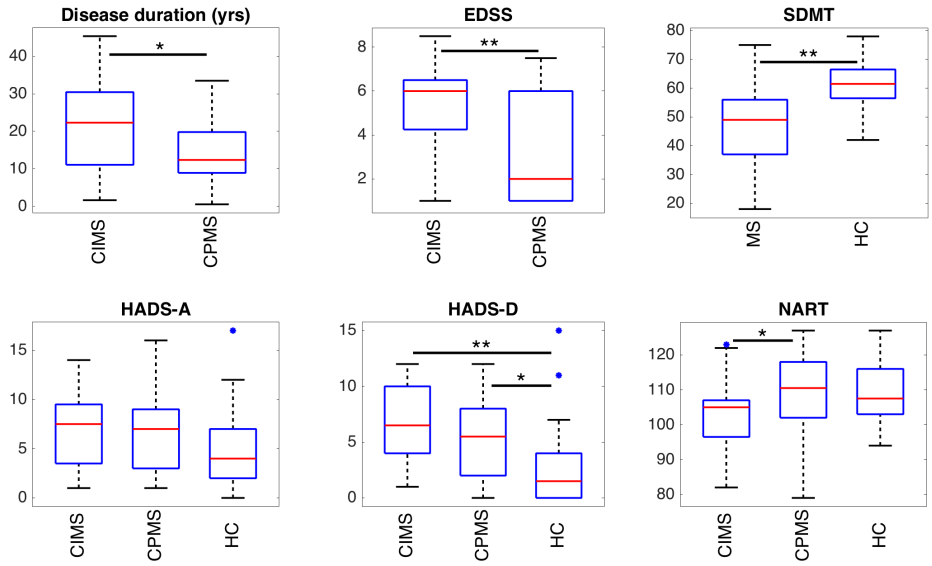

Fig. 1.3: Boxplots representing the summary of clinical scores in the different groups of subjects. Statistically significant differences between groups are indicated with * for $p < 0.05$ and with ** for $p < 0.01$. It can be observed that SDMT and depression (HADS-D) are significantly different in MS patients with respect to HCs. EDSS and, to a lesser extent, disease duration and NART can discriminate between CIMS and CPMS patients.

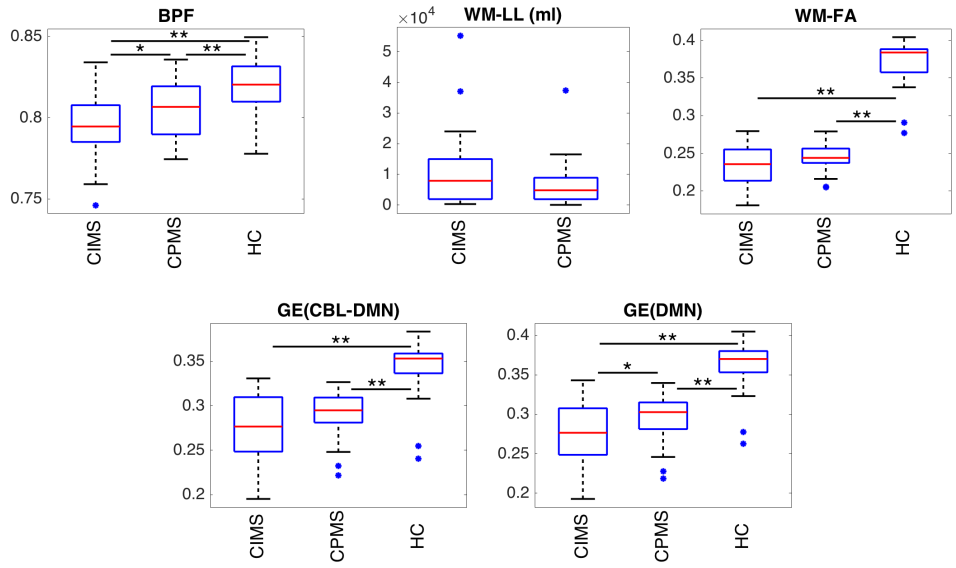

Fig. 1.4: Boxplots representing the summary of MRI metrics in the different groups of subjects. Statistically significant differences between groups are indicated with * for $p < 0.05$ and with ** for $p < 0.01$. It can be observed that all these measures can distinguish between MS patients and HCs. BPF and GE(DMN) are significantly reduced in CIMS with respect to CPMS. Despite the absence of statistical significance (which could also reflect differences in group sizes), a similar trend can be observed also for GE(CBL-DMN) and WM-FA.

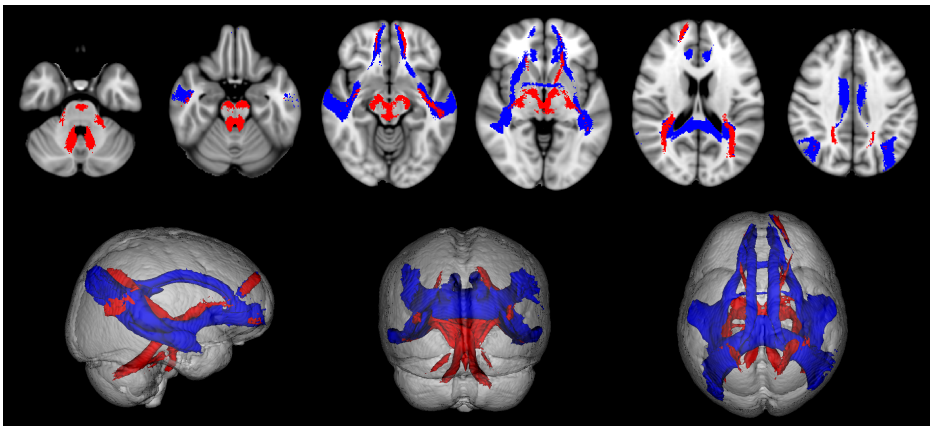

Fig. 1.5: Tractography results from HCs were registered to MNI 152 standard space at $1\,\mathrm{mm}$ resolution to create a population map for each tract. Here are shown the tracts resulting from the application of a 50% probabilistic threshold to these population maps. The tracts shown here were subsequently registered to MS patients to compute tract-averaged diffusion metrics. Tracts connecting cerebral nodes are displayed in blue, while cortico-cerebellar connections are displayed in red.

connecting the cerebellum to the cerebral cortex resulted to be poorly traced: in fact, many streamlines were lost at the level of peduncles decussation, where fibre geometry is most intricate and the tractography algorithm most frequently fails. This is the case of tracts originating from the medial frontal cortex and projecting to the cerebellum and of tracts originating from the cerebellum projecting to the posterior cingulate cortex and to the angular gyri.

Associations with SDMT For HCs no significant correlation was found between MRI, clinical, neuropsychological or demographic variables and SDMT scores (see Tab. 1.3). Strong and significant correlations ($\rho \approx 0.5$ and $\mathrm{p} < 0.001$) were found for MS patients instead, in particular between SDMT scores and FA-weighted metrics, EDSS and BPF. In the same group of subjects, significant correlations were found also between SDMT performance and age, disease duration and WM-LL, even though with lower coefficients ($\rho \approx 0.3$).

When considering CIMS patients only, GE(CBL-DMN) and GE(DMN) showed the strongest correlations with SDMT scores ($\rho > 0.8$ and $\mathrm{p} < 0.001$). Significant strong correlations were also found for WM-FA and BPF, while there was no correlation between SDMT and EDSS. When considering CPMS patients, SDMT performance was most associated with BPF ($\rho = 0.57$ and $\mathrm{p} < 0.001$) and significant correlations were found also for GE(CBL-DMN), GE(DMN) and EDSS. The difference between correlation coefficients for CPMS and CIMS is statistically significant only for FA-weighted measures ($\mathrm{p} < 0.01$ for GE(CBL-DMN and $\mathrm{p} < 0.05$ for GE(DMN and WM-FA).

As illustrated in Tab. 1.4, the GE(DMN) alone could explain 67% of SDMT variance, while this increased to 76% with the inclusion of cerebellar nodes. In CPMS the amount

	HC		MS		CIMS		CPMS	
GE(CBL-DMN)	0.13 (0.597)	0.02	**0.54 (<0.001)**	**0.29**	**0.87 (<0.001)**	**0.76**	**0.51 (<0.001)**	**0.26**
GE(DMN)	0.15 (0.524)	0.02	**0.57 (<0.001)**	**0.33**	**0.82 (<0.001)**	**0.67**	**0.48 (0.001)**	**0.23**
WM-FA	0.16 (0.508)	0.02	**0.47 (<0.001)**	**0.22**	**0.73 (<0.001)**	**0.53**	0.37 (0.012)	0.13
Age	-0.09 (0.692)	0.01	**-0.32 (0.009)**	**0.10**	-0.17 (0.469)	0.03	-0.28 (0.056)	0.08
EDSS	n.a.	n.a.	**-0.52 (<0.001)**	**0.27**	-0.04 (0.861)	<0.01	**-0.46 (0.001)**	**0.21**
Disease duration	n.a.	n.a.	**-0.35 (0.004)**	**0.12**	-0.27 (0.246)	0.07	-0.12 (0.416)	0.02
WM-LL	n.a.	n.a.	**-0.39 (0.002)**	**0.15**	-0.45 (0.055)	0.20	-0.31 (0.050)	0.09
BPF	-0.13 (0.599)	0.02	**0.55 (<0.001)**	**0.31**	**0.63 (0.004)**	**0.39**	**0.57 (<0.001)**	**0.33**
NART-predict	0.04 (0.873)	<0.01	0.32 (0.010)	0.10	0.21 (0.376)	0.04	0.18 (0.221)	0.03
HADS-A	0.23 (0.330)	0.05	-0.09 (0.476)	0.01	-0.17 (0.469)	0.03	-0.03 (0.872)	<0.01
HADS-D	0.09 (0.695)	0.01	-0.30 (0.016)	0.09	-0.29 (0.220)	0.08	-0.24 (0.109)	0.05

Tab. 1.3: Correlations of MRI measures and clinical data with SDMT. Person correlation coefficients are reported (first column of each group) along with p-values (in brackets) and the corresponding R^2 (each second column). Correlations with p-value < 0.01 are highlighted in bold.

of explained variance was 23% and 26% for GE(DMN) and GE(CBL-DMN) respectively. In both groups GE(CBL-DMN) showed the highest correlation with SDMT scores (see Fig. 1.6) and thus it was considered for the following regression analysis, where demographic, clinical, neuropsychological variables and other MRI metrics were took into account (see Tab. 1.5).

Linear regression analysis using multivariable models showed that GE(CBL-DMN) remained the only significant predictor of SDMT variability in CIMS group. On the other hand, for CPMS patients EDSS and BPF add a significant contribution to the explained SDMT variance as expressed by R^2: this increased from 0.26 (GE(CBL-DMN) alone) to 0.34 and 0.37 respectively and with BPF in particular showing even lower p-value than GE(CBL-DMN).

1.5 Discussion

In this study we demonstrated the role of the cerebellum in the context of supporting information processing in MS by studying the integrity of the CBL-DMN and its rela-

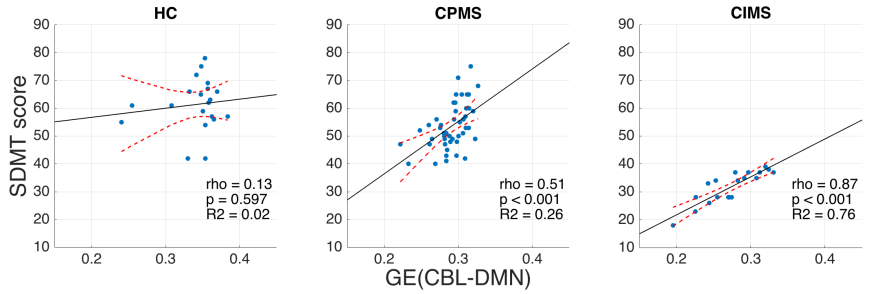

(a)

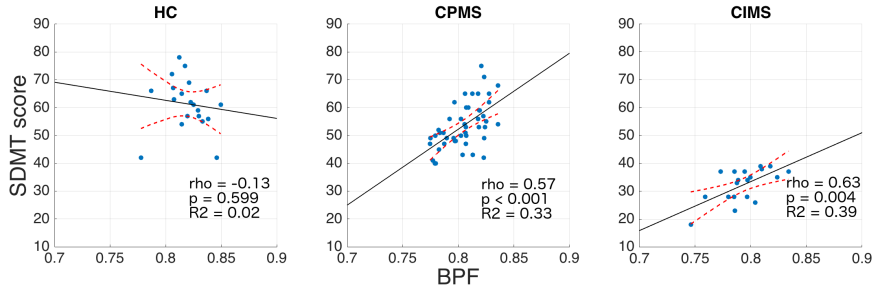

(b)

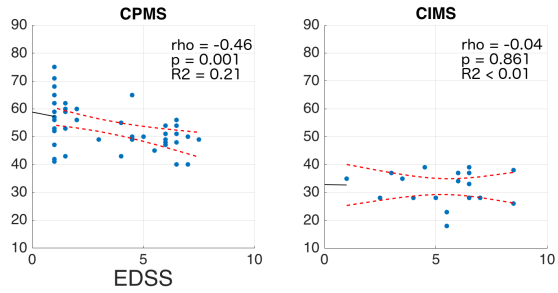

(c)

Fig. 1.6: Scatter plots representing SDMT vs GE(CBL-DMN) (a), BPF (b) and EDSS (c) for HCs (left), CPMS (centre) and CIMS (right). Solid black lines represent the linear regression model fit, while dashed red lines represent 95% confidence intervals. It is noteworthy that GE(CBL-DMN) predicts SDMT performance progressively better going from HCs (no significant correlation) to CPMS ($\rho = 0.51$, $p < 0.001$) to CIMS ($\rho = 0.87$, $p < 0.001$). The difference between correlation coefficients for CPMS and CIMS is statistically significant ($p < 0.01$) only for GE(CBL-DMN), as verified by applying Fisher z-transformation.

	SDMT predictor	R	R^2	R^2 corrected	p-value
CIMS	GE(DMN)	0.82	0.67	0.65	0.001
	GE(CBL-DMN)	0.87	0.76	0.75	<0.001
CPMS	GE(DMN)	0.48	0.23	0.21	<0.001
	GE(CBL-DMN)	0.51	0.26	0.25	<0.001

Tab. 1.4: Linear regression analysis in CIMS and CPMS patients. SDMT is considered as the dependent variable and GE(CBL-DMN) and GE(DMN) are considered individually as predictors. In both groups, GE(CBL-DMN) is the best predictor of SDMT variability.

tionship with cognitive performance as clinically assessed by SDMT.

We found that the network structural integrity is compromised by pathology and that its GE shows significant correlation with SDMT performance. In particular, we found that in those subjects showing more severe cognitive deficit (CIMS) the network GE is the best predictor of cognitive performance, when compared to other MRI or clinical measures. Furthermore, the inclusion of cerebellar nodes led to even stronger association. On the contrary, measures of atrophy (BPF) and general disability (EDSS) provide the greatest correlation with SDMT scores in CPMS. The increased association found between GE and SDMT in CIMS with respect to CPMS seems consistent with the hypothesis of a network collapse proposed by Schoonheim et al. (2015).

Hindered neuronal communication is a main consequence of MS pathology and it was proposed as the mechanisms at the basis of cognitive impairment (Dineen et al., 2009; Bozzali et al., 2013). In particular, regional analysis conducted in previous studies showed that structural damage affecting individual bundles of WM fibres pertaining to the DMN reflects on cognitive performance (Rocca et al., 2010; Zhou et al., 2014; Hawellek et al., 2011; Roosendaal et al., 2009, 2010). However, the modest correlations found indicate that the subject-specific heterogeneity of MS-induced damage prevents an exhaustive explanation of deficit, at least until this is based on structural changes of individual bundles of WM fibres.

Thus, it became clear that local approaches may not be adequate to describe the impairment of a specific cognitive domain. Moreover, given the nature of the MS damage and the interactive behaviour of brain networks, different subjects could have different portions of the DMN connectivity affected, resulting however in a similar global derangement.

Graph theory methods can summarise the effect local damage affecting different parts of the network in few comprehensive metrics, thus assessing its level of integrity. Graph theory has already been applied to study changes in brain networks topology in MS and this was done at different network scales (Llufriu et al., 2017; Shu et al., 2016, 2011; He et al., 2009; Pardini et al., 2015). It was found that graph metrics are able to capture network abnormalities and that they can better predict disability with respect to measures of local properties (Pardini et al., 2015, 2014).

As mentioned above, brain functions are thought to be encoded in specific subnetworks. Thus, it is reasonable to look for structural correlates of specific deficits in the corresponding sub-network (Griffa et al., 2013; Menon, 2011). Cognitive processing

	Model predictors	R	R^2	R^2 corrected	Sig. GE(CBL-DMN)	Sig. other variable
CIMS	GE(CBL-DMN), Age	0.87	0.76	0.74	<**0.001**	0.793
	GE(CBL-DMN), EDSS	0.87	0.76	0.74	<**0.001**	0.851
	GE(CBL-DMN), Disease duration	0.87	0.76	0.74	<**0.001**	0.931
	GE(CBL-DMN), WM-LL	0.88	0.77	0.74	<**0.001**	0.630
	GE(CBL-DMN), WM-FA	0.88	0.78	0.75	<**0.001**	0.326
	GE(CBL-DMN), BPF	0.88	0.78	0.75	<**0.001**	0.634
	GE(CBL-DMN), NART-predict	0.87	0.76	0.74	<**0.001**	0.804
	GE(CBL-DMN), HADS-A	0.87	0.76	0.74	<**0.001**	0.847
	GE(CBL-DMN), HADS-D	0.88	0.78	0.75	<**0.001**	0.296
CPMS	GE(CBL-DMN), Age	0.57	0.32	0.29	<**0.001**	0.063
	GE(CBL-DMN), EDSS	0.59	0.34	0.31	**0.004**	**0.025**
	GE(CBL-DMN), Disease duration	0.51	0.26	0.23	<**0.001**	0.867
	GE(CBL-DMN), WM-LL	0.52	0.27	0.23	**0.004**	0.944
	GE(CBL-DMN), WM-FA	0.51	0.26	0.23	**0.009**	0.990
	GE(CBL-DMN), BPF	0.61	0.37	0.35	0.087	**0.008**
	GE(CBL-DMN), NART-predict	0.53	0.28	0.25	<**0.001**	0.319
	GE(CBL-DMN), HADS-A	0.51	0.26	0.23	<**0.001**	0.813
	GE(CBL-DMN), HADS-D	0.54	0.29	0.26	<**0.001**	0.192

Tab. 1.5: Linear regression analysis in CIMS and CPMS patients. SDMT is considered as the dependent variable and GE(CBL-DMN) is tested against each other MRI or clinical variable. The second last column reports the p-value associated with GE(CBL-DMN) within each model and the last column reports the p-value associated with each second predictor. GE(CBL-DMN) holds as the only significant predictor against each other variable in CIMS, while in CPMS EDSS and BPF are also significant predictors of SDMT performance. p-values < 0.05 are displayed in bold.

has been associated with the DMN (Forn et al., 2013; Rocca et al., 2010; Sumowski et al., 2010; Bonavita et al., 2015) and hence, we decided to focus on this specific network. Conversely, a graph representation of the whole-brain network could be more appropriate to describe macroscopic disease patterns, but it may be not sufficiently specific to link structural changes to clinical performance (Cercignani & Gandini Wheeler-Kingshott, 2018).

GE was chosen as the primary measure of network integrity: it captures the overall network damage and quantifies the efficiency of communication between network regions. Mean FA was chosen as link weight by virtue of its recognised sensitivity to MS-induced damage in both focal lesions and normal-appearing white matter (NAWM) (Kutzelnigg et al., 2005; Werring et al., 1999), which has been linked to disability in MS (Dineen et al., 2009; Hulst et al., 2013; Deppe et al., 2015). With regards to network behaviour, it is important to take NAWM into account because the widespread damage affecting it is independent of lesion location and because it could impact network functions as much as focal lesions (Cercignani & Gandini Wheeler-Kingshott, 2018).

Our results suggest that FA-weighted GE captures indeed MS-related damage affecting the DMN circuit and that it significantly correlates with cognition. no significant correlation with SDMT performance was found in our HC population; on the other hand, we found that GE significantly contributes to SDMT performance in MS. In agreement with previous studies, we found that SDMT scores are significantly associated also with WM-FA, BPF and EDSS in MS patients (Louapre et al., 2014; Deppe et al., 2015). Our results suggest that cognitive performance in MS patients is influenced to a similar degree by alteration of tissue microstructure, atrophy and disease course. It remains to be discussed whether the DMN connectivity to the cerebellum can further strengthen the results.

Valentino et al. (2009) and Bonnet et al. (2010) hypothesised that poor cognitive performance could originate also from the alteration of the cortico-cerebellar pathways that support automation and attention processes. Subsequently, it has been proved that MS-related cognitive impairment is influenced also by cerebellar pathology (Weier et al., 2014, 2015). Finally, with regards to our case of interest, recent studies expressly reported the existence of a link between cognitive processing deficit and the posterior cerebellar lobules and the cerebellar peduncles (Moroso et al., 2017a,b). Therefore, in the light of the importance of network specificity illustrated above and given the recognised contribution of cerebellar pathology to cognitive processing deficit, we decided to assess the effect of including cerebellar nodes within the DMN.

GE(CBL-DMN) provided greater correlation with SDMT with respect to DMN alone for both CIMS and CPMS patients: the inclusion of cortico-cerebellar connections increased the explained SDMT variance R^2 from 67% (GE(DMN)) to 76% for CIMS patients and from 23% to 26% for CPMS. This suggests that the DMN network connectivity with the cerebellum, rather than cerebellar pathology per se, can be functionally relevant to SDMT performance in MS and this highlights the necessity to address networks as a whole rather than focusing on separate components.

In addition to the strength of the association of GE(DMN) with SDMT, multivariable regression analysis highlighted another important difference between CIMS and CPMS.

While for the first group the network GE holds as the only significant predictor of SDMT variability, in the second group, BPF and EDSS are also important factors. This suggest that the DMN integrity can have a different influence on cognitive performance at different stages of the disease. In milder stages of MS (e.g. in CPMS), the damage accumulated since the disease onset might affect the network only slightly, thus preserving the overall functioning of the network. With a heavier disease burden (e.g. in CIMS), as captured by a worse score in the SDMT, it is possible that the accumulating damage reaches a critical threshold, beyond which the network functioning collapses and the cognitive performance worsens more rapidly (Schoonheim et al., 2015; Shu et al., 2016; Cercignani & Gandini Wheeler-Kingshott, 2018)). Here, the absence of a statistically significant difference in GE(DMN) between CIMS and CPMS groups could also reflect differences in group sizes (see Fig. 1.4).

Although EDSS significantly distinguishes between CIMS and CPMS groups, no correlation was found between SDMT and EDSS scores in CIMS. FA-weighted measures are key factors of poor SDMT performance in CIMS patients, with unmatched correlation coefficients ranging from 0.73 to 0.87 ($p < 0.001$). The network efficiency alone provided $R^2 = 0.76$ and linear regression analysis showed that GE(CBL-DMN) is the best predictor of poor cognitive performance, while no other variable adds a relevant contribution to the percentage of the explained SDMT variance. However, in CPMS patients, factors associated with the general disease course like BPF and EDSS still importantly affect SDMT performance. The inclusion of BPF and EDSS as explanatory variables in a linear regression model improves the percentage of SDMT explained variance in CPMS (R^2 growing respectively from 0.26 to 0.37 and 0.34), thus showing that SDMT performance in CPMS patients is driven by both a "milder" alteration of the network efficiency and the general disease course. Therefore, we report a possible distinct role of the CBL-DMN network in SDMT performance at different cognitive stages. In particular, our results show that the association between GE(CBL-DMN) and SDMT performance is progressively strengthened with increasing network derangement. In HC the CBL-DMN structural integrity is untouched and the SDMT performance is completely unrelated to GE.

In CPMS, the SDMT scores are only partially dependent on GE(CBL-DMN) as other factors associated with the general disease course such as BPF contribute to performance. Interestingly, in CIMS the association between GE(CBL-DMN) and SDMT scores becomes much stronger (see Fig. 1.6) implying that GE(CBL-DMN) assumes a more prominent role in cognitive performance.

1.5.1 Limitations

This work is not without limitations. Here, we report an important association between GE(CBL-DMN) and SDMT performance in MS, but this is a cross-sectional study, so causality between network microstructural damage and SDMT worsening can only be hypothesised and a longitudinal study is warranted in the future. Graph theory provides many different measures and several different link weights can be used, but it is not clear yet which combination could be the best to capture clinically relevant network abnormalities in MS. Moreover, Powell et al. (2018) showed that many factors can affect

group results of graph measures and, in particular, that inferences of network disruptions in disease are substantially affected by the choice of weights. Here, we focused on FA-weighted GE to capture the overall network damage and did not assess other graph theory measures whose interpretation is less straightforward (Griffa et al., 2013), for example segregation measures. Further work is required to clarify which graph theory measures are most useful. With regards to link weights, the diffusion tensor model that we used has been shown to be sensitive but not-specific to the different pathological substrates of MS (Cercignani & Gandini Wheeler-Kingshott, 2018). Alternative frameworks, like models illustrated in Chap. 2, could provide metrics more specific to pathology-related microstructural damage: these metrics combined with graph theory could give a better insight into the mechanisms leading from pathology alterations at the cellular level to subsequent functional impairment. In the present study we only used one measure (FA) to weight DMN connection, but multimodal approaches using different imaging modalities, for example combining different structural measures (Pardini et al., 2015) or structural and functional imaging (Zhou et al., 2014; Romascano et al., 2015) have been proposed and may further improve our ability to explain cognitive outcomes. This could be scoped in future work and composite weights could be adopted.

1.6 Conclusions

Our data showed that GE(CBL-DMN) is reduced by MS pathology and it is increasingly associated with information processing speed as cognitive impairment becomes evident. Concurrently, with increasing cognitive impairment, GE(CBL-DMN) dominates over more global measures of brain pathology (WM-FA and BPF) or disability (EDSS). We showed that connections between the cerebellum and the DMN are relevant to SDMT performance: cortico-cerebellar connections within the DMN play an important role in the network organisation and their MS-related structural alteration affects cognitively-relevant network functioning. These results warrant future longitudinal studies to assess the clinical translation potential of network measures for the early detection of cognitive processing speed decline.

CHAPTER 2

Cerebellar microstructure

In the previous chapter we have shown that cerebro-cerebellar connectivity plays an important role in cognitive processing in MS. However, the cerebellum is involved in several structural and functional loops.

How the cerebellum supports brain networks executing so many different tasks is still matter of debate. Given its rather uniform cyto-architecture, Schmahmann (2010) proposed that the cerebellum contributes to brain functions by means of a "universal cerebellar transform"(UCT), an hypothesised mathematical function that processes and integrates signals independently of their nature (*e.g.* sensorimotor or cognitive). According to this theory the UCT is constant throughout the whole extent of the cerebellum and functional diversity is only due to the connectivity patterns of each area of the cerebellar cortex. However, studies of cerebellar anatomy, development and neurodegeneration, expression of molecular markers and physiology reported the existence of microstructural inhomogeneities in the cerebellar cortex (Cerminara et al., 2015). Interestingly, it has also been shown that cellular morphological features can affect the electro-physiological properties of the cell (Canto et al., 2016).

Therefore, in order to fully understand how the cerebellum contributes to brain functions, its microstructural features must be studied. It is intriguing to think that cerebellar structure and function might be closely linked and that regions subserving different functions might do this in virtue of some kind of structural peculiarity. This would have incredibly important implications for modelling of brain networks and emerging behaviour, a research field where, thanks to its unmatched versatility and non-invasiveness, MRI plays a unique role.

Therefore, this chapter aims to assessing whether the sensitivity of a high quality 3 T MRI protocol is sufficient to detect significant differences in cyto-architecture between subregions of the cerebellar cortex, these being possibly related to the findings reported in histological studies.

dMRI is able to probe tissue microstructure non-invasively. This can be done with statistical descriptions of the diffusion signal at the voxel level, as it is done with diffusion tensor imaging (DTI) and diffusional kurtosis imaging (DKI), or with biophysical models that describe tissue as a set of water pools (*i.e.* compartments with different geometrical properties determined by tissue architecture where water molecules diffuse).

In the previous chapter we used DTI to produce measures sensitive (even though not specific) to tissue alterations caused by MS. This choice was dictated by the diffusion ac-

quisition protocol that, with only one b-value, allowed the estimation of diffusion tensor measures only. However, DTI have several well-known limitations (Jones et al., 2013), that become evident in regions with complex fibre geometry.

More advanced diffusion models have been proposed. Biophysical models attempt to model water pools in order to provide measures specific to cellular properties, like axonal density or axonal diameter. However, they are usually based on strong assumptions that limit their applicability. On the contrary, statistical descriptions like DTI and DKI rely on less assumptions and are more versatile, even though the interpretation of the resulting measures in terms of cellular properties can be trickier. In particular, DKI is a higher-order extension of DTI. With respect to DTI, it requires the acquisition of more than one b-value to quantify the departure of diffusion from a gaussian behaviour. In this chapter, T1w, T2w and diffusion measures like DTI and DKI obtained from a high quality $3\,\mathrm{T}$ MRI Human Connectome Project (HCP) dataset (with diffusion sequences providing for three b-values) are exploited to describe the microstructure of the cerebellar cortex.

2.1 Introduction

It has been estimated that the contribution of the cerebellum to the total mass of the brain is 10%, but that it contains more than 80% of brain neurons as granule cells (Herculano-Houzel, 2009). Therefore, the cellular density in the cerebellum is much higher than in the brain and cellular arrangement is highly ordered. Because of this, the cerebellum exhibits outstanding processing capabilities and it is involved in a great number of neuronal circuits. Historically, it is thought to play a role only in sensorimotor functions, but experimental evidence proved its involvement also in higher cognitive functions (D'Angelo & Casali, 2013; O'Reilly et al., 2010; Ramnani, 2006; Sokolov et al., 2017; Stoodley & Schmahmann, 2010; Strick et al., 2009).

For this reason interest started to grow around the cerebellum also in the MRI community. Dedicated anatomical and functional MRI atlases of the cerebellum have been produced and made freely available (Diedrichsen et al., 2009, 2011a; Buckner et al., 2011; van Baarsen et al., 2016). Functional MRI was used to investigate cerebellar functions and functional connectivity (Habas et al., 2009; Krienen & Buckner, 2009; O'Reilly et al., 2010; Stoodley & Schmahmann, 2010; Buckner et al., 2011). Structural imaging was used to investigate cerebellar anatomy and microstructure (Marques et al., 2010; Diedrichsen et al., 2011a; Boillat et al., 2018). Diffusion MRI was used to reconstruct cerebellar anatomy and structural connectivity (Ramnani et al., 2006; Granziera et al., 2009; Dell'Acqua et al., 2013; Palesi et al., 2015; Steele et al., 2016; van Baarsen et al., 2016; Palesi et al., 2017). Moreover, MRI constitutes a powerful tool to evaluate the role of the cerebellum in neurological conditions like autism, attention deficit hyperactivity disorder, dyslexia, multiple sclerosis (see Chap. 1), Alzheimer's disease, depression and essential tremor (D'Mello & Stoodley, 2015; Fatemi et al., 2012; Stoodley, 2014; Weier et al., 2015; Jacobs et al., 2018; Zhao et al., 2016; Novellino et al., 2016).

Thanks to its capability to reconstruct major bundles of WM fibres, diffusion MRI has been exploited to reconstruct the numerous segments composing the cerebellar cir-

cuits and connecting the cerebellar cortex, the deep cerebellar nuclei (DCN), the olivary nuclei, the pons, the thalamus and the cerebral cortex (Ramnani et al., 2006; Granziera et al., 2009; Palesi et al., 2015; Steele et al., 2016; van Baarsen et al., 2016; Palesi et al., 2017). Interestingly, Dell'Acqua et al. (2013) performed ultra-high resolution ($100\,\mu m$) diffusion imaging and tractography on a fixated cerebellum to reconstruct fibres in the different cerebellar cortical layers of individual folia; Steele et al. (2016) used ultra-high field (UHF) in-vivo sub-millimetre diffusion imaging to track fibres projecting from the cerebellar cortex to the dentate nuclei; van Baarsen et al. (2016) used probabilistic streamline tractography to produce a probabilistic atlas of the cerebellar peduncles.

However, to date MRI diffusion modelling has not been exploited to investigate the microstructural features of the cerebellum. All cerebellar circuits present the same cytoarchitecture (*i.e.* the cellular components of the circuit and their morphological features are the same) and this led to the assumption of a uniform cerebellar cortex. Consequently, it is thought that functional diversity of cerebellar regions is only due to the distinct signal sources and targets involved in each individual circuit. However, these concepts have been (and are still) challenged by an increasing number of studies that highlighted local differences across regions of the cerebellar cortex and, consequently, it has been hypothesised that differences in information processing may arise also from regional differences in cerebellar circuitry (Cerminara et al., 2015).

The study of most cellular populations (*i.e.* Purkinje, granule, Golgi cells, etc.) of the cerebellum showed that cells can differ in physiological, molecular and morphological properties across regions. In particular, evidences of inhomogeneities came from studies of cerebellar anatomy, development and neurodegeneration, expression of molecular markers and physiology. Cerminara et al. (2015) provided an exhaustive review of such differences. Here, we briefly report some of the main findings that are of interest for the current work. Looking at cerebellar architecture it was found that:

- the packing density of **Purkinje cells** is higher in the anterior lobe with respect to the posterior lobe; it is higher at the folium apex with respect to the base and the morphology of the dendritic tree is also different at the base and at the apex of the folium; the diameter of Purkinje cells body is larger in the vermis with respect to the hemispheres and the axon diameter is different in different WM compartments;

- the **granule cells** packing density is higher in the folium apex than at the base; the diameter of granule cells body is larger in the vermis with respect to the hemispheres; **parallel fibers** in the deep regions of the molecular layer are thicker and shorter than those lying closer to the external surface of the cerebellar cortex;

- **unipolar brush cells** are more numerous in the nodulus (which corresponds to the vermal lobules Xa and Xb), in the ventral uvula (which corresponds to the vermal lobules IXd), in the flocculus and in the ventromedial paraflocculus with respect to other regions of the cerebellar cortex;

- the cellular density of **Lugaro cells** is higher in the posterior lobe with respect to the anterior lobe, except for lobules VIa-VIb and X;

- the packing density of **Golgi cells** is higher in the vermis than in the corresponding lobules of the hemispheres and it is maximum in the flocculus and in lobule IX; the size of Golgi cells soma is larger in the vermis with respect to the hemispheres.

From a molecular and physiological point of view, most studies focused on the properties of Purkinje cells, because they constitute the only output of the cerebellar cortex. Looking at the expression of molecular markers it was found that the cerebellar cortex can be divided in rostro-caudally oriented stripes. The most extensively (but not only) studied molecular pattern is the one produced by Aldolase C enzyme (usually referred to as Zebrin II) that can be expressed by Purkinje cells. The cerebellar cortex exhibits an alternating pattern of stripes of groups of Purkinje cells that do and do not express Zebrin II. This pattern is highly conserved across many different animal species including mammals and birds. From a physiological point of view, regional variations of intrinsic Purkinje cell properties were found across cerebellar cortical regions. The same is true for synaptic physiology of Purkinje cells. Most of these findings came from animal studies, mainly rodents and small mammals, but in those cases where the studies were repeated for primates and humans the results were confirmed.

It is known that fissures between lobules do not coincide with the borders of functional areas and other mappings of the cerebellar cortex are possible depending on the criteria adopted for its subdivision (Apps & Hawkes, 2009). Therefore, in the light of the above-mentioned hypothesis of inhomogeneity-driven functional diversity, these differences in cellular populations could be relevant for understanding the functional organization of the cerebellum. In particular, here we focus on cyto-architecture: cell morphology can have an influence on its electro-physiological and functional properties. This was shown for example in the cerebellar nuclei, where heterogeneity in cell size and density is known to exist across regions (Braak & Braak, 1983; Yamaguchi & Goto, 1997; Voogd, 2003; Ristanović et al., 2010; Tellmann et al., 2015a): Canto et al. (2016) showed in neurons of the cerebellar nuclei that soma size affects electro-physiological properties of the cell like membrane resistance, capacitance and spike length.

At the same time, cellular density and morphology determine the geometrical properties of the environment where water molecules diffuse. In principle, this has an effect on diffusion MRI signal. However, this differences could be too small to be detected by current techniques and thus it must be assessed whether diffusion MRI is sufficiently sensitive to such inhomogeneities.

To date diffusion imaging in the cerebellum has never focused on its microstructure. Therefore, the aim of this work is to investigate cerebellar cyto-architecture by applying different models of the diffusion signal to detect those inhomogeneities brought to light by histological studies.

2.2 Methods

2.2.1 MRI data

For this work we used high quality data provided by the HCP (Essen et al., 2013). In particular we considered diffusion and structural data from the 100 Subjects Data Re-

	Diffusion	T1w	T2w
Sequence	2D SE-EPI	3D MPRAGE	3D T2-SPACE
TR (ms)	5520	2400	3200
TE (ms)	89.5	2.14	565
TI (ms)	-	1000	-
Flip angle (deg)	78	8	variable
Refocusing flip angle (deg)	160	-	-
PE direction	R→L / L→R		
FOV (mm) (RO×PE)	210×180	224×224	224×224
Voxel size (mm)	1.25 isotropic	0.7 isotropic	0.7 isotropic
Echo spacing (ms)	0.78	-	-
BW (Hz/px)	1488	210	744
Multiband factor	3	-	-
iPAT	-	2	2
PPF	6/8	-	-
Diffusion scheme	monopolar	-	-
b-values (s/mm^2)	1000, 2000, 3000	-	-
Diffusion directions per shell	90	-	-
b=0 s/mm^2 volumes	6	-	-

Tab. 2.1: Acquisition details provided for diffusion and structural protocols from HCP.

lease with minimal pre-processing pipeline. This includes diffusion and T1w and T2w structural imaging. Acquisition protocol details are shown in Tab. 2.1. A monopolar sensitizing gradient scheme was adopted for diffusion encoding; the 90 uniformly distributed diffusion encoding directions for each shell were optimised according to Caruyer et al. (2013). The diffusion run included also a structural T1w reference scan at $1.25\,\mathrm{mm}$ isotropic resolution.

The minimal pre-processing pipeline for diffusion images included:

- intensity normalisation across scans;
- TOPUP for EPI distortion correction (Andersson et al., 2003; Smith et al., 2004);
- EDDY for eddy currents and motion correction (Andersson & Sotiropoulos, 2016);
- correction for gradient non-linearity and calculation of gradient b-value and b-vector deviation;
- linear registration of mean b=$0\,s/mm^2$ volume to native $1.25\,\mathrm{mm}$ T1w reference image;
- registration of diffusion data, gradient deviation data and gradient directions to $1.25\,\mathrm{mm}$ T1w reference image;

- brain extraction and creation of brain binary mask.

The pre-processing pipeline for structural images consisted in:

- correction for gradient distortion;
- rigid registration of T1w and T2w images;
- brain extraction;
- field map distortion correction;
- bias field correction;
- registration to MNI 152 standard space.

2.2.2 Image processing

Diffusion images were inspected for image quality assessment. High resolution T1w and T2w structural images were down-sampled and registered to $1.25\,\mathrm{mm}$ T1w space (registered to diffusion images). Both T1w and T2w images were provided to SPM[1] for accurate tissue segmentation using tissue probability maps provided by Lorio et al. (2016), which were optimised to produce a more accurate delineation of subcortical grey matter (GM) structures including DCN.

Diffusion data were then processed to fit different models of the diffusion signal. The constrained weighted linear least squares method (Veraart et al., 2013) is here used to fit the diffusion tensor model (Basser & Pierpaoli, 2011) and to compute the excess kurtosis (Jensen et al., 2005; Jensen & Helpern, 2010). Maps of axial diffusivity (AD), radial diffusivity (RD), mean diffusivity (MD) and FA were produced from the diffusion tensor, while measures of kurtosis were axial kurtosis (AK), radial kurtosis (RK) and mean kurtosis (MK).

Kurtosis measures are highly susceptible to noise that can produce high amplitude outliers in the resulting parameter maps. Therefore, following suggestions given by Jensen et al. (2005); Jensen & Helpern (2010), a gaussian smoothing kernel was applied ($\mathrm{FWHM} = 1.2 \times voxel\ size$) and the range of acceptable values was set between 0 and 4.

We also computed the per-shell spherical mean of the diffusion signal across directions and the normalised spherical mean (divided by the b=$0\,\mathrm{s/mm^2}$ image). The T1w/T2w ratio was also computed.

2.2.3 Cerebellum analysis

Since our interest focused on the cerebellum, this structure was isolated using the dedicated SUIT[2] (Diedrichsen, 2006) tools implemented within SPM and MATLAB[3]. The cropped cerebellum was then registered to the SUIT template and the inverse transformation was computed. This last step allowed us to bring cerebellar atlases to the native

[1] `http://www.fil.ion.ucl.ac.uk/spm`
[2] `http://www.diedrichsenlab.org/imaging/suit.htm`
[3] The MathWorks, Inc., Natick, MA. `https://www.mathworks.com`

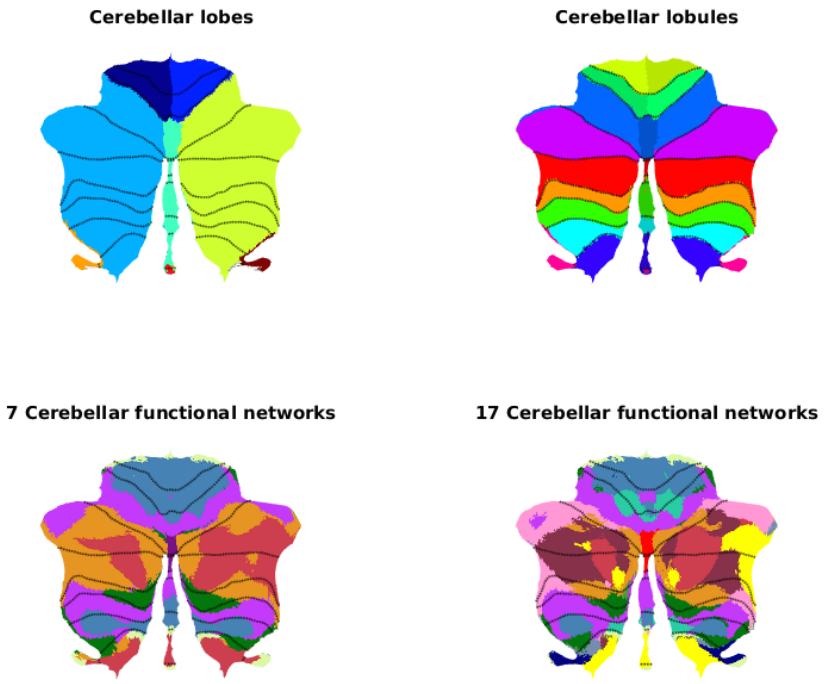

Fig. 2.1: Atlases of the cerebellar cortex. The flattened anatomical (top row) and functional (bottom row) atlases of the cerebellar cortex are shown.

cerebellar space of each subject and to label cerebellar anatomical substructures. In particular, we considered:

- the anatomical parcellation of the cerebellar GM (Diedrichsen et al., 2009): here the cerebellar cortex is divided into lobules and each lobule is further divided into vermal and left and right hemispherical components (28 regions);
- the functional atlas of the cerebellum (Buckner et al., 2011; Yeo et al., 2011): this is based on resting state blood oxigenation level dependent (BOLD) fMRI results and it comes in two versions dividing the cerebellum in 7 or 17 distinct functional regions respectively.

The anatomical atlas of cerebellar GM was edited to label also a coarser subdivision of the cerebellar cortex: lobules were merged in order to create a mask for the anterior, posterior and flocculonodular lobes; the subdivision into vermis and left and right hemispheres was maintained, thus totalling 8 regions. These cerebellar atlases are illustrated in Fig. 2.1.

Atlases, along with segmentation maps were used to compute region-specific average values of the different measures. In particular, in order to avoid as much as possible partial volume effects, a 90% threshold was applied to resulting probability maps of tissue segmentation prior to computing the regional average values.

Region-specific average values were computed for each subject in its cerebellar native

space. These average values were provided to a T-test for independent samples with unequal variance, which was performed to detect significant differences between regions of the same atlas.

Microstructural maps of each subject were then registered to SUIT standard space by applying the inverse of the transformation used to register atlases to subject native space. We were then able to produce across-subjects average microstructural maps.

2.2.4 Clustering

In order to produce an automated classification of voxels based on similarity of microstructural properties, we ran a data-driven K-means clustering algorithm. This was used for microstructural segmentation of cerebellar cortical GM.

Given the spatial resolution of the current protocol and because of cerebellar anatomical organization in thin folia, where WM fibres are surrounded by GM convolutions, the risk of partial volume effects is relevant. The SUIT toolbox provides tools for surface mapping of the cerebellum: in particular, the external surfaces of cerebellar GM and WM are used to map data from those voxels lying between them at desired depth. In order to reduce partial volume effects with inner cerebellar WM and outer cerebro spinal fluid (CSF) we considered only the layer in the depth range between the outer 10% and 30% of the cerebellar GM, where, if present, the relative volume of WM and CSF should be limited.

Variables with wider range of values have higher impact on clustering and contribution from other variables would be obscured; therefore, each variable was previously normalised and then different combinations of variables were selected. The clustering algorithm was set to produce two, three or four clusters for each combination of variables and for each subject. The combinations of variables used for clustering were chosen building up from basic images acquired in most clinical protocols and adding diffusion parameters. The chosen combinations are reported in Tab. 2.2. The clustering of the cerebellar cortex performed by providing all the variables was set to produce also five, six and seven clusters.

Corresponding clusters of voxels were finally averaged across subjects to produce a probability map of each cluster (see Fig. 2.11 for an example).

2.3 Results

2.3.1 Image quality

The inspection of diffusion images revealed that many subjects were affected by artefacts induced by susceptibility gradients even after TOPUP correction. These artefacts appeared as distortions and signal loss and they were considered an issue when they involved the cerebellum and/or the pons. Such artefacts were detected in 24 out of 100 subjects, which were discarded from subsequent analysis. Fig. 2.2 reports few examples of such distortions.

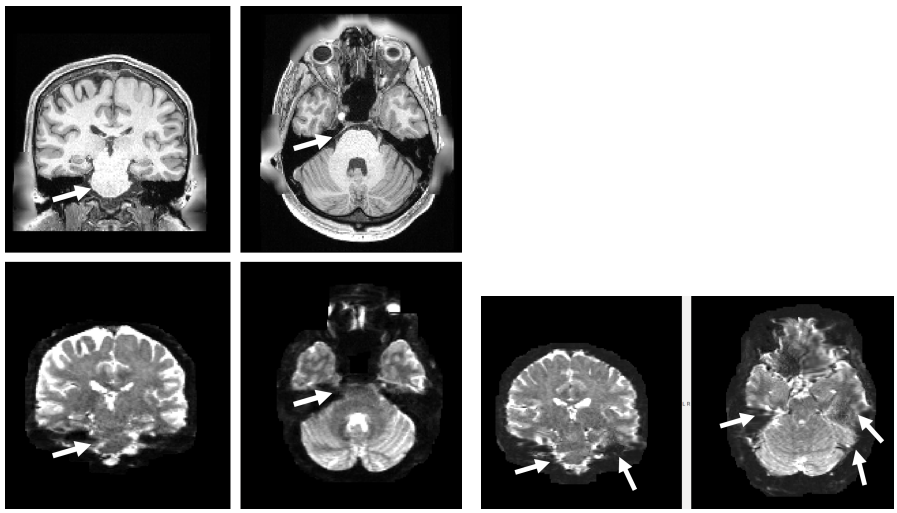

(a) (b)

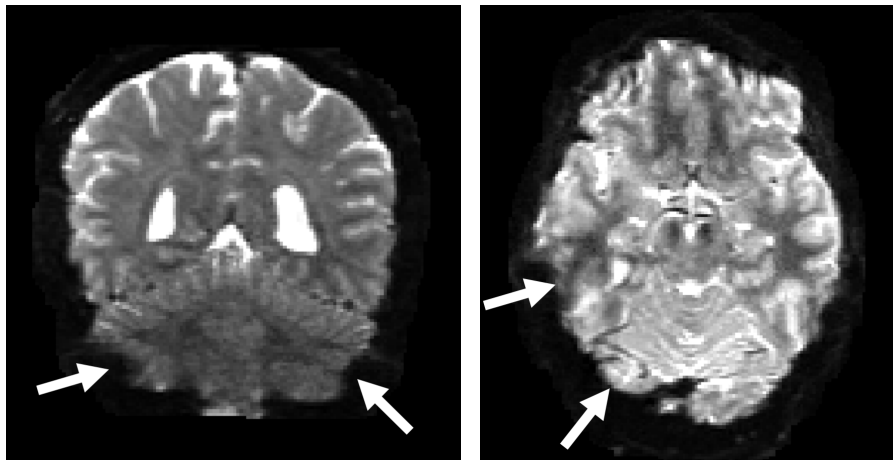

(c) (d)

Fig. 2.2: Susceptibility-induced artefacts in the cerebellum. These examples are shown in b=0 $\mathrm{s/mm^2}$ images and they are taken from four different subjects. For one subject (a) the corresponding T1w images are shown for undistorted anatomical reference. White arrows point at artefacts, which can take the form of distortions in the pons (a, b), distortions in the cerebellar hemispheres (b, d) or signal loss in the cerebellar hemispheres (c). The temporal lobes can also be affected (b, d).

Var. combination	T1w	T2w	T1w/T2w	b=0 s/mm^2	sph. mean	DTI	DKI
1	•	•					
2	•	•	•				
3	•			•			
4				•	•		
5						•	
6							•
7	•	•		•	•		
8	•	•				•	
9	•	•					•
10						•	•
11	•	•	•	•	•	•	•

Tab. 2.2: Combinations of MRI variables considered for K-means clustering of the cerebellar cortex. The number in the left column identifies the combination, while dots indicate the variables included in that combination. For combination from 1 to 10 up to four clusters were produced. For combination 11 K-means was set to produce up to seven clusters. Here, DTI indicates that AD, RD, MD and FA were used, while DKI indicates the use of AK, RK, MK maps.

2.3.2 Segmentation

Fig. 2.3 reports results of the two-input tissue segmentation for one subject as an example. The resulting tissue probability maps are shown with 90% lower threshold, which is subsequently used as a binary mask for computation of regional average microstructural values.

Despite the adopted precautions, some inaccuracies can still be observed. In particular, it can be seen that the WM bundle intruding a folium is erroneously labelled as GM even though a high (90%) threshold was set (see Fig. 2.3a and c); however, given the high inter-subject variability of folia position, tissue probability maps priors can only account for those WM bundles whose location is most reproducible, and, therefore, our results are not surprising. Unfortunately, this leads to unavoidable partial volume effects and errors when computing regional average microstructural values.

The second error concerns the DCN: deep-GM structures are clearly visible as hypointense regions with T2w contrast. Despite the use of the T2w image as second segmentation input and the use of dedicated tissue probability maps priors, most of DCN are marked as WM (see Fig. 2.3b and c, where the dentate nuclei are shown in virtue of their size).

2.3.3 Diffusion modelling

Fig. 2.4 show results for a single subject, while Fig. 2.5 show across-subjects averaged maps in SUIT standard space.

In particular, Fig. 2.4a and Fig. 2.5a show T1w, T2w and T1w/T2w ratio; Fig. 2.4b

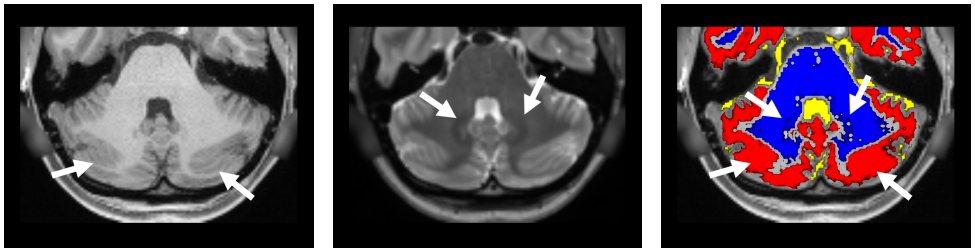

(a) (b) (c)

Fig. 2.3: Cropped cerebellum and segmentation. The cropped T1w (a) and T2w (b) images are shown. Tissue segmentation with 90% threshold for each tissue type is shown in (c). Red: GM; blue: WM; yellow: CSF. Arrows point at imperfections in segmentation corresponding to the WM layer intruding a folium, which is erroneously labelled as GM (a and c), and to DCN (clearly visible with T2w contrast) that are marked as WM (b and c).

and Fig. 2.5b show b=0 $\mathrm{s/mm^2}$ and per-shell spherical mean of the diffusion signal (the second row shows the normalised spherical mean obtained by dividing the spherical mean image by the b=0 $\mathrm{s/mm^2}$ image and values represent the percentage signal).

Fig. 2.4c and Fig. 2.5c show the parameters derived from the diffusion tensor (first row) and kurtosis (second row) models. Fig. 2.6 show the respective flatmaps of the cerebellar cortex.

Since observations on cerebellar microstructure retrieved in existing literature refer preferentially to coarser subdivisions of the cerebellar cortex (*e.g.* lobes rather than lobules), and given the macroscopic differences observed in the average maps, we decided to focus on the subdivision of the cerebellar cortex in 8 lobes and 7 resting-state functional networks for subsequent analysis rather than addressing also the lobular atlas and the 17 networks map (see Fig. 2.1a).

2.3.4 Regional analysis

Regional analysis of the cerebellar cortex was performed using the above-mentioned atlases and segmentation masks. Here, we report only results obtained using the atlas of lobes (see Fig. 2.7 and Fig. 2.8) and the atlas of 7 resting-state functional networks (see Fig. 2.9 and Fig. 2.10). Boxplots show the median and the 25^{th} and 75^{th} percentiles of the distribution of regional average values from 76 subjects. Each second row of plots reports a table with results from T-test referring to boxplots in the preceding row: a red box indicates that the difference between values of the two regions is not statistically significant; a grey box represents a significant difference with $\mathrm{p} < 0.05$ and a black box represents a significant difference with $\mathrm{p} < 0.01$.

Cerebellar lobes Here are summarised the main results that can be evinced from regional analysis when considering the atlas of cerebellar lobes.

- T1w and T2w images show that the posterior lobe has significantly different values

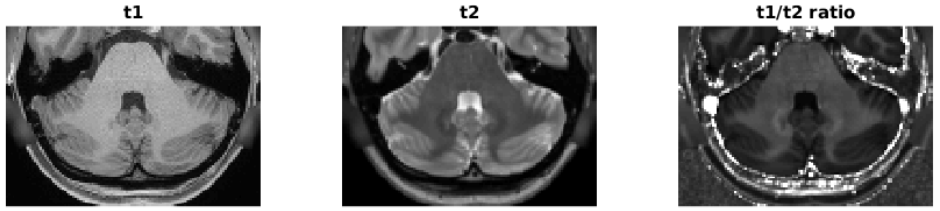

(a)

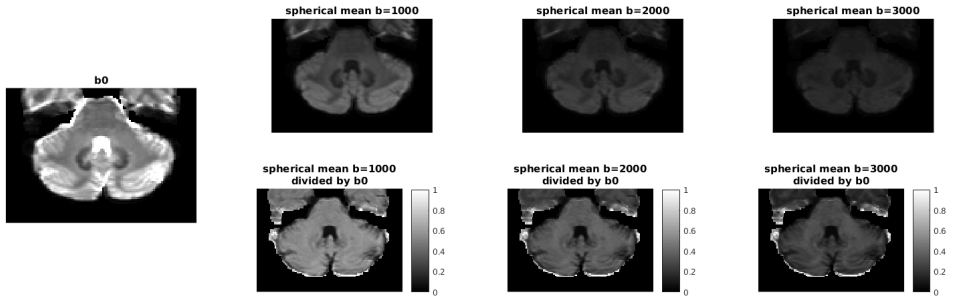

(b)

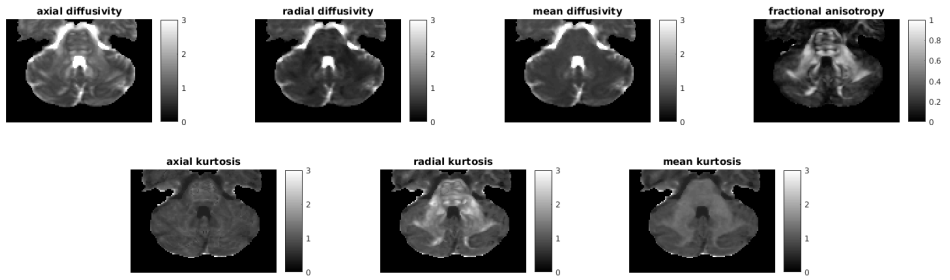

(c)

Fig. 2.4: Cropped microstructural maps of the cerebellum for a single subject in the native space. (a) reports T1w (left), T2w (middle) and T1w/T2w ratio (right) images. (b) reports the average b=$0\,\mathrm{s/mm^2}$ image (isolated on the left), while the following three vertical pairs of images show the spherical mean of the diffusion signal at b=$1000\,\mathrm{s/mm^2}$ (left), b=$2000\,\mathrm{s/mm^2}$ (middle) and b=$3000\,\mathrm{s/mm^2}$ (right). The first row shows the spherical mean of the diffusion-weighted images, while normalised maps (divided by the average b=$0\,\mathrm{s/mm^2}$ image) are shown in the second row. (c) reports the maps of measures derived from the diffusion tensor (first row) and those derived from the estimate of the diffusional kurtosis.

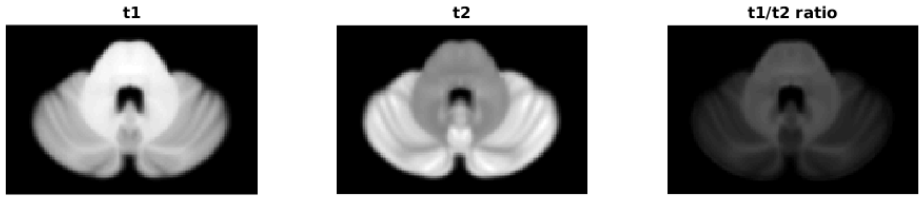

(a)

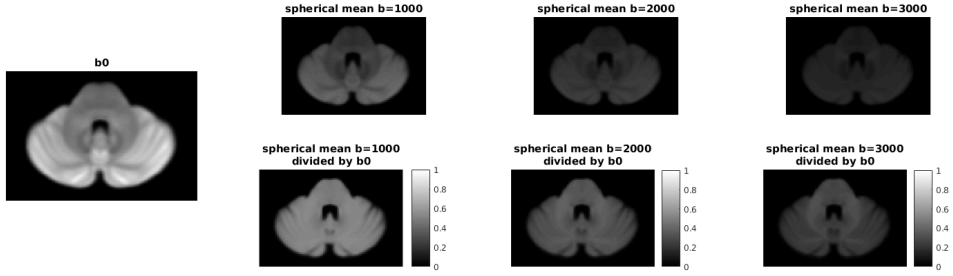

(b)

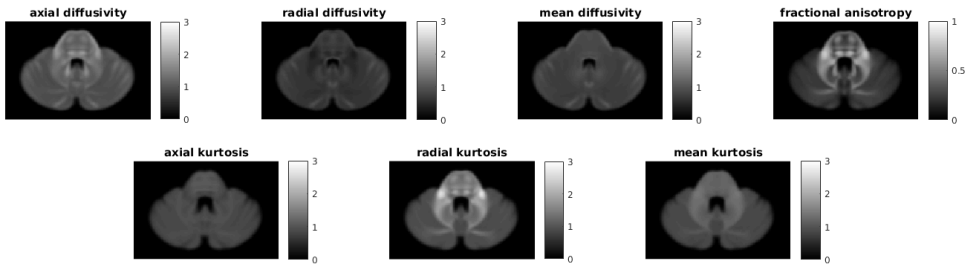

(c)

Fig. 2.5: Microstructural maps of the cerebellum averaged across all subjects in the SUIT standard space. The microstructural parameters reported here are the same shown in Fig. 2.4 and they are reported in the same order.

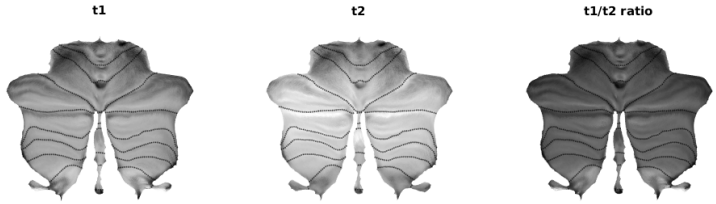

(a)

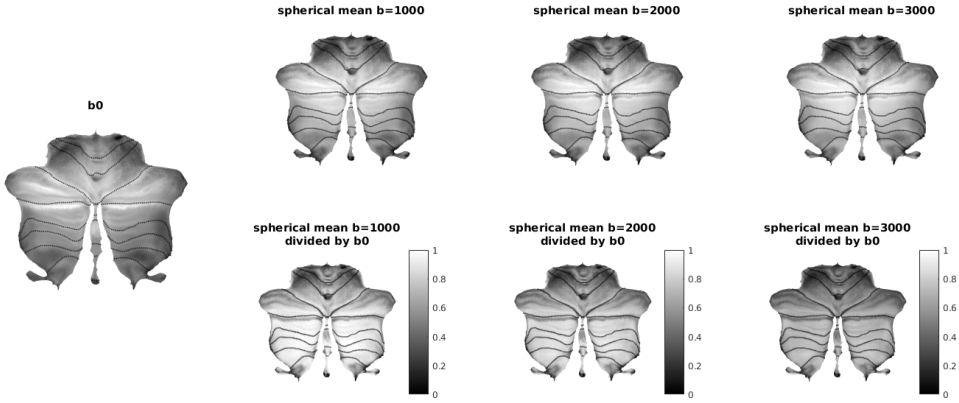

(b)

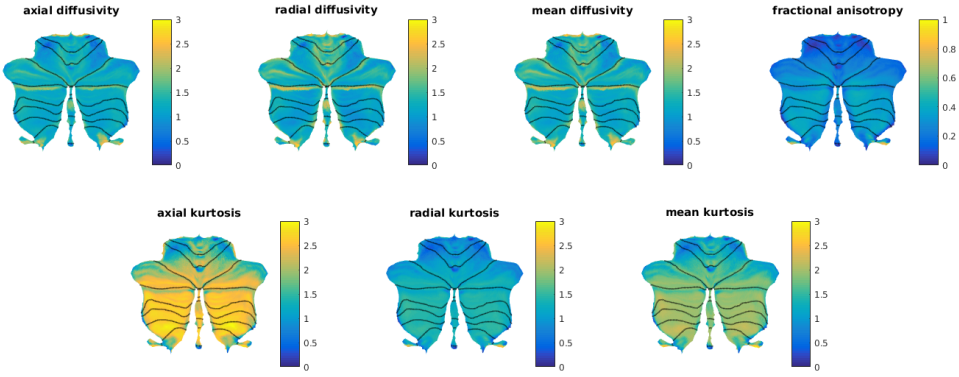

(c)

Fig. 2.6: Flatmaps of the cerebellar cortex showing average microstructural parameters. The microstructural parameters reported here are the same shown in Fig. 2.4 and they are reported in the same order.

with respect to other lobes (anterior and flocculonodular); on average left, right and vermal regions of the same lobe show no (or lower) significant differences.

- T1w/T2w ratio adds little information with respect to previous images.
- The T2w contrast provided by b=$0\,\mathrm{s/mm^2}$ images better differentiates the flocculonodular lobe from the other ones; moreover, the vermis is significantly distinguished from the corresponding left and right regions.
- The per-shell normalised spherical mean of the diffusion signal show that significant differences are observable between most regions. The comparison of average values with increasing diffusion weighting highlights different trends in the decay of the diffusion signal. In particular, from boxplots it is possible to observe a progressive flattening of the average values when going from b=$1000\,\mathrm{s/mm^2}$ to b=$3000\,\mathrm{s/mm^2}$, thus showing, for example, a faster signal decay in regions of the posterior lobe of the cortex (this is also confirmed by increasing occurrence of grey and red cells in the corresponding tables). Moreover, it should be noted the peculiar behaviour of the vermal flocculonodular lobe with respect to corresponding regions in the hemispheres: it exhibits significantly higher values at b=$0\,\mathrm{s/mm^2}$ (in the previous plot) and b=$1000\,\mathrm{s/mm^2}$, while it is not significantly different from the hemispheres at b=$2000\,\mathrm{s/mm^2}$ and it becomes significantly lower at b=$3000\,\mathrm{s/mm^2}$, thus meaning a faster decay with increasing diffusion weighting. As for the vermis of the posterior lobe, it can be noted that the spherical mean of the diffusion signal is always significantly lower than in the corresponding regions in the hemispheres, while the opposite is true at b=$0\,\mathrm{s/mm^2}$. However, it should also be noted that vermal regions are made by small number of voxels with respect to the hemispheres (in particular in the case of the posterior lobe) and this could result in higher inter-subject variability due to imperfections in atlas registration.
- Measures of diffusivity derived from the diffusion tensor show consistent and significant inter-lobe differences. AD and MD of the vermis are significantly different from the hemispheres in both the posterior and flocculonodular lobes. FA values in the vermis are systematically lower than in the corresponding hemispheres.
- Measures of excess kurtosis (RK and MK in particular) show significant differences between the vermis and the hemispheres. All kurtosis measures show significant differences between the flocculonodular lobe and the other ones.

Cerebellar functional networks Here are summarised the main results that can be evinced from regional analysis when applying the functional parcellation of the cerebellum based on resting-state connectivity.

- From T1w and T2w images the cerebellum appears divided in three distinct groups of regions. The first group is made by those regions associated with sensory and motor resting-state networks, *i.e.* the visual network (VN) and the somatomotor network (SMN). The second is constituted by regions that are mostly involved

in cognitive networks (dorsal attention (DAN), ventral attention (VAN), fronto-parietal control (FPCN) and default mode network (DMN)). Within each group no significant difference is observed. Values of regions associated with the limbic network (LN) are significantly different from all other regions.

- T1w/T2w ratio mostly confirmed the results obtained from T1w and T2w images.
- The contrast provided by b=$0\,\mathrm{s/mm^2}$ images makes most networks significantly distinguished and it makes the functional categorisation of groups of networks more challenging. However, the LN remains the network with the most peculiar values.
- From the point of view of the diffusion signal, significant differences are found between spherical mean values of most networks, but the situation appears much more homogeneous if compared to corresponding measures of cerebellar lobes. Looking at boxes, the relative mutual position is conserved across shells for all networks apart from the LN, which exhibits a slower signal decay with increasing b-values. The group of networks with the most similar distribution of average values are VN, VAN, FPCN and DMN, which are the networks that occupy most of the cerebellar posterior lobe.
- Measures of diffusivity from DTI gather again VN, VAN, FPCN and DMN as networks with similar values and the networks with most peculiar values are SMN and LN. Values of FA are significantly different between almost all networks.
- AK and RK show very different patterns that are then reflected in MK. AK divides the networks in two groups: the first one made by VN, SMN, DAN, VAN and LN, while the second one is constituted by FPCN and DMN. RK isolates VN, LN and FPCN, while the other networks share similar values. Finally, the LN shows significantly higher MK values than other networks, while the DMN has significantly lower values than the rest of networks. All other networks share similar MK.

2.3.5 Clustering

Clustering results are illustrated in Fig. 2.12, 2.13 and 2.14. Each row illustrates the flatmap of the cerebellar cortex divided in two, three and four clusters based on the variables indicated above each plot and in Tab. 2.2. There is no deliberate correspondence of colours between plots.

The first general considerations regard the choice of combinations of variables. DTI metrics seem to be the least capable to distinguish different subregions of the cerebellar cortex. In fact, independently of the total number of clusters required, one of them is always dedicated to smaller details, while the remaining clusters cover most of the cortex. Since T1w/T2w ratio depends on T1w and T2w values, it adds little information and this is confirmed by clustering results (compare the first and second row of plots in Fig. 2.12). Very different combinations of variables can provide extremely similar results as, for example, in the second and third rows in Fig. 2.13, which represent respectively

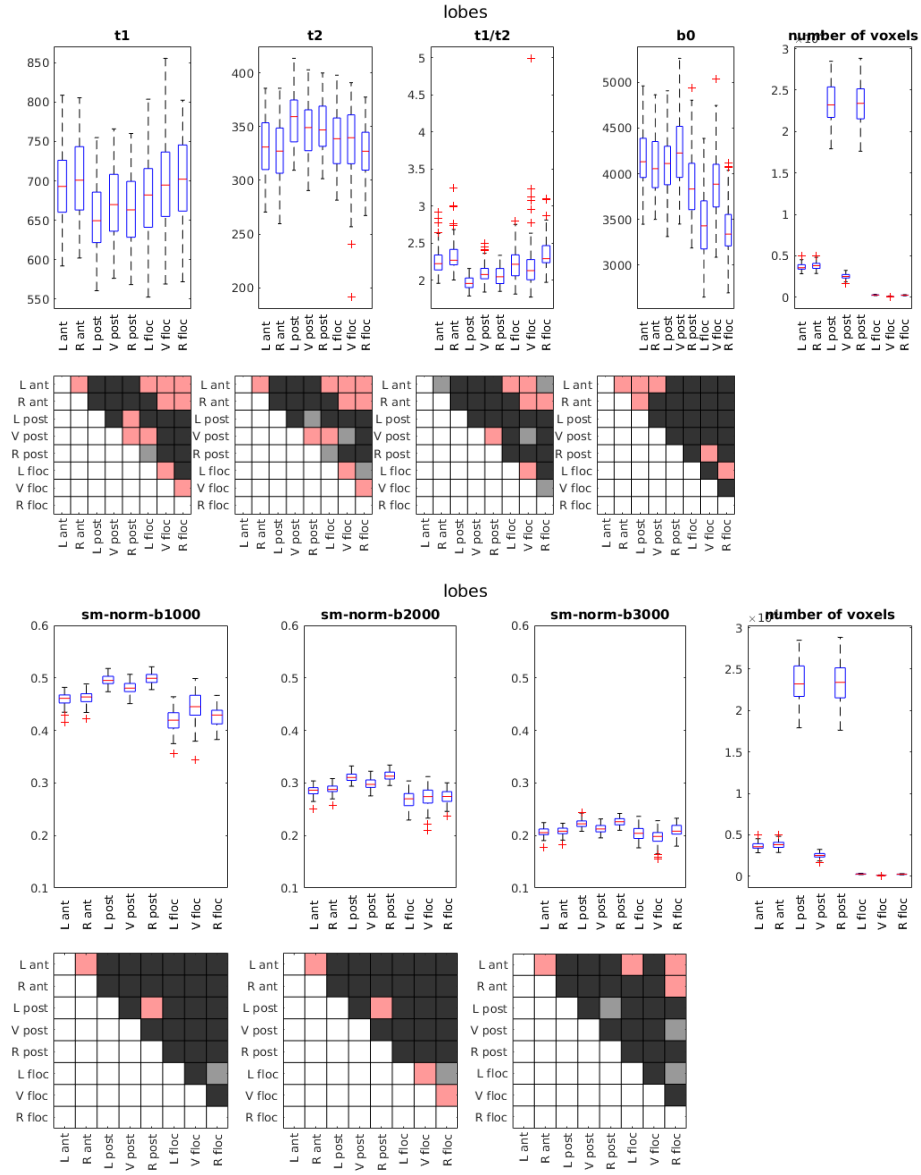

Fig. 2.7: Regional average values for regions of the atlas of cerebellar lobes. They are computed for each region of each subject in its native space. Here are reported results for T1w, T2w, T1w/T2w, b=0 $\mathrm{s/mm^2}$ and spherical mean images. Each first row reports boxplots of such regional average values from all subjects. In each box the red line represents the median across all subjects, while the box edges represent the 25^{th} and 75^{th} percentiles. Each boxplot refers to the variable reported above it. Each last boxplot reports the number of voxels included in each region. Tables in each second row of plots report T-test results corresponding to the boxplots immediately above. Each row and column of a table represents a region of the atlas. The entry at the intersection of two regions is coloured in red if the difference between their across-subjects mean values is not statistically significant. Grey and black entries indicate that the difference is statistically significant. Grey is for $\mathrm{p} < 0.05$, while black indicates $\mathrm{p} < 0.01$.

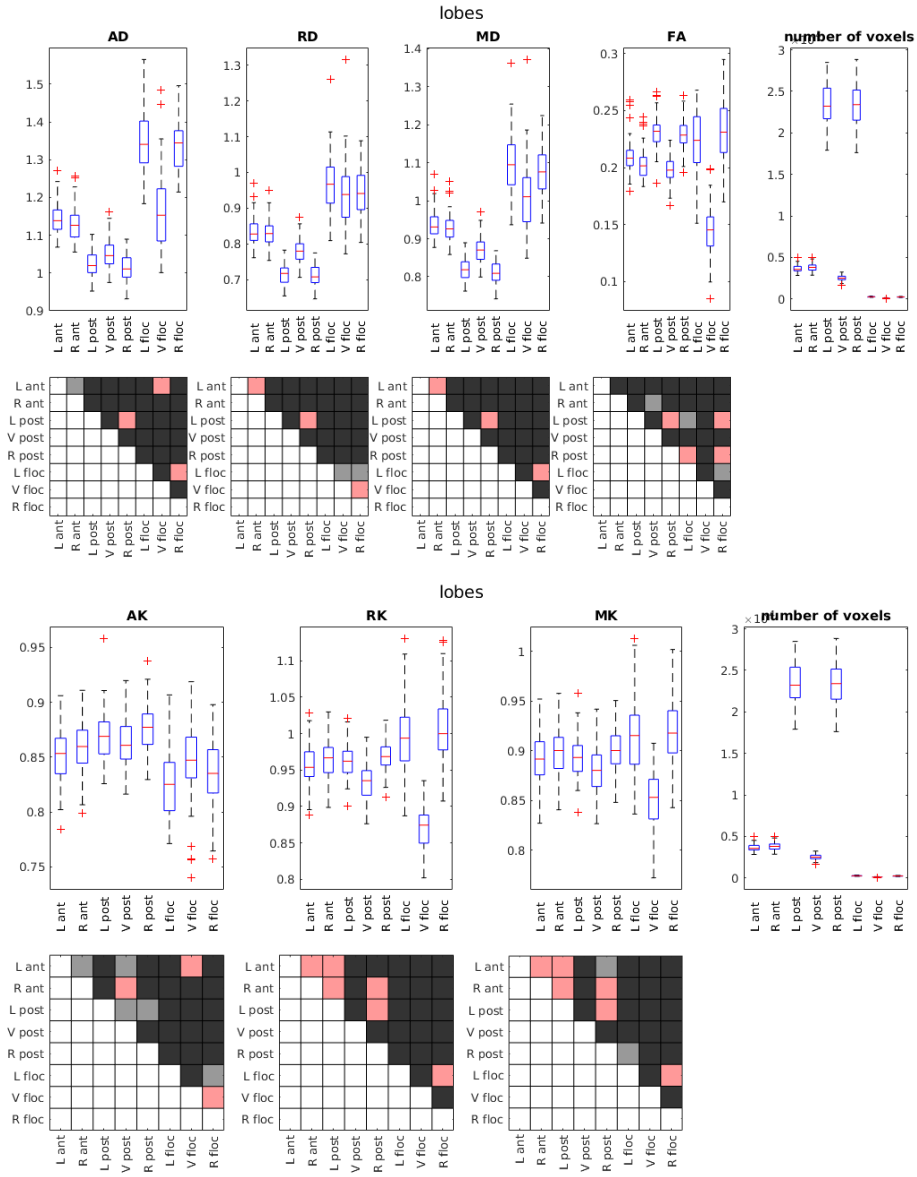

Fig. 2.8: Regional average values for regions of the atlas of cerebellar lobes. Refer to Fig. 2.7 for detailed explanation. Here are reported results for diffusion tensor and diffusional kurtosis measures.

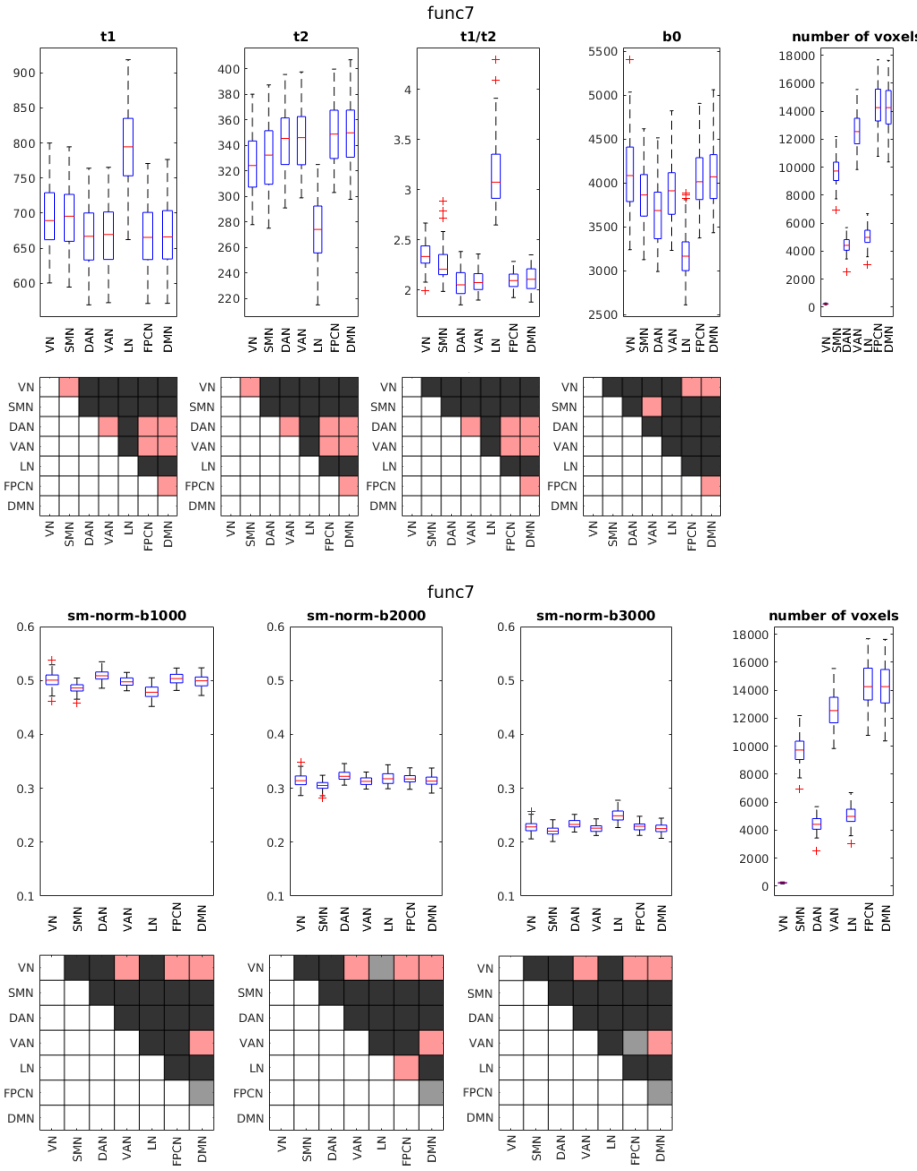

Fig. 2.9: Regional average values for regions of the functional atlas of the cerebellar cortex. Refer to Fig. 2.7 for detailed explanation. Here are reported results for T1w, T2w, T1w/T2w, b=0 $\mathrm{s/mm^2}$ and spherical mean images.

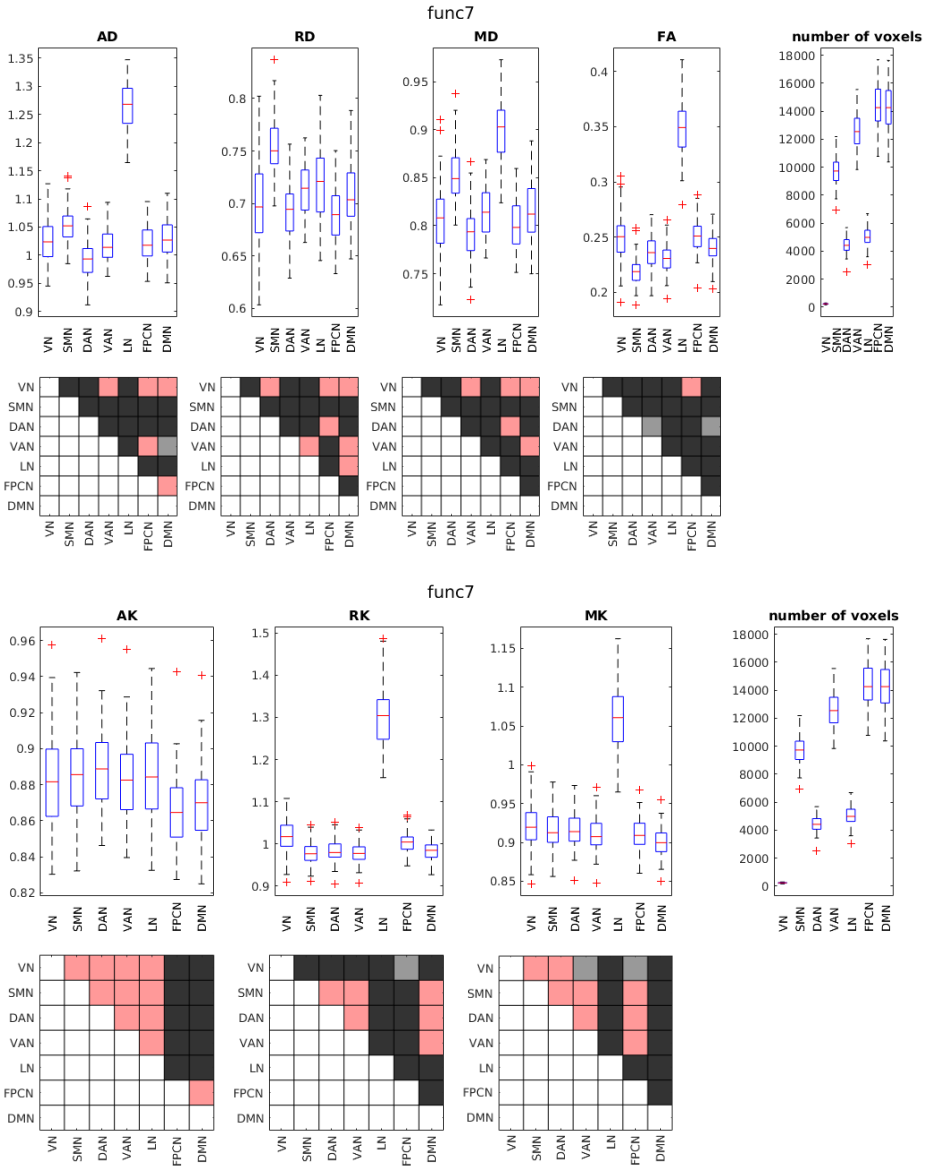

Fig. 2.10: Regional average values for regions of the functional atlas of the cerebellar cortex. Refer to Fig. 2.7 for detailed explanation. Here are reported results for diffusion tensor and diffusional kurtosis measures.

clustering based on DKI measures alone and clustering based on T1w, T2w, b=$0\,\mathrm{s/mm^2}$ and normalised spherical mean images.

It can be noted that, with the exception of DTI metrics, all combinations of variables provide a similar subdivision in two clusters: the first cluster includes the lateral regions of the anterior lobe, the lateral regions of lobule VI, Crus I and lobule IX and part of lobule X. The second cluster covers the rest of the cerebellum.

The subdivision into three clusters can highlight more differences. In most cases, one cluster identifies the most lateral parts of the anterior lobe and of lobule VI and, occasionally, of Crus I along with the vermal region of lobule X. The second cluster is generally composed by the medial region of the anterior lobe, most of lobule VI, the superior part of Crus I, by half of the vermal region of lobule VIIIa and by the inferior part of lobule IX. The last cluster consists in the remainder regions of the cerebellar cortex, which correspond to most of the posterior lobe starting from the inferior part of Crus I to most of lobule IX. Exceptions to this scheme are two combinations of variables that involve DTI metrics, where the second cluster is strongly reduced leaving more space for the third one. Finally, for the T1w + b=$0\,\mathrm{s/mm^2}$ combination, the second cluster is much more circumscribed and it covers the medial regions of lobules V and VI and most of Crus I and Crus II.

The four-cluster subdivision is the one that provided most heterogeneous results. The first cluster generally comprehends the lateral regions of the anterior lobe and of lobule VI and the vermal part of lobule X. The second cluster usually extends from the medial regions of the anterior lobe, to a stripe in lobule VI to the lateral part of Crus I; when considering DTI parameters alone this cluster covers also the medial region of lobule VI. The third cluster mainly covers the medial region of lobule VI and Crus I and th vermal region of lobule VIIIa; when considering the T1w + b=$0\,\mathrm{s/mm^2}$ combination, this cluster includes also most of Crus II; when considering the T1w + T2w (+T1w/T2w) combination, this cluster extends to the boundary of lobule VIIIb. Therefore, the fourth cluster corresponds to most of the posterior lobule, apart in the T1w + T2w (+T1w/T2w) case where it is limited to lobules VIIIb and IX. The classification of lobule IX lateral regions is not consistent across different combinations.

Finally, the use of all variables and the concomitant subdivision in more than four clusters give a guideline to summarise the most reproducible features:

- the anterior lobe and lobule VI can be divided into multiple medio-lateral regions (when asking for seven clusters, four regions can be distinguished in lobules I-IV and up to 5 different regions in lobule V);
- a recurrent block is constituted by the medial region of lobule VI, by the superior part of Crus I and by the vermal region of lobule VIIIa;
- the cluster that extends from the inferior part of Crus I to lobule VIIIb-IX is consistently reproducible across combinations and with different number of clusters;
- multiple medio-lateral regions can be distinguished in lobules IX and X.

Moreover, in case of seven clusters, one of them is dedicated to lobule VIIIb and considerable parts of lobules IX and X.

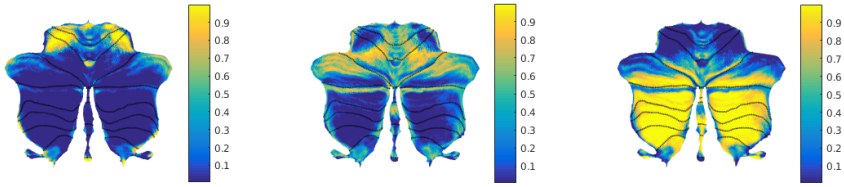

Fig. 2.11: Population probability maps of clusters. These maps were produced by averaging categorical cluster maps across all subjects. In this case the K-means algorithm was set to produce three clusters based on all variables as shown in combination 11 in Tab. 2.2.

2.4 Discussion

Following the recently proposed hypothesis that cellular inhomogeneities within the cerebellar cortex can affect cerebellar circuitry and function, we investigated the cerebellum with MRI measures sensitive to microstructure and cyto-architecture. Here are discussed the main findings reported in the previous section.

As mentioned in Sec. 2.1, previous studies mainly investigated and found differences between the anterior, posterior and flocculonodular lobes of the cerebellar cortex and between the vermis and the hemispheres. Therefore, in order to compare our results with existing literature, we decided to focus on this coarser anatomical parcellation, rather than addressing individual cerebellar lobules.

Our results indicate that MRI measures here considered are sensitive to microstructural features of cerebellar tissues. The measures we chose are sensitive to iron and myelin content (T1w, T2w and T1w/T2w ratio images (Fukunaga et al., 2010; Glasser & Van Essen, 2011)) and to diffusion properties of water molecules moving in different microanatomical domains. Tensor modelling of the diffusion signal at the voxel level is informative about the principal direction of neurites within the voxel and estimates the apparent diffusion coefficient. Diffusional excess kurtosis quantifies the deviation from mono-exponential decay, and therefore the departure from gaussian behaviour of water molecules, due to tissue microscopic structures like membranes and compartments.

Firstly, the following consideration is due: anomalous values are found in flatmaps in correspondence of fissures between lobules (see Fig. 2.15, purple) and between folia (red) and in correspondence of WM layers inside major folia and gyrifications (yellow), signalling partial volume effects that can affect following regional measures. Therefore, further studies with higher resolution are recommended to better resolve folia and GM and WM regions and to improve tissue specificity of measured values. However, the intensity gradient characterising all inhomogeneities listed below does not exhibit the same degree of sharpness found at the level of fissures and they can be found in regions that are not consistent with anatomical structures like fissures and gyri.

Apart from fissures between lobules, our results show relevant inhomogeneities and suggest that the cerebellar cortex may not be considered uniform also for MRI measures. In particular, in most cases it is possible to note that the cortex can be macroscopically divided into three transversal regions (see Fig. 2.6). The transition from one region to the next one can be characterised by a different degree of sharpness depending on the

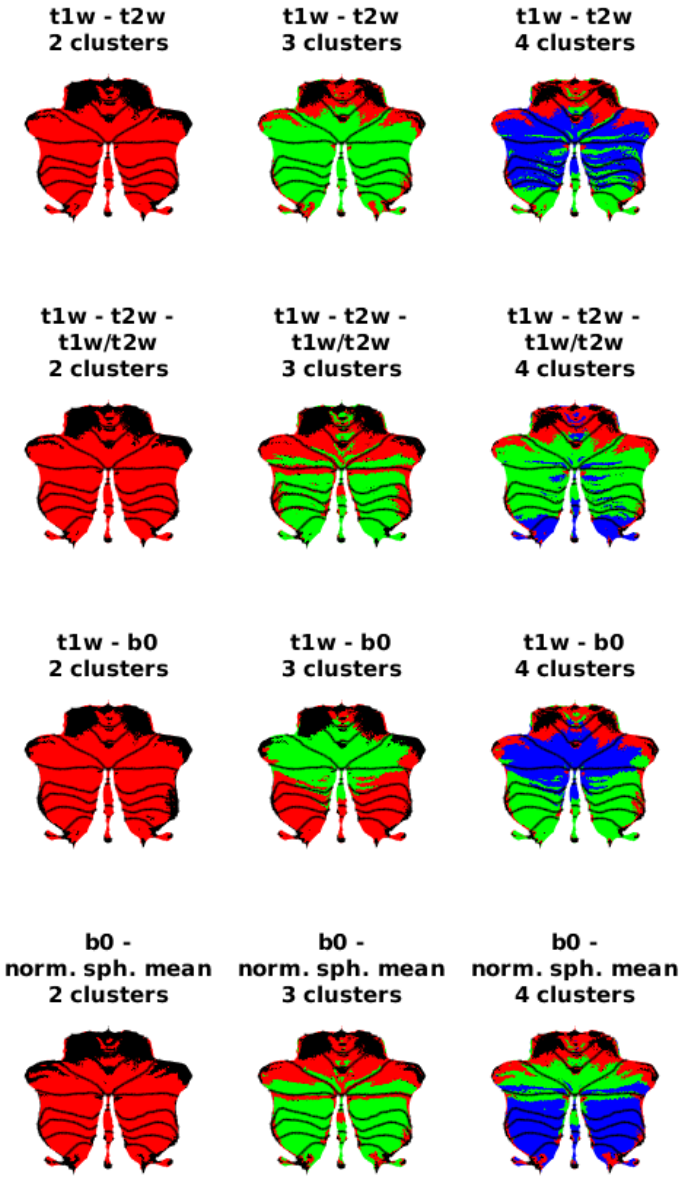

Fig. 2.12: Flatmaps showing the categorical subdivision of the cerebellar cortex into clusters. After averaging categorical cluster maps across all subjects to produce the population probability map of each cluster, each point of the map is assigned to the cluster showing the highest probability value in that point. Each row reports results from a specific combination of variables. The variables considered and the number of clusters are reported above each map. Combinations are shown in the same order reported in Tab. 2.2. Here are reported combinations from 1 to 4.

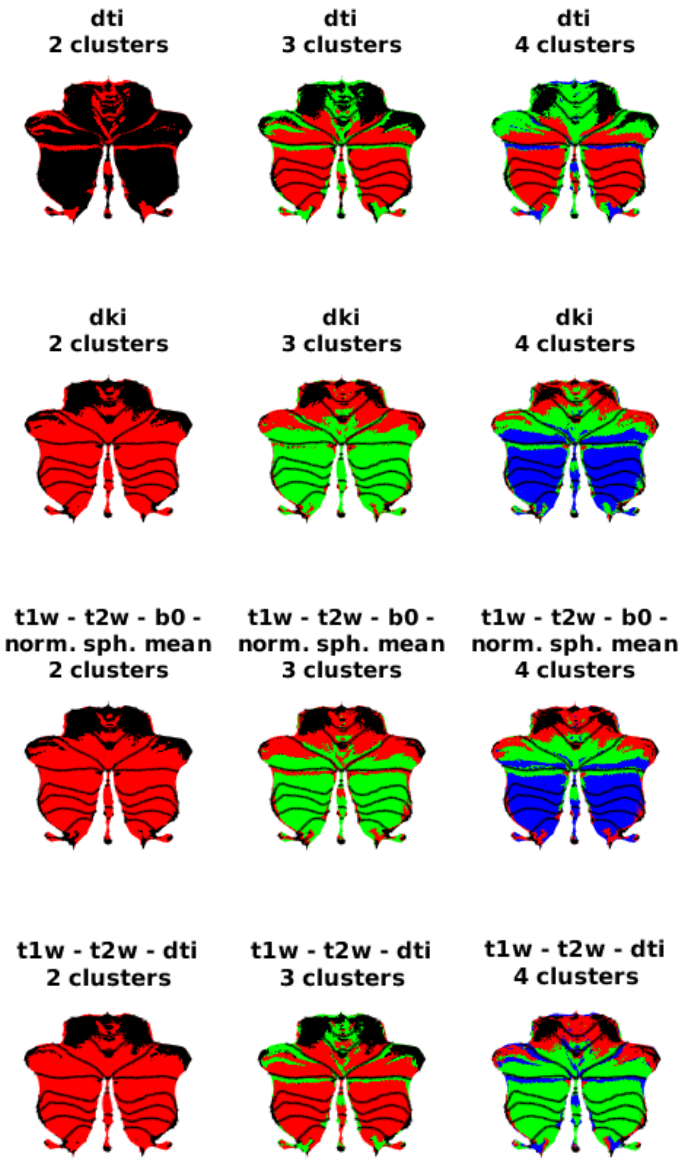

Fig. 2.13: Flatmaps showing the categorical subdivision of the cerebellar cortex into clusters. The pipeline followed is the same as for Fig. 2.12. Here are reported combinations of variables from 5 to 8 of Tab. 2.2.

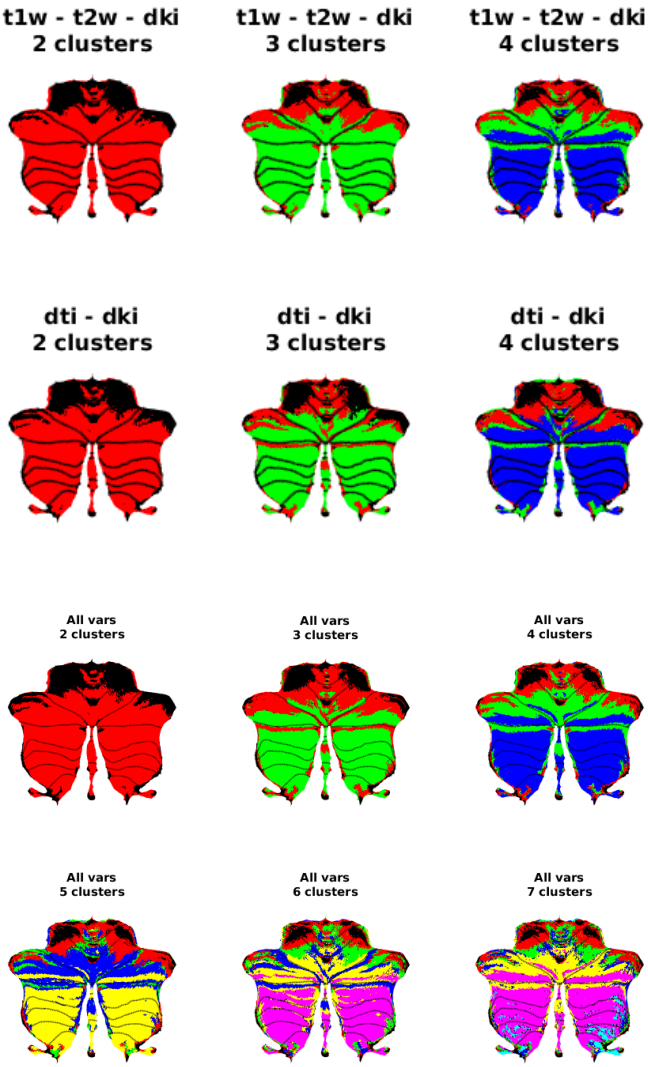

Fig. 2.14: Flatmaps showing the categorical subdivision of the cerebellar cortex into clusters. The pipeline followed is the same as for Fig. 2.12. Here are reported combinations of variables from 9 to 11 of Tab. 2.2. For combination 11, the third and the fourth rows of maps report the subdivision into 2, 3 and 4 and 5, 6 and 7 clusters respectively.

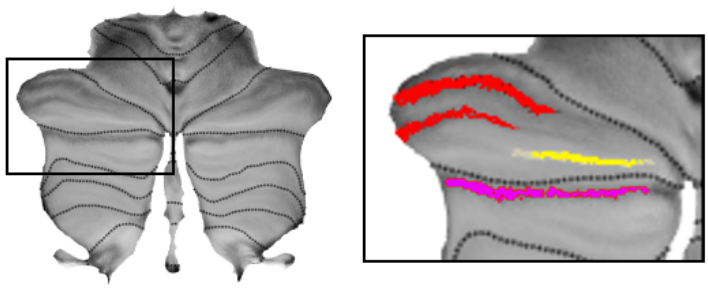

Fig. 2.15: Average T1w flatmap showing partial volume effects. These can be produced by CSF filling fissures between lobules (purple) and between folia (red). Yellow regions in the right plot correspond to WM fibres entering a folium.

specific map and its exact location may be different too. However, a general trend can be observed. Even though not in correspondence of the primary fissure that divides the anterior lobe from the posterior lobe, a first transition usually distinguishes the anterior regions of the cerebellum (including also part of lobule VI) from the posterior ones. A second transition is usually observed between lobules VIIIb and IX, thus dividing the posterior lobe of the cerebellum from a region that includes lobule IX and the flocculonodular lobe (lobule X). T-tests confirmed that in most maps the posterior lobe exhibits significantly different values from other regions and this coarse subdivision can also be visually observed in most maps, maybe with the exception of diffusivity measures derived from the diffusion tensor (Fig. 2.7 and 2.8).

Finer details can be observed when looking at intra-lobule inhomogeneities. The lateral regions of the anterior lobe and of lobule VI exhibits remarkably different values from medial regions of the same lobules. Intra-lobule inhomogeneities can also be observed in lobules IX and X, which show again a gradient when moving along the medio-lateral direction (*i.e.* parallel to the folium main axis).

Given the small representation size of the vermis it is generally harder to visually observe relevant differences between the vermis the hemispheres. However, in the case of lobules VIIIa and X differences may be even spotted between vermal and hemispheric regions (Fig. 2.6). Moreover, the vermal region of lobule VIIIa is nearly always divided in a superior and an inferior region (this is not much evident instead for FA, RK and MK).

It is interesting to note, that in two maps only (specifically b=$0\,\mathrm{s/mm^2}$ and AK) values in lobule VIIIb lie in a remarkably different range with respect to neighbouring regions and that the borders of this differently-intense regions (hypo-intense in the case of the b=$0\,\mathrm{s/mm^2}$ image and hyper-intense in the case of AK map) are extremely coherent with the anatomical delineation of the lobule.

Although many similarities are found between our results and those obtained from histological studies, a direct link between density of a specific cell population and MRI measures can not be established without reference histological data. Therefore, an interpretation of such differences is not straightforward, but further (though still specu-

lative) suggestions could come from a comparison between the above-mentioned inhomogeneities and the atlas of the 7 resting-state functional networks.

The first striking similarity concerns lobule VIIIb as seen in b=$0\,\mathrm{s/mm^2}$ and AK images: in the resting-state functional atlas of the cerebellum, hemispheric regions of lobule VIIIb are the only ones associated with the SMN in the posterior lobe. Within the posterior lobe, vermal regions involved in this network cover lobule VIIIb and the inferior half of lobule VIIIa, exactly where almost all of our maps show a discontinuity in values.

A further similarity concerns the coarser anterior - posterior subdivision, where the anterior region includes areas associated with the SMN (from lobule I to part of lobule VI) and the superior part of the VAN (lobule VI and the superior part of Crus I). The transition "line" is not clearly delineated in our maps (Fig. 2.6): looking for example at the T1w map, darker regions include the lateral regions of Crus I. However, given the shape and sharpness of dark lines, it looks plausible that signal hypo-intensity in these regions could originate from the presence of CSF between individual folia. Therefore, the "line" separating the two broad regions that we have located may be right above the border of lobule VI, thus corresponding to the border between the VAN and the FPCN. This result is in line with current knowledge of cerebellar functional topography that considers the anterior lobe mostly dedicated to motor functions and the posterior lobe mainly associated with cognitive functions (Stoodley & Schmahmann, 2010).

Finally, there is a strong similarity also in lobule IX, where darker regions in T1w and T2w maps correspond to areas associated with the DMN.

Results from group average of data-driven clustering individually performed for each subject depict a situation analogous to the discussed subdivision of the cerebellar cortex (Fig. 2.12, 2.13 and 2.14). However, even though the comparison between clustering results and the functional atlas of the cerebellum may show some resemblance between the two, it is clear that no network is microstructurally uniform across its whole extent. Despite this, it is interesting to note that, when considering four or more clusters, the superior part of vermal lobule VIIIa and the central region of lobule VI (two regions that are both involved in VAN) are often classified as part of the same cluster.

Eventually, attention should be paid to the anterior lobe. It is known from literature that lobules are characterised by longitudinal zones and stripes (Voogd, 2011; Cerminara et al., 2015). Boillat et al. (2018) investigated the cerebellar cortex with UHF quantitative mapping of T1 and T2*. They found a pattern of parasagittal regions with alternating levels of lower and higher T1 in the cortex of the anterior lobe. They hypothesised that T1 medio-lateral fluctuations may be caused by different myelin content, which could in turn be linked to the level of specific marker protein (like Zebrin II) in Purkinje cells. In agreement with this hypothesis, results obtained from the cortical subdivision in seven clusters based on all variables show that the anterior lobe is divided in multiple longitudinal regions (see Fig. 2.14), thus reminding the above-mentioned longitudinal zones and stripes.

2.5 Conclusions and future perspectives

We showed that MRI measures can detect significant differences between cortical regions of the cerebellum suggesting their sensitivity to microstructural features of cerebellar GM. All considerations made to this point are derived from the observation of the maps and from a deep research in literature, but the specificity of MRI measures to cyto-architectural features of cerebellar tissues has never been extensively investigated before. Therefore, given the unique properties of cerebellar tissues in terms of cellular population and density, validation studies should be performed in future, in particular to establish a solid link between diffusion measures and morphological features of cerebellar microstructure. Moreover, diffusion models other than the diffusion tensor and the diffusional kurtosis could be considered. Biophysical models try to model water pools and make assumptions that limit their applicability, but they could provide a more straightforward interpretation of results.

Another relevant factor for the specificity of MRI measures in the cerebellum is spatial resolution. For example, despite precautions taken here, for tissue segmentation and production of flatmaps, small structures like folia ensure a certain degree of partial volume effects. Therefore, high-resolution acquisition are recommended when investigating the cerebellar cortex. However, high resolution would come at the cost of longer acquisition times and, in case of EPI-based sequences (like those commonly adopted for dMRI and fMRI), susceptibility-induced distortions, which can be particularly severe in the cerebellum as shown in Sec. 2.3.1. Therefore, in Chap. 3 the issue of high-resolution and susceptibility-induced artefacts in the case of imaging of small structures of the CNS will be addressed. In particular, the cause of distortions in EPI-based sequences will be examined and the implementation of a reduced-FOV approach to reduce such distortions is presented.

In the current case, another possibility to deal with partial volume effects caused by fissures and folial WM is to exploit two consecutive clusterings: we have shown that with most combinations of measures, one cluster identified fissures and folial WM. This is also true in single-subject maps. Therefore, voxels identified by that cluster could be excluded from analysis.

This work focused on cerebellar cortex. However, literature and preliminary results (here not reported) show that other structures of interest could be the DCN and the cerebellar WM.

As in GM of the cerebellar cortex, regional variability was found also in DCN. Histological studies showed that asymmetries in volume and folding pattern can be found between left and right dentate nuclei (Baizer, 2014) and that cell density differentiates the ventral and the dorsal region of the dentate (Tellmann et al., 2015b). It has been shown that dentate nuclei receive inputs from different regions of the cerebellar cortex: fMRI and tractography have been exploited to identify nuclear subunits involved in motor and cognitive circuits, respectively from the point of view of function and connectivity (Küper et al., 2011, 2012; Steele et al., 2016). All these works recommend further studies to clarify the link between functional, connective and microstructural topography in the cerebellar nuclei.

DCN, and dentate nuclei in particular, can be easily identified in T2w images because of their high iron content, which causes local signal hypo-intensity. However, low signal, low resolution of functional and diffusion sequences and small size (especially of interposed and fastigial nuclei) prevent proper studies of DCN with most MRI scanners ($1.5\,\mathrm{T}$ and $3\,\mathrm{T}$), especially if nuclear subregions are the target of the study. Moreover, iron content generates a strong susceptibility gradient, which can result in distortions when using EPI-based sequences as in almost all fMRI and dMRI protocols. Evidently, from the perspective of topography of subregions of small structures like DCN, distortions would further hinder precise spatial localisation in addition to inter-subject variability. The strategy illustrated in Chap. 3 represents a possible solution also to this issue.

The cerebellar WM is known to be divided in rostro-caudally oriented compartments running perpendicular to lobule main axis. Each WM compartment contains a group of Purkinje cells with specific cortico-nuclear and olivo-cerebellar connectivity, thus representing also a sort of functional compartmentalisation. WM compartments are about $1\,\mathrm{mm}$ wide and they were first identified by J. Voogd in the sixties (Voogd, 2011): using Häggqvist staining (axons are stained blue, while myelin sheath is stained red) he noted that in folial WM regions of fibres with larger calibre were separated by *raphes* of fibres with smaller calibre. He later discovered also systematic difference in the average calibre of fibres across compartments. Thanks to recent technological developments, which resulted in $3\,\mathrm{T}$ scanners with diffusion gradients amplitude up to $300\,\mathrm{mT/m}$, and the development of diffusion models that provide an estimate of the axon diameter it would be exciting to use dMRI to locate compartments in cerebellar WM. This would lead to precise reconstruction of whole individual cerebellar circuits, which, combined with high-resolution fMRI, could help in filling the gap between microscopic physiology and macroscopic brain networks functions.

CHAPTER 3

ZOOM imaging

As shown in the previous chapters, the microstructure of the cerebellum presents unique features that can be investigated using dMRI.

As shown in the previous chapters, dMRI can be exploited to investigate several aspects concerning the cerebellum, including cerebellar connectivity and microstructure. In particular, in Chap. 1, dMRI and probabilistic tractography were exploited to investigate the contribution of cortico-cerebellar connectivity to cognitive processing deficit in MS, while in Chap. 2 dMRI was exploited to assess regional microstructural variations in the cerebellar cortex. Models of the diffusion signal will likely evolve to provide a more and more accurate description of the nervous tissues and this will help to understand the mechanisms of neurological diseases and diagnosis. On the side of image acquisition though, both studies highlighted some weakness. In Chap. 1 higher spatial resolution may have helped to reduce mixing of fibre population in single voxels, thus improving fibre tracking in regions characterised by crossing fibres like the brainstem where the decussation of cerebellar peduncles occurs (see Sec. 1.4). Higher spatial resolution may have also been beneficial in the study described in Chap. 2, where partial volume effects from WM entering folia and CSF surrounding the cerebellum may have affected measurements in cerebellar cortex GM.

Therefore, it is evident that organs like the cerebellum represent a real challenge for current dMRI acquisition strategies: in the specific case of the cerebellum, this is due to the size of its constituents and also to its location.

The cerebellum is located at the base of the skull and its anterior part is close to the oral cavity. The air-tissue interface is responsible for a strong susceptibility gradient that results in severe geometric distortions and signal loss in EPI-based sequences. Unfortunately, most diffusion sequences use an EPI readout and fall into this category. The extent of such distortions is directly proportional to the echo time (TE) and inversely proportional to the bandwidth (BW) in the phase encoding (PE) direction (see Sec. 3.1). Therefore, a reduced FOV in the PE direction could mitigate the distortions by acting on both the TE and the $\mathrm{BW_{PE}}$. This can be particularly useful when investigating small parts of the brain where very high resolution (and therefore a large acquisition matrix) is needed. For example, this is the case of the DCN, which are completely covered by few voxels when using a standard diffusion protocol with $2\,\mathrm{mm}$ isotropic resolution at $3\,\mathrm{T}$. The benefits of high resolution can be much appreciated also when investigating

the cerebellar cortex, where the branches of the *arbor vitae* infiltrating a *folium* are often confounded within GM.

In this chapter, we describe a reduced FOV approach for imaging small structures. In Sec. 3.1, we will analyse the advantages and limitations of reduced FOV techniques with respect to whole-brain imaging. In Sec. 3.2 we will then focus on two particular SE methods called ZOOM and CO-ZOOM that achieve a reduced FOV by applying non-coplanar radio frequency (RF) pulses. We will describe the implementation of such methods on two MRI scanners in Sec. 3.3. Finally, in Sec. 3.4 ZOOM and CO-ZOOM are applied at $3\,\mathrm{T}$ and $7\,\mathrm{T}$ for diffusion study of the cerebellum and at $7\,\mathrm{T}$ for combined dMRI and fMRI study of the pons and the brainstem. The main issues and limitations encountered during sequence testing and application are also discussed.

3.1 Reduced FOV imaging

In a clinical setting, a comprehensive view of the brain is normally required for diagnostic purposes. Also in basic neuroscience research whole brain approaches are usually preferred, for example when investigating structural and functional connections of the brain. Nevertheless, there are a number of circumstances in which the interest is focused only on small parts of the CNS and a reduced FOV is desirable.

The typical example is diffusion imaging of the spinal cord: its cross-sectional dimensions are small and an adequate spatial resolution is needed in order to resolve its internal structure. Imaging of the whole chest with such resolution would lead to unnecessarily long scan times; therefore, for axial acquisitions, the reduced FOV is centred on the spinal cord and the remaining portion of the chest is not acquired, thus reducing the scan time.

This is also valid for diffusion imaging of cerebellar substructures. The DCN are GM structures located in the middle of the cerebellum with dimensions ranging on average from about $3\,\mathrm{mm} \times 3\,\mathrm{mm} \times 2\,\mathrm{mm}$ for the fastigial nuclei to about $13\,\mathrm{mm} \times 19\,\mathrm{mm} \times 14\,\mathrm{mm}$ for the dentate nuclei in humans (Diedrichsen et al., 2011b). The cerebellar cortex is characterised by *folia* where white matter embranchments are surrounded by thin layers of GM. In both cases high spatial resolution (ideally below the millimetre) is fundamental to reduce partial volume effects and for discriminating such small structures (Boillat et al., 2018).

Therefore, the most easily conceivable advantage of reduced FOV imaging is a reduced scan time resulting from the acquisition of only a part of the body or organ when high resolution is needed.

The second important advantage is found when considering that most diffusion sequences are based on fast EPI readouts, which are susceptible to distortions caused by field inhomogeneity. This can be of particular concern when imaging the cerebellum, because of its proximity to the oral cavity. Therein, the air-tissue interface generates a susceptibility difference $\Delta\chi = \chi_2 - \chi_1$ that results in local field inhomogeneity $\Delta B_0 = \Delta\chi\, B_0$, producing severe distortions in the neighbouring regions like the pons (see Fig. 3.1 and 3.2).

EPI sequences are characterised by low BW in the PE direction, with respect to the

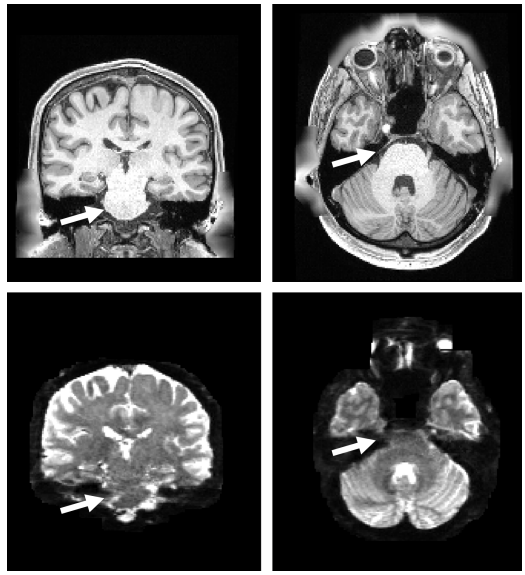

Fig. 3.1: Image distortion along the left - right PE direction caused by susceptibility differences. Top: anatomical reference T1w image. Bottom: single-shot SE-EPI with no diffusion weighting $b = 0\,\mathrm{s/mm^2}$. It is noteworthy that in this image the TOPUP distortion correction method described by Andersson et al. (2003) and implemented in FSL (Smith et al., 2004) has already been applied.

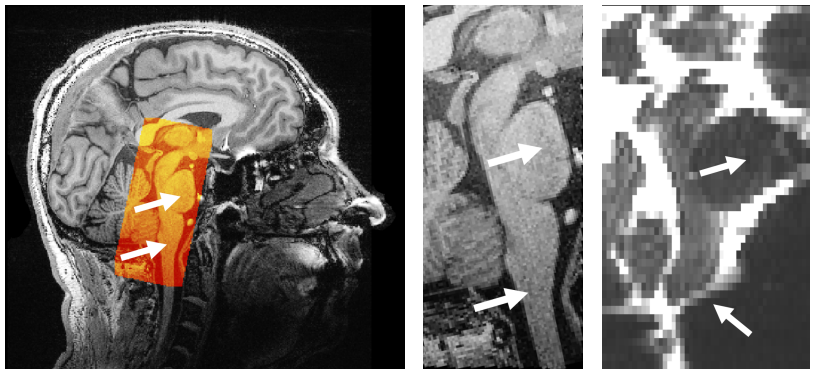

(a) (b) (c)

Fig. 3.2: Image distortion along the anterior - posterior PE direction caused by susceptibility differences. The arrows point at the main observable distortions in the pons and at the basis of the *medulla oblongata*. (a) Anatomical reference T1w image. (b) Snippet of the brainstem obtained from the highlighted region in (a). (c) Snippet of the corresponding single-shot SE-EPI image of the brainstem with no diffusion weighting $b = 0\,\mathrm{s/mm^2}$.

readout (RO) direction:

$$\mathrm{BW}_{\mathrm{RO}} = \frac{1}{T_{\mathrm{RO}}} \tag{3.1}$$

$$\mathrm{BW}_{\mathrm{PE}} = \frac{1}{T_{acq}} \sim \frac{1}{n\,T_{\mathrm{RO}}} = \frac{\mathrm{BW}_{\mathrm{RO}}}{n} \tag{3.2}$$

where T_{RO} is the acquisition time for a single RO line in k-space, T_{acq} is the acquisition time for a whole plane in k-space and n is the number of lines composing that plane. The BW (expressed in Hz/pixel) represents the range of signal frequencies encoded in a pixel at a certain location characterised by a specific Larmor frequency. This means that in the presence of field inhomogeneities, ΔB_0, the corresponding Larmor frequency of the protons is shifted by an amount $\Delta\omega_0 = \gamma \Delta B_0$, where γ is the gyromagnetic ratio of the nucleus under investigation (*e.g.* the proton). If $\Delta\omega_0 > \mathrm{BW}$ the signal is reconstructed in a spatial position different from its true position. The visual result is image distortion. Since $\mathrm{BW}_{\mathrm{PE}} \ll \mathrm{BW}_{\mathrm{RO}}$, this effect is much more evident in the PE direction; the displacement d is proportional to n

$$d \propto \frac{\Delta B_0\,\mathrm{TE}}{\mathrm{BW}_{\mathrm{PE}}} \sim n \frac{\Delta B_0\,\mathrm{TE}}{\mathrm{BW}_{\mathrm{RO}}} \tag{3.3}$$

and it grows with increasing spatial resolution (Port & Pomper, 2000; Fischer & Ladebeck, 1998). In case of field inhomogeneities due to differences in tissues susceptibility $\Delta\chi$:

$$d \propto \frac{\Delta\chi\, B_0\,\mathrm{TE}}{\mathrm{BW}_{\mathrm{PE}}} \sim n \frac{\Delta\chi\, B_0\,\mathrm{TE}}{\mathrm{BW}_{\mathrm{RO}}} \tag{3.4}$$

Therefore, when high resolution is recommended (higher n), a reduced FOV in the PE direction (lower n) can help mitigating distortions by reducing n.

Moreover, a lower number of lines in the PE direction can also imply a shorter TE. In fact, in SE sequences, the TE is defined as the distance between the $\pi/2$ excitation RF pulse and the centre of the echo. Considering that the acquired lines are equally distributed around the centre of the k-space (apart from those cases in which phase partial fourier (PPF) is applied), a lower n means that less lines must be accommodated in the time $\mathrm{TE}/2$ between the π refocusing RF pulse and the centre of the echo, thus allowing a shorter minimum TE and, again, reduced distortions (see Fig. 3.3). A further benefit of a lower n and, therefore, of a shorter TE is a higher signal intensity, counteracting the effect of signal reduction due to enhanced resolution and smaller voxels.

A reduced FOV can not be accomplished simply by reducing the PE size of the acquisition matrix. If the FOV is smaller than the object size, then the Nyquist sampling criterion is not fulfilled, thus giving rise to aliasing artefacts, also called wrap-around or fold-over artefacts (see Fig. 3.4):

$$\frac{1}{\Delta k_{\mathrm{PE}}} \equiv \mathrm{FOV}_{\mathrm{PE}} > A \tag{3.5}$$

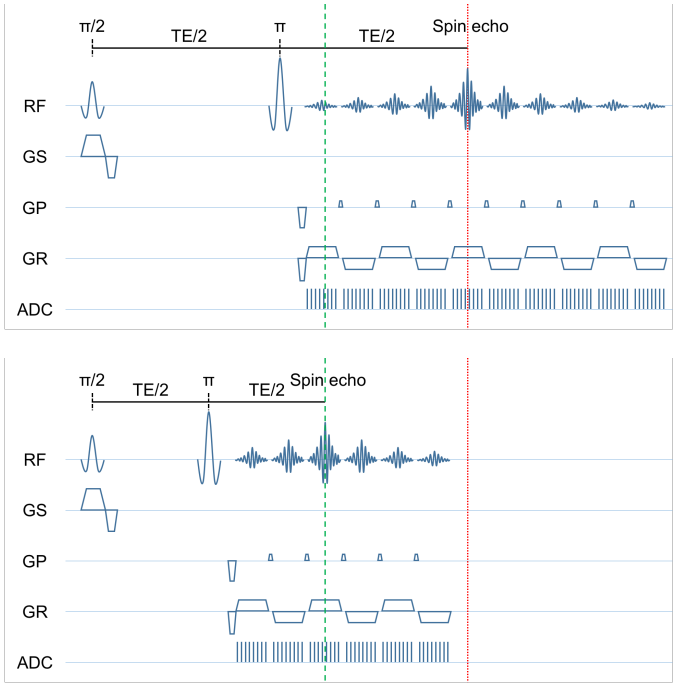

Fig. 3.3: Scheme of a SE sequence showing the effect of a lower number of PE lines on TE. In the top panel more PE lines must be accommodated between the π refocusing RF pulse and the echo peak (red dotted line). In the bottom panel a reduced number of PE lines between the π refocusing RF pulse and the echo peak (green dashed line) reduces the minimum TE.

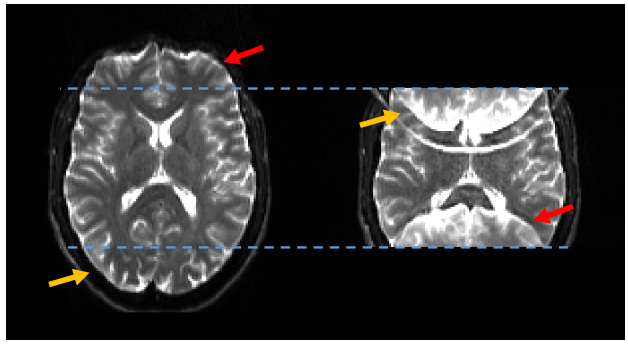

Fig. 3.4: Fold-over artefact due to the reduction of the FOV in the PE direction. In this case, the PE direction is anterior - posterior. The image shown on the right (acquisition matrix: 164×80) was produced by reducing of about the 50% the acquisition FOV shown on the left (acquisition matrix: 164×164) with no use of techniques aiming at the selection of a subregion of the brain. It can be seen that the anterior part of the head is overlaid at the bottom of the image on the right (red arrows) and that, vice versa, the posterior part of the head is overlaid at the top of it (orange arrows). If $\mathrm{FOV}_{\mathrm{PE}}$ is further reduced, multiple overlays may appear.

where Δk_{PE} is the sampling step size in k-space, in this case in the PE direction, $1/\Delta k_{\mathrm{PE}}$ represents the periodicity of the reconstructed spin density and A represents the object size (Brown et al., 2014a).

Aliasing can be avoided by preventing the formation of the signal in regions outside the FOV. This can be achieved using many techniques, which can be grouped in three main categories depending on the physical principle at the base (Wargo et al., 2013):

1. methods that use spatial saturation RF pulses to suppress the signal from neighbouring regions;

2. methods that use 2D spatially selective RF pulses to excite only the imaged volume;

3. methods that use different spatial orientations for the $\pi/2$ and the π RF pulses to refocus only the region that lies at the intersection of the two (inner volume (IV) imaging methods).

In this chapter we will focus mainly on two methods that fall in the last category.

The acquisition of the signal only from a limited region has a major downside: the reduction of the signal intensity. This can be balanced by the shorter TE, as illustrated in Fig. 3.3, by using parallel imaging techniques and PPF to further reduce the number of PE steps and hence the TE, or by resorting to higher B_0 fields. In particular, UHF MRI ($B_0 \geq 7\,\mathrm{T}$) have a great potential for high-resolution imaging in terms of signal, resolution and contrast enhancement. However, such high magnetic fields cause larger susceptibility-induced distortion and bring a number of additional technical issues including B_0 and B_1 inhomogeneities and high power deposition in tissues. Wargo et al. (2013) compared the performance of eight different reduced FOV techniques at 7 T: in particular, they evaluated signal-to-noise ratio (SNR), specific absorption rate (SAR), artefact power and general image quality in a phantom and *in vivo*, for single-slice and

multi-slice modalities. They reported that SAR can be a major limitation for the applicability of reduced FOV techniques from categories 1 and 2, since they need respectively additional RF pulses for spatial saturation or RF pulses with high peak power. SAR also limits the number of slices that can be acquired in a single multi-slice package. Moreover, suppression-based methods are sensitive to B_0 and B_1 field inhomogeneities: B_0 inhomogeneities introduce variations of the Larmor frequency and, consequently, localisation of areas of no interest that need to be suppressed using frequency-selective RF pulses; on the other hand B_1 field inhomogeneities degrade the quality of signal suppression outside the imaged volume, thus potentially causing signal wrap-around in the volume of interest.

Wargo et al. (2013) showed that IV methods provide more precise reduced FOV with sharper profile, much lower SAR and higher single-slice SNR.

These are the main reasons why we decided to focus on techniques from the third category. However, IV methods are not exempt from problems, in particular for multi-slice mode, but these will be specifically addressed in next sections. In particular, ZOOM (Symms, 2000; Wheeler-Kingshott et al., 2002) and CO-ZOOM (Dowell et al., 2009) sequences will be illustrated.

3.2 Theory

Here the physical principles of the ZOOM and CO-ZOOM methods are exposed, addressing also the main limitations of the two. Sec. 3.3 will describe instead the practical implementation of these sequences for dMRI and fMRI applications at $3\,\mathrm{T}$ and $7\,\mathrm{T}$.

3.2.1 ZOOM

IV MRI was originally proposed by Feinberg et al. (1985) to reduce the scan time and to eliminate artefacts originating from tissues adjacent to the imaged region. The π RF pulse is tilted with respect to the $\pi/2$ excitation RF pulse by 90° and only the spins experiencing both pulses are refocused (see Fig. 3.5). Therefore, at the time of measurement, the signal originates only from the region at the intersection of the pulses. The first implementation of this technique did not contemplate an EPI readout. The main limitation of this method is the infeasibility of multi-slice mode because of severe signal loss in the neighbouring slices, whose magnetization is inverted by the tilted refocusing pulse.

Wheeler-Kingshott et al. (2002) proposed a solution to bypass this problem: the IV is selected by tilting the refocusing pulse by an angle θ smaller than 90° (see Fig. 3.6). This is achieved by applying a magnetic field gradient along the PE direction at the same time of the RF pulse and of the slice selective gradient. The amplitude of the PE gradient determines the angle θ, which in turn determines the number of slices N whose magnetization is (only partially) inverted. Therefore, it is not possible to acquire contiguous slices in a linear fashion, but a slice gap must be left between two slices which are chronologically consecutive: after the acquisition of the first slice of the stack, the next one to be acquired is the $(N+1)^{th}$, thus allowing an interleaved multi-slice mode (see Fig. 3.7).

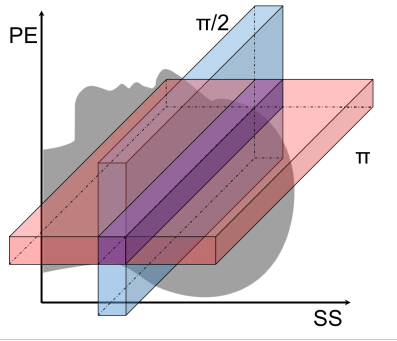

Fig. 3.5: Schematic view of IV MRI as proposed by Feinberg et al. (1985). A slice selective $\pi/2$ RF pulse (blue) is followed by a refocusing π pulse (red). Only the spins at the intersection of the pulses are refocused and generate the MR signal (purple).

The result of the selection is a region with the shape of a parallelogram (purple region, Fig. 3.6d). If the FOV is smaller than the PE size of the parallelogram l_{PE} wrap-around artefacts must be expected. However, a minimum $\mathrm{FOV}_{min} < l_{\mathrm{PE}}$ can be defined if the volume of interest is limited to the rectangular part of the excited region (*i.e.* the IV). The triangular regions are called transition bands (TBs) and the minimum FOV is

$$\mathrm{FOV}_{min} = \mathrm{FOV}_{iv} + l_{TB} \tag{3.6}$$

where FOV_{iv} is the desired IV (rectangular region) and l_{TB} represents the PE size of one triangle. If FOV_{min} is centred around the IV, wrap-around artefacts will be present but will not affect the volume of interest.

From these considerations, the two main limitations of this method can be evinced:

1. The oblique RF pulse acts also on the magnetization of a portion of the N adjacent slices. Hence the necessity to leave an N-sized slice gap. If contiguous slices are required, the whole stack of slices can be divided in $N+1$ interleaved sets of slices, which will be acquired one after the other. If the time needed to acquire a whole slice set is short to fully restore the magnetization of the first slice of the next set, then cross-talk arises, *i.e.* signal loss and inhomogeneity across the slice. Therefore, the next slice set should be acquired after waiting a whole repetition time (TR) set long enough to allow a full recovery of the magnetization (*e.g.* $\mathrm{TR} > 5\,\mathrm{T}_1$). This means that, in case of contiguous slices, the acquisition time for the whole volume of interest will be $(N+1) \times \mathrm{TR}$, where TR in this case indicates the ideal TR that would be set for the specific acquisition (*e.g.* $\sim 3\,\mathrm{s}$ for a standard fMRI experiment).

2. The triangular TBs are part of the selected regions. Therefore, in order to avoid wrap-around artefacts in the IV an $\mathrm{FOV}_{min} > \mathrm{FOV}_{iv}$ must be acquired (over-sampling in the PE direction by at least l_{TB}), thus reducing the impact of ZOOM on susceptibility-induced distortions. Paradoxically, if the gap was only one slice thick $\mathrm{FOV}_{min} = 2\,\mathrm{FOV}_{iv}$ and if the volume of interest was as big as half of the brain, FOV_{min} would have the same size of the whole brain. In order to address

this problem, Wilm et al. (2009) proposed the use of suppression bands to eliminate the signal originating from the TBs. This solution would reduce the distortions and shorten TE, but at UHF would encounter SAR limits.

3.2.2 CO-ZOOM

Another solution for multi-slice IV MRI was proposed by Dowell et al. (2009). This method is based on a dual (or twice-refocused) SE approach commonly adopted for bipolar diffusion sequences: a pair of π refocusing RF pulses are orthogonally applied with respect to the excitation pulse as for the original IV method. The first π pulse refocuses the magnetization of the spins included in the region of intersection of the two pulses, but it also inverts the magnetization of the spins of all the other slices. The second π pulse refocuses again the magnetization of the selected volume and it restores the magnetization of adjacent slices towards the B_0 direction (see Fig. 3.8).

However, because of longitudinal relaxation, part of the inverted magnetization is recovered in the time between the two π RF pulses. This means that when the second slice is excited, if the magnetization is not fully recovered along the B_0 field direction, the magnetization brought into the transverse plane by the $\pi/2$ pulse will be smaller than the one of the first slice. The same concept holds for the following slices with respect to the previous ones. This implies that slices imaged earlier will provide a higher signal with respect to the subsequent ones, but a steady state is established after a number of repetitions. Therefore, in order to achieve signal homogeneity through slices, dummy scans should be added at the beginning of the sequence.

Finally, the authors showed that the signal intensity at the steady state depends on the time $\mathrm{TE}/2$ between the two refocusing pulses and on the time TR/n where n is the total number of slices, or, equivalently, the number of times the π pulses pair is repeated. The first dependency is explained by the amount of recovered magnetization between the two pulses: ideally, if the process of magnetization inversion was instantaneous and if the second pulse was applied immediately after the first one, the whole magnetization would be recovered along the B_0 direction and there would be no signal loss. Moreover, a shorter $\mathrm{TE}/2$ reduces transverse relaxation effects. The second dependency was implicitly illustrated above: even if the magnetization is not fully recovered after the second refocusing pulse, longitudinal relaxation mechanisms take place in the time TR/n between two pairs of π RF pulses. The longer TR/n is, the more complete the magnetization recovery will be. For sufficiently long TR/n there is no signal loss.

Therefore the main limitation of this method is the signal intensity, which is reduced with increasing number of slices and for short TR. Signal intensity is further reduced by long TEs, which could be necessary to accommodate gradients for strong diffusion weighting with high b-values. Moreover, this method is based on dual SE that lenghtens the minimum TE and provides lower signal with respect to SE sequences with only one refocusing pulse.

On the other hand, the CO-ZOOM method overcomes the problems that affect the ZOOM: no slice gap is required, thus making the acquisition of contiguous slices possible and allowing the acquisition of all slices within one TR. Since the angle between the

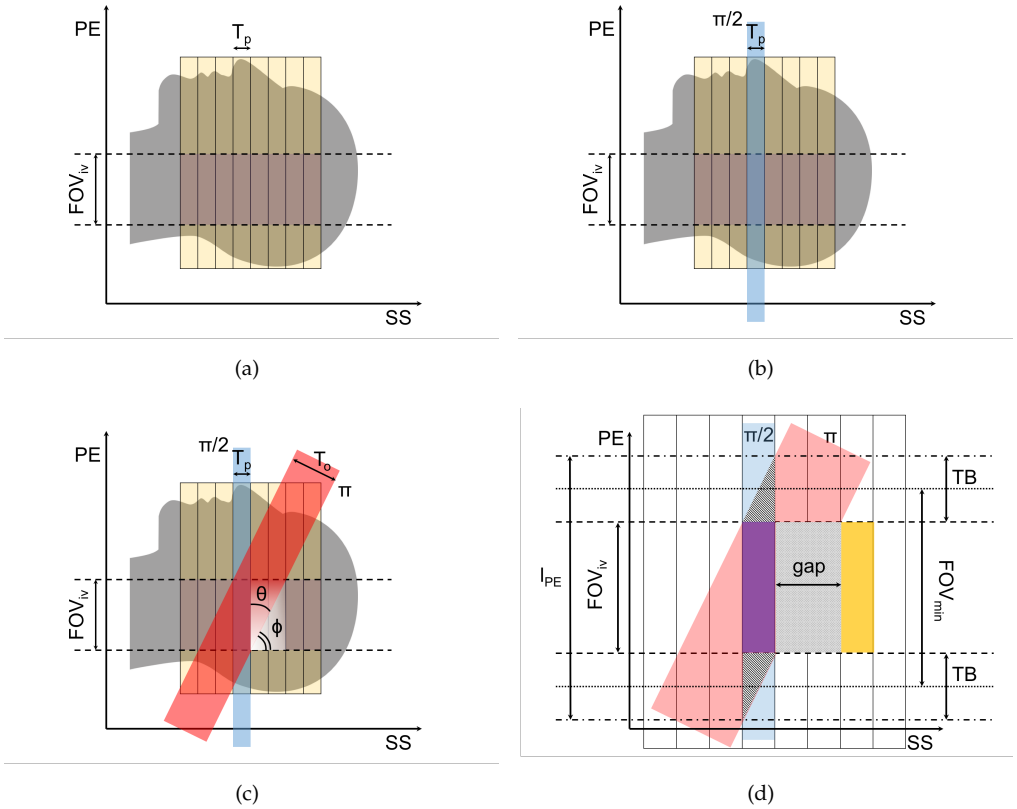

Fig. 3.6: Schematic view of ZOOM SE imaging. The size of the desired reduced FOV is FOV_{iv} (a). First, the slice selective $\pi/2$ excitation pulse is applied (blue) and its thickness T_p is the slice thickness set into the protocol (b). Then, the refocusing pulse with thickness T_o (see Eq. 3.9) is applied (red) tilted by the angle θ with respect to the previous excitation pulse (c). The region selected by the two RF pulses is the parallelogram made by the purple rectangle (the desired FOV) and the two dashed triangular regions, *i.e.* the transition bands (d). Here are displayed also the PE size of the parallelogram l_{PE}, the minimum FOV FOV_{min} (see Eq. 3.8), the transition bands TB and the minimum gap required to avoid cross-talk. Here, apart from the selected slice, $N = 2$ slices to its right are affected by the oblique pulse. Therefore, the following slice to be acquired is displayed in yellow.

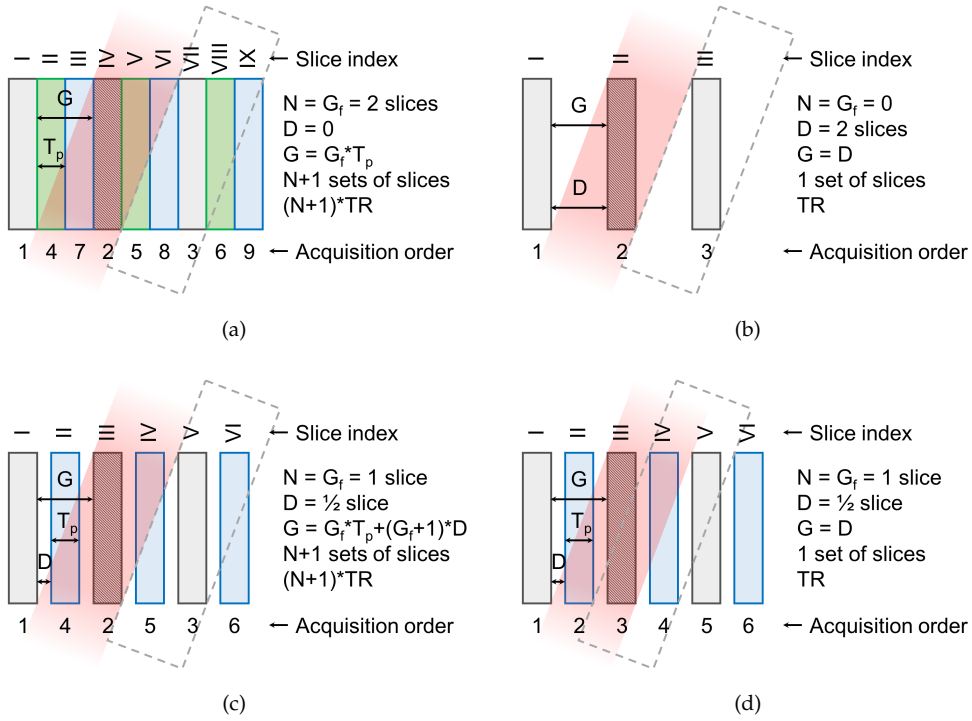

Fig. 3.7: Schemes for ZOOM multi-slice acquisition modes. The slice index expressed in Roman numerals represents the physical slice order that will be reconstructed (see Sec. 3.3.1). The order of acquisition is indicated in Arabic numerals. The red regions represent the oblique pulse that is applied to select the current slice (greyed). The dashed rectangles represent the oblique pulse that will be applied to select the next slice. Physically contiguous slices are acquired only in scheme (a), where the effective gap G between two consecutively acquired slices is a multiple of T_p and is given by the gap factor G_f only. The scheme illustrated in (b) is for non contiguous slices: a gap between them already exists and it is exploited to accommodate the tilted RF pulse. The scheme illustrated in (c) is a combination of (a) and (b). These three schemes are allowed in the modified UI (see Sec. 3.3.1 and Fig. 3.9). (a), (b) and (c) show three possibilities of dedicated slice order, which prevent the oblique pulse from affecting the next acquired slice. The scheme illustrated in (d) represents a sequential acquisition where each slice is affected by the oblique pulse that selects the previous slice. This last scheme was adopted by Wargo et al. (2013) to reduce the total scan time at the expense of signal intensity.

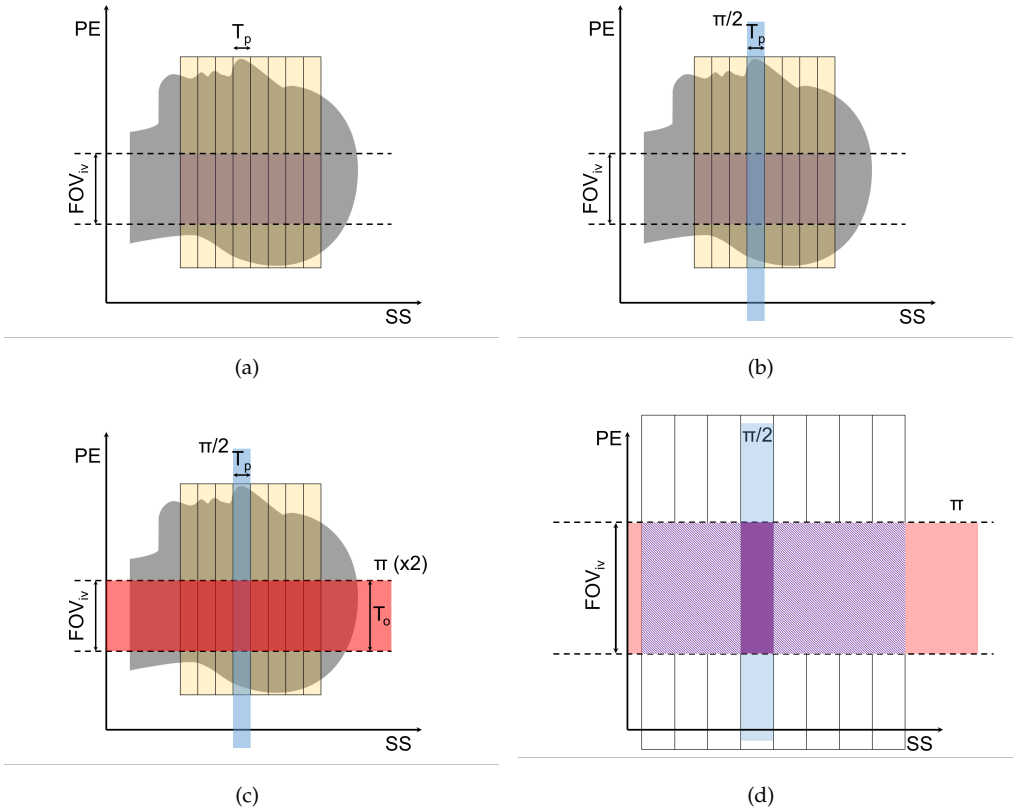

Fig. 3.8: Schematic view of CO-ZOOM dual SE imaging. The first two steps (a and b) are the same as for ZOOM imaging (see Fig. 3.6): the size of the desired reduced FOV is FOV_{iv} (a). The slice selective $\pi/2$ excitation pulse is applied (blue) and its thickness T_p is the slice thickness set into the protocol (b). Then, the two refocusing pulses with thickness FOV_{iv} are applied (red) orthogonally with respect to the previous excitation pulse (c). The region selected by the three RF pulses is the purple rectangle (d). The whole slice stack if affected by the pair of π pulses (light purple).

excitation and the refocusing pulses is equal to $90°$ the acquired FOV corresponds to the desired FOV_{iv}.

3.3 Implementation

This section describes the practical implementation of ZOOM and CO-ZOOM sequences for a $3\,\mathrm{T}$ Prisma and $7\,\mathrm{T}$ Magnetom Siemens scanners (Siemens Healthineers, Erlangen, Germany). The sequences were developed within the coding environment called IDEA (Integrated Development Environment for Applications) provided by Siemens. The programming language is C++ (object-oriented) and the starting point for this work is the 2D-EPI Siemens product sequence for dMRI applications.

3.3.1 ZOOM

ZOOM achieves a reduced FOV in the PE direction by tilting one of the two RF pulses that make the SE. Originally, the π refocusing pulse was applied at an angle φ with respect to the slice selection (SS) direction (Symms, 2000; Wheeler-Kingshott et al., 2002). Here, conversely, the orientation of the excitation pulse is changed and the refocusing pulse is slice selective. This configuration allows a faster recovery of the magnetization in neighbouring slices, where the magnetization relaxes starting from the transverse xy plane and not from the $-\hat{z}$ axis. This can reduce signal loss in neighbouring slices and it can be particularly relevant, for example:

- if the slice profile corresponding to the oblique pulse is not sufficiently sharp (see Sec. 3.3.3);
- if the acquisition contemplates a slice gap smaller than required and if a dedicated interleaved slice order of acquisition is not applied (see Fig. 3.7d).

These considerations are also confirmed by Wargo et al. (2013), who inverted the orientations of RF pulses in the original IV sequence proposed by (Feinberg et al., 1985). They showed that if the $\pi/2$ pulse excites the whole stack of slices and the π pulse is slice selective and refocuses only the imaged slice, the signal loss in the following slices is reduced.

All parameters needed to configure the ZOOM geometry can be obtained by fixing two of them. Since this method is not contemplated by the original 2D-EPI, the UI was modified to allow the user to set the additional parameters required (see Fig. 3.9). In the "Special"card (*i.e.* an additional window that can be added to the UI to control parameters required by new applications) it is now possible to choose whether to acquire a reduced FOV and, if yes, the method (*i.e.* ZOOM or CO-ZOOM). For ZOOM imaging the user can now set FOV_{iv} (*i.e.* the PE size of the IV) expressed in millimetres and the gap factor G_f expressed in number of slices (*e.g.* if the slice thickness is $2\,\mathrm{mm}$ and the Zoom Gap Factor is 3, the gap (edge-to-edge) between two consecutively acquired slices is $6\,\mathrm{mm}$ wide and it will accommodate three slices). Further parameters required from the sequence protocol to set the geometry are the protocol "Slice thickness" T_p and the

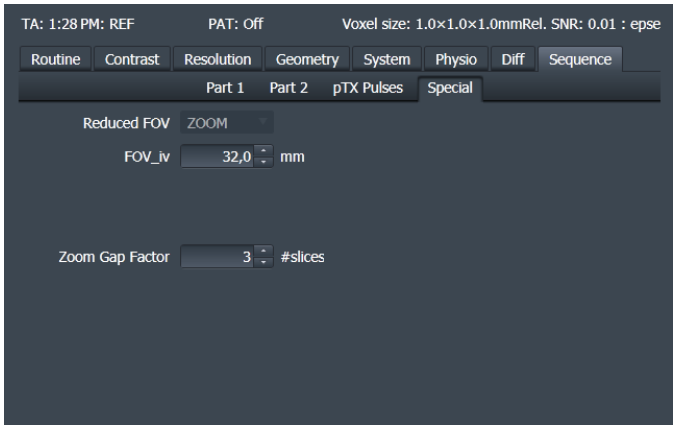

(a)

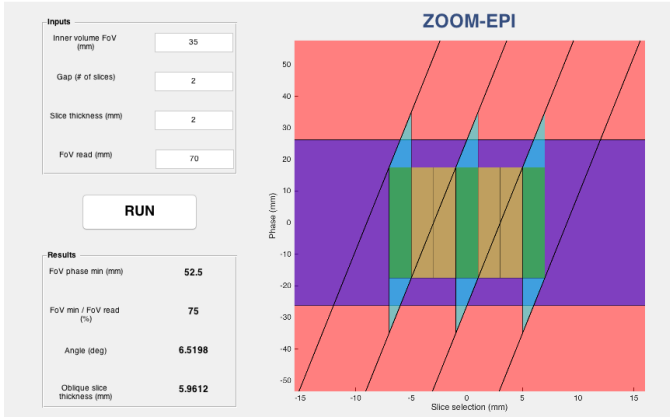

(b)

Fig. 3.9: (a) Screenshot of the scanner UI modified to allow the user to set ZOOM parameters. The FOV_{iv} and the gap factor G_f were chosen because, to our judgement, they are the ones that provide the user with the most intuitive representation of the sequence. (b) Screenshot of the tool developed using MATLAB that provides a pictorial view of the ZOOM sequence and the correct parameters to set in the scanner UI given the FOV_{iv}, the G_f and the protocol slice thickness T_p.

"Distance factor" D, which are already present in the UI. It follows that:

$$\theta = \arctan\left(\frac{G}{\mathrm{FOV}_{iv}}\right) \tag{3.7}$$

$$\mathrm{FOV}_{min} = \mathrm{FOV}_{iv} + \frac{T_p}{\tan\theta} = \mathrm{FOV}_{iv}\left(1 + \frac{T_p}{G}\right) \tag{3.8}$$

$$T_o = T_p \cos\theta + \mathrm{FOV}_{iv} \sin\theta \tag{3.9}$$

where T_o is the thickness of the oblique slice and the gap expressed in millimetres is G, which takes into account also D to allow different possible configurations of slices (see

Fig. 3.10: Coordinate systems in an MRI scanner. Left: the (x, y, z) device coordinate system (DCS). Right: the (PE, RO, SS) logical coordinate system (LCS). The DCS is fixed, while the LCS depends on subject orientation and imaging parameters. The LCS shown here is for the specific case: "head-first", "supine" with axial acquisition and A→P PE direction.

Fig. 3.7):

$$G = G_f T_p + (G_f + 1)D \tag{3.10}$$

These functions are gathered in a class called `zoom`, which includes all the variables required for FOV reduction. An object of this class is created and passed to sequence functions where required to change the sequence blocks accordingly, with blocks meaning here the basic constituents of the sequence like the excitation block, the diffusion encoding block and the readout block.

Within the sequence code, the physical stack of slices is represented by an array of `slice` objects A_S. The order of `slices` within A_S represents the chronological order of acquisition. Moreover, each `slice` of A_S is characterized by the slice index, the slice shift and the rotation matrix. The slice index refers to the physical position of the slice: if an object `slice` is the second element of A_S, but its slice index is 3 (numbering starts from 0), it means that the fourth physical slice will be the second to be acquired. Therefore, the slice index is linked to the physical position of the slice and to the slice shift, which is the distance between the isocenter of the scanner and the plane passing through the centre of the slice (*i.e.* the shift in the SS direction; see Fig. 3.12). The slice shift determines the central frequency of the RF pulse. Finally, the rotation matrix stores information about the slice orientation.

In an MRI scanner, different coordinate systems can be defined (see Fig. 3.10). In particular:

- the device coordinate system (DCS) (x, y, z) is related to the physical gradients (*i.e.* the gradient coils) of the scanner (see Fig. 3.10);
- the logical coordinate system (LCS) (PE,RO,SS) is related to imaging parameters and it is defined by

$$\vec{G}_\mathrm{PE} \times \vec{G}_\mathrm{RO} = \vec{G}_\mathrm{SS} \tag{3.11}$$

The relation between these two coordinate systems depends on the position of the subject (*e.g.* head-first, supine), on the type of acquisition (axial, sagittal, coronal and intermediate slice orientations) and on the PE direction, which determines the in-plane

rotation of the slice (typically anterior - posterior, right - left or feet - head, but also intermediate angles are allowed).

Parameters set by the user during the protocol planning are in LCS, but these are then transformed to DCS, to which the gradient coils refer. This transformation is achieved by applying the above-mentioned rotation matrix **R** stored in each `slice` object

$$\mathbf{R} = \begin{pmatrix} r_{00} & r_{01} & r_{02} \\ r_{10} & r_{11} & r_{12} \\ r_{20} & r_{21} & r_{22} \end{pmatrix} \tag{3.12}$$

that links the two coordinate systems in the following way

$$\begin{pmatrix} G_x \\ G_y \\ G_z \end{pmatrix} = \mathbf{R} \times \begin{pmatrix} G_{\mathrm{PE}} \\ G_{\mathrm{RO}} \\ G_{\mathrm{SS}} \end{pmatrix} \tag{3.13}$$

For example, if the positioning of the patient is head-first, supine and the acquisition planning is exactly transversal (*i.e.* axial) and the PE direction is anterior - posterior (that means from the anterior part of the head to its posterior part and is also denoted A→P), **R** is (see Fig. 3.10):

$$\mathbf{R} = \begin{pmatrix} 0 & -1 & 0 \\ -1 & 0 & 0 \\ 0 & 0 & -1 \end{pmatrix} \tag{3.14}$$

A change of the slice orientation is achieved by changing the direction of application of the slice selective magnetic field gradient. For ZOOM imaging only one of the two slice selective gradients (the one corresponding to the excitation pulse or the one corresponding to the refocusing pulse) is changed to create the planes intersection that identifies the IV. Therefore, for ZOOM imaging, the normal vector that identifies the slice orientation must be tilted from the SS direction towards the PE direction by an angle θ. In LCS this corresponds to a rotation around the RO coordinate (that is the second coordinate in LCS). This last transformation relates LCS to what we could call the zoom coordinate system (ZCS)

$$\begin{pmatrix} G_{\mathrm{PE}} \\ G_{\mathrm{RO}} \\ G_{\mathrm{SS}} \end{pmatrix} = \mathbf{R}_{\mathrm{Z}} \times \begin{pmatrix} G_{\mathrm{PE,Z}} \\ G_{\mathrm{RO,Z}} \\ G_{\mathrm{SS,Z}} \end{pmatrix} \tag{3.15}$$

where the subscript Z refers to ZOOM and $\mathbf{R}_{\mathrm{Z}}$ is

$$\mathbf{R}_{\mathrm{Z}} = \begin{pmatrix} \cos\theta & 0 & -\sin\theta \\ 0 & 1 & 0 \\ \sin\theta & 0 & \cos\theta \end{pmatrix} \tag{3.16}$$

Therefore, $\mathbf{R}_{\mathrm{Z}}$ introduces a PE component in LCS and the direction of the resulting gradient is rotated (see Fig. 3.11).

It follows that the rotation matrix $\mathbf{R}'$ such that

$$\begin{pmatrix} G_x \\ G_y \\ G_z \end{pmatrix} = \mathbf{R} \times \mathbf{R}_{\mathrm{Z}} \times \begin{pmatrix} G_{\mathrm{PE,Z}} \\ G_{\mathrm{RO,Z}} \\ G_{\mathrm{SS,Z}} \end{pmatrix} = \mathbf{R}' \times \begin{pmatrix} G_{\mathrm{PE,Z}} \\ G_{\mathrm{RO,Z}} \\ G_{\mathrm{SS,Z}} \end{pmatrix} \tag{3.17}$$

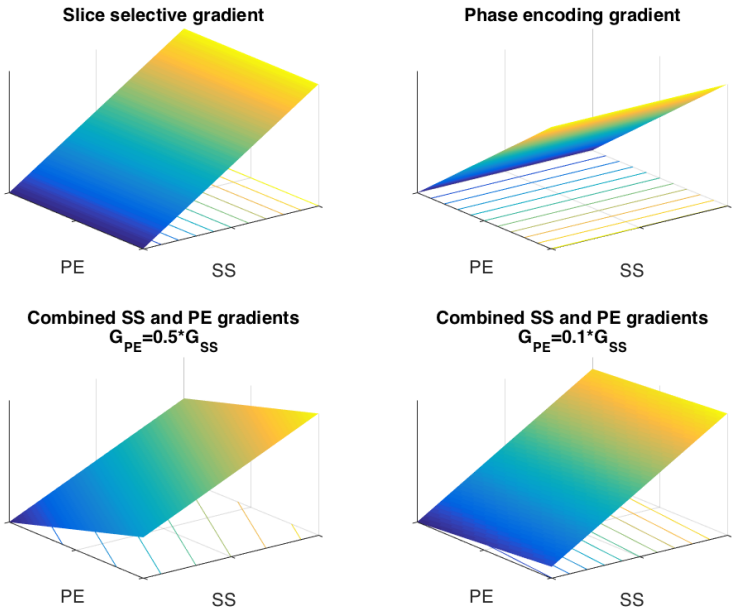

Fig. 3.11: Simultaneous application of magnetic gradients along the SS and the PE directions. Different relative weights for the linear combination of the two gradients rotate the resulting gradient by different angles. The resulting direction is perpendicular to the level curves displayed on the floor of each plot.

$$\mathbf{R}' = \mathbf{R} \times \mathbf{R}_{\mathrm{Z}} = \begin{pmatrix} r_{00}\cos\theta + r_{02}\sin\theta & r_{01} & -r_{00}\sin\theta + r_{02}\cos\theta \\ r_{10}\cos\theta + r_{12}\sin\theta & r_{11} & -r_{10}\sin\theta + r_{12}\cos\theta \\ r_{20}\cos\theta + r_{22}\sin\theta & r_{21} & -r_{20}\sin\theta + r_{22}\cos\theta \end{pmatrix} \tag{3.18}$$

is the rotation matrix that will be stored in the `slice` object that corresponds to the physical oblique slice. Therefore, when tilting a slice, it is not necessary to manually add a magnetic gradient in the PE direction, but it is sufficient to compute the angle and the rotation matrix and the sequence code will take care of applying the correct combination of (G_x, G_y, G_z) gradients.

Now it is also possible to compute the slice shift of the oblique slice. As mentioned above, the slice shift determines the central frequency of the RF pulse and it is stored in LCS coordinates in the `slice` object. In order to calculate the RF pulse central frequency, usually the rotation matrix $\mathbf{R}$ is applied to the vector that locates the centre of the slice in LCS. In the case of the oblique slice, the stored rotation matrix is $\mathbf{R}'$ and, therefore, the slice centre must be coherently expressed in ZCS coordinates:

$$\begin{pmatrix} C_{\mathrm{PE,Z}} \\ C_{\mathrm{RO,Z}} \\ C_{\mathrm{SS,Z}} \end{pmatrix} = \mathbf{R}_Z^{-1} \times \begin{pmatrix} C_{\mathrm{PE}} \\ C_{\mathrm{RO}} \\ C_{\mathrm{SS}} \end{pmatrix} = \begin{pmatrix} \cos\theta & 0 & \sin\theta \\ 0 & 1 & 0 \\ -\sin\theta & 0 & \cos\theta \end{pmatrix} \times \begin{pmatrix} C_{\mathrm{PE}} \\ C_{\mathrm{RO}} \\ C_{\mathrm{SS}} \end{pmatrix} \tag{3.19}$$

where C_{PE} and C_{RO} represent the slice off-centre in the PE and RO directions respectively and C_{SS} represents the slice shift. This quantities are analogously defined in ZCS and

$$C_{\mathrm{SS,Z}} = -C_{\mathrm{PE}}\sin\theta + C_{\mathrm{SS}}\cos\theta \tag{3.20}$$

is the slice shift that must be stored in the `slice` object corresponding to the oblique slice (see Fig. 3.12). The remaining two coordinates of the slice centre expressed in ZCS are discarded and the reason is discussed below.

Thus, a rather simple way to implement the ZOOM sequence is the following:

1. When the original `slice` array A_{S} is prepared, the slices are stored in A_{S} according to their acquisition order, which is determined by the gap G (see Eq. 3.10). To this end, a function has been written to implement the correct ZOOM-dedicated slice order starting from the standard "Ascending" order provided by Siemens (the slice order "Ascending" must be explicitly set by the user in the UI during the protocol planning). Within this step, the geometric parameters of each `slice` are set, including the rotation matrix $\mathbf{R}$ and the position of the slice centre in LCS coordinates.

2. After the acquisition order and the geometric parameters have been set, an array $A_{\mathrm{S,Z}}$ copy of A_{S} is created.

3. The rotation matrix and the slice shift of each `slice` in $A_{\mathrm{S,Z}}$ are changed according to Eqs. 3.7, 3.10, 3.18 and 3.19, thus introducing the ZCS.

4. When the methods in charge of running the sequence blocks are called, the proper `slice` array is passed. In the case of a tilted $\pi/2$ excitation pulse, $A_{\mathrm{S,Z}}$ is provided

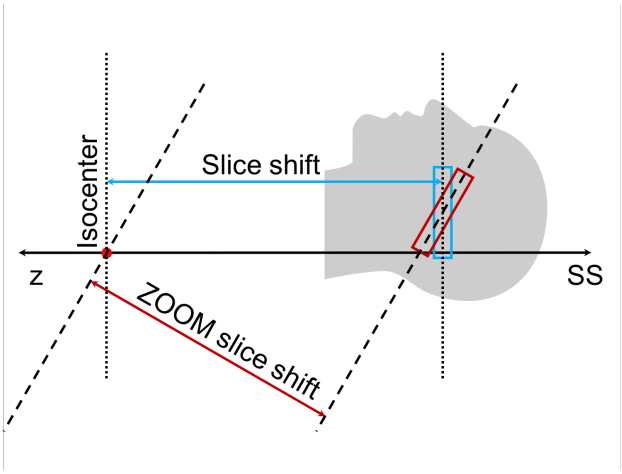

Fig. 3.12: Visual representation of the slice shift. The slice shift is the distance between the isocenter of the scanner and the centre of the slice. It determines the central frequency of the corresponding RF pulse. If the slice is tilted as with the ZOOM method, its slice shift must be set according to the new rotation matrix $\mathbf{R}'$ (see Eq. 3.20).

to the method that rules the excitation block and A_{S} is passed to the method that rules the refocusing pulse. To implement the first version of ZOOM as proposed by Symms (2000) and Wheeler-Kingshott et al. (2002), the excitation block should be provided with A_{S}, while $A_{\mathrm{S,Z}}$ should be passed to the methods ruling the refocusing block. The readout block is always provided with A_{S}.

5. The block corresponding to the tilted pulse is also provided with the `zoom` object: it contains information about the thickness of the oblique slice (see Eq. 3.9). This is used to set accordingly the factors of the excitation block like the pulse duration, the amplitude of the slice selective gradient and of the B_1 field.

6. Because of ZOOM reordering, the header file that is filled with measurement data throughout the acquisition (and that maps such data with indexes for subsequent image reconstruction) must be informed of the correct slice number, which is different from the one expected with the "Ascending" slice order. To this end, the slice index is provided.

It should now be clear why $C_{\mathrm{PE,Z}}$ and $C_{\mathrm{RO,Z}}$ are discarded. The PE and RO off-centre coordinates of the slice centre are only used during image reconstruction to set the proper FOV. By providing the readout block with A_{S}, the reconstructed image will be correctly centred on the slice with the PE and RO FOV set by the user in the UI. Therefore, the user must provide the FOV in the PE direction in the UI with the correct FOV_{min} (see Eq. 3.8). To help with the computation of this quantity (that in Siemens UI is expressed in terms of percentage of the FOV in the RO direction) and to provide a pictorial representation of the ZOOM mechanism, a simple tool was developed in MAT-

LAB[1] (see Fig. 3.9b). This returns also numerical information about the angle θ and the thickness T_o of the oblique slice.

3.3.2 CO-ZOOM

As explained above, CO-ZOOM selects a reduced FOV in the PE direction again by applying non-coplanar slice selective RF pulses. Here, the two refocusing pulses are applied orthogonally to the PE direction and their thickness is the $\mathrm{FOV_{PE}}$.

The practical implementation of CO-ZOOM is not much different from the ZOOM one. Here, though, only one parameter is required to be entered by the user to set the geometry. In fact, the tilt angle is fixed at $\theta = 90°$, no gap is needed and all slices can be acquired according to any of the default ordering methods provided by Siemens ("Ascending","Descending" or "Interleaved"). Therefore, only the size of the reduced FOV in the PE direction must be set. It is possible to create a dedicated field in the UI, but since $\mathrm{FOV}_{iv} = \mathrm{FOV}_{min}$ it is easier to set it directly by adjusting the default $\mathrm{FOV_{PE}}$ field in the UI. Finally, from Eq. 3.9 $T_o = \mathrm{FOV}_{iv}$.

The `zoom` class mentioned above includes variables and methods also for CO-ZOOM imaging. The concepts explained above for `slice` objects are still valid. In this case it is always

$$\mathbf{R}_{\mathrm{Z}} = \begin{pmatrix} 0 & 0 & -1 \\ 0 & 1 & 0 \\ 1 & 0 & 0 \end{pmatrix} \qquad \mathbf{R}' = \begin{pmatrix} r_{02} & r_{01} & -r_{00} \\ r_{12} & r_{11} & -r_{10} \\ r_{22} & r_{21} & -r_{20} \end{pmatrix} \tag{3.21}$$

$$\begin{pmatrix} G_{\mathrm{PE,Z}} \\ G_{\mathrm{RO,Z}} \\ G_{\mathrm{SS,Z}} \end{pmatrix} = \mathbf{R}_{\mathrm{Z}}^{-1} \times \begin{pmatrix} G_{\mathrm{PE}} \\ G_{\mathrm{RO}} \\ G_{\mathrm{SS}} \end{pmatrix} = \begin{pmatrix} 0 & 0 & 1 \\ 0 & 1 & 0 \\ -1 & 0 & 0 \end{pmatrix} \times \begin{pmatrix} G_{\mathrm{PE}} \\ G_{\mathrm{RO}} \\ G_{\mathrm{SS}} \end{pmatrix} = \begin{pmatrix} G_{\mathrm{SS}} \\ G_{\mathrm{RO}} \\ -G_{\mathrm{PE}} \end{pmatrix} \tag{3.22}$$

and the resulting slice shift in ZCS coordinates is the same for each slice

$$C_{\mathrm{SS,Z}} = -C_{\mathrm{PE}} \tag{3.23}$$

Therefore, CO-ZOOM is implemented in the following way:

1. The `slice` array $A_{\mathtt{s}}$ is prepared and its elements are arranged according to one of the default ordering methods that is chosen by the user in the UI. The rotation matrix $\mathbf{R}$ and the position of the slice centre are computed for each `slice` of $A_{\mathtt{s}}$.

2. After the acquisition order and the geometric parameters have been set, an array $A_{\mathrm{s,Z}}$ copy of $A_{\mathtt{s}}$ is created.

3. The rotation matrix and the slice shift for each `slice` in $A_{\mathrm{s,Z}}$ are changed according to Eqs. 3.21, 3.22 and 3.23.

4. When the methods (C++ class functions) in charge of running the sequence blocks are called, the proper `slice` array is provided. In this case, π refocusing RF pulses

[1] The MathWorks, Inc., Natick, MA. `https://www.mathworks.com`

are tilted with respect to the original stack of slices. Therefore, $A_{\mathrm{S,Z}}$ is provided to the method that rules the refocusing block and A_{S} is passed to the method that rules the excitation pulse. Again, the readout block is always provided with A_{S}.

5. The `zoom` object is provided to the block corresponding to the tilted pulse to pass information about the thickness of the oblique slice: FOV_{iv} for CO-ZOOM.

6. Since CO-ZOOM adopts the default slice orderings, the header file that collects the measurement data is already informed about the correct acquisition order of the slices and there is no need to provide it with the slice index.

3.3.3 Problems and artefacts addressed

ZOOM and CO-ZOOM were tested at $3\,\mathrm{T}$ and $7\,\mathrm{T}$ on both phantoms and healthy volunteers. A cylindrical phantom with no internal structure was first used to have a visual confirmation of the $\mathrm{FOV}_{\mathrm{PE}}$ reduction. The main issues encountered were related to the slice profile.

Siemens SE EPI sequence for diffusion applications usually adopts the pulses reported in Fig. 3.14a and b for excitation and refocusing respectively. These pulses are suggested for a slice thickness ranging from $2.4\,\mathrm{mm}$ to $20.0\,\mathrm{mm}$. When certain conditions are met the pulses displayed in Fig. 3.14c and d are used instead. These pulses have a higher time-bandwidth product (TBW) (*i.e.* the number of zero-crossings of the pulse in the time domain) and thus, by increasing the SS gradient and the B_1 field amplitude accordingly, they provide a slice with the same thickness, but with an improved profile. These pulses are suggested for a slice thickness ranging from $1.0\,\mathrm{mm}$ to $500.0\,\mathrm{mm}$.

Phantom The quality of the slice profile was tested against different values of FOV_{iv}. An example of a test conducted at $3\,\mathrm{T}$ is shown in Fig. 3.15. In the reported case, the full $\mathrm{FOV}_{\mathrm{PE}}$ was maintained for data acquisition and CO-ZOOM was used to select the desired region. Therefore, the displayed images are the result of the double refocusing pulses. The full FOV acquisition shows a higher signal intensity in the most external regions of the phantom due to their proximity to the coil elements. This feature is maintained also in reduced FOV images. However, the homogeneous content of the phantom highlights signal inhomogeneity across the slice width. As can be noticed comparing the profile of the measured signal with the shape of the signal in the frequency domain in Fig. 3.14d that was used in this test, signal ripples due to the pulse shape appear in the selected region. The ripples are more visible in the outer region of the phantom where the signal is higher (orange lines with respect to blue lines) and they become more evident with increasing width of the FOV_{iv} (from first to third plot in the bottom row) for a given image resolution. This issue can be of particular concern for CO-ZOOM where the reduction of the $\mathrm{FOV}_{\mathrm{PE}}$ is achieved as in this case. Depending on the size of the imaged object, the FOV_{iv} could potentially be tens of millimetres wide, thus being affected by signal inhomogeneity.

The slice thickness is usually defined in terms of the full width at half maximum (FWHM) of the signal curve in the frequency domain. From Fig. 3.15 it can be seen

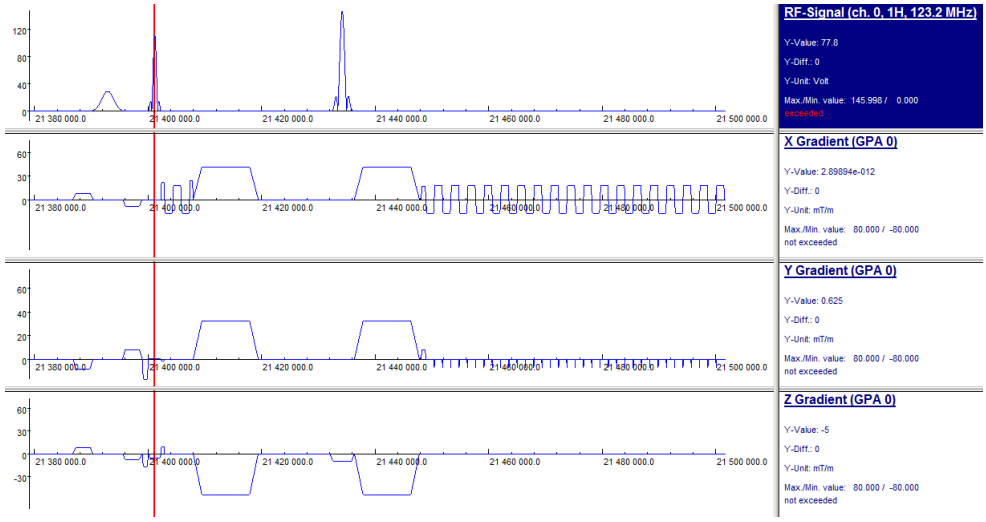

(a)

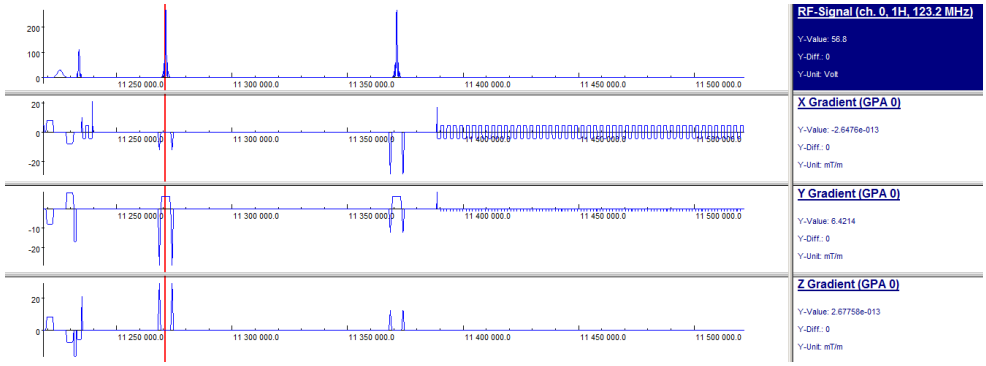

(b)

Fig. 3.13: Sequence simulations performed within IDEA. The values shown on the right for the gradient coils and the RF pulse generator refer to the position of the red cursor in the sequence scheme. For both simulations the rotation matrix **R** is the one shown in Eq. 3.14. (a) ZOOM sequence: during the excitation pulse the y gradient coil is activated to tilt the slice by an angle θ. Note that its numerical value on the right is significantly different from zero. No y gradient is present during the refocusing pulse. (b) CO-ZOOM sequence: during the refocusing pulses the z is turned off and only the y gradient is active to tilt the slice by $90°$. Note that its numerical value on the right is the only one significantly different from zero. No y gradient is present during the excitation pulse.

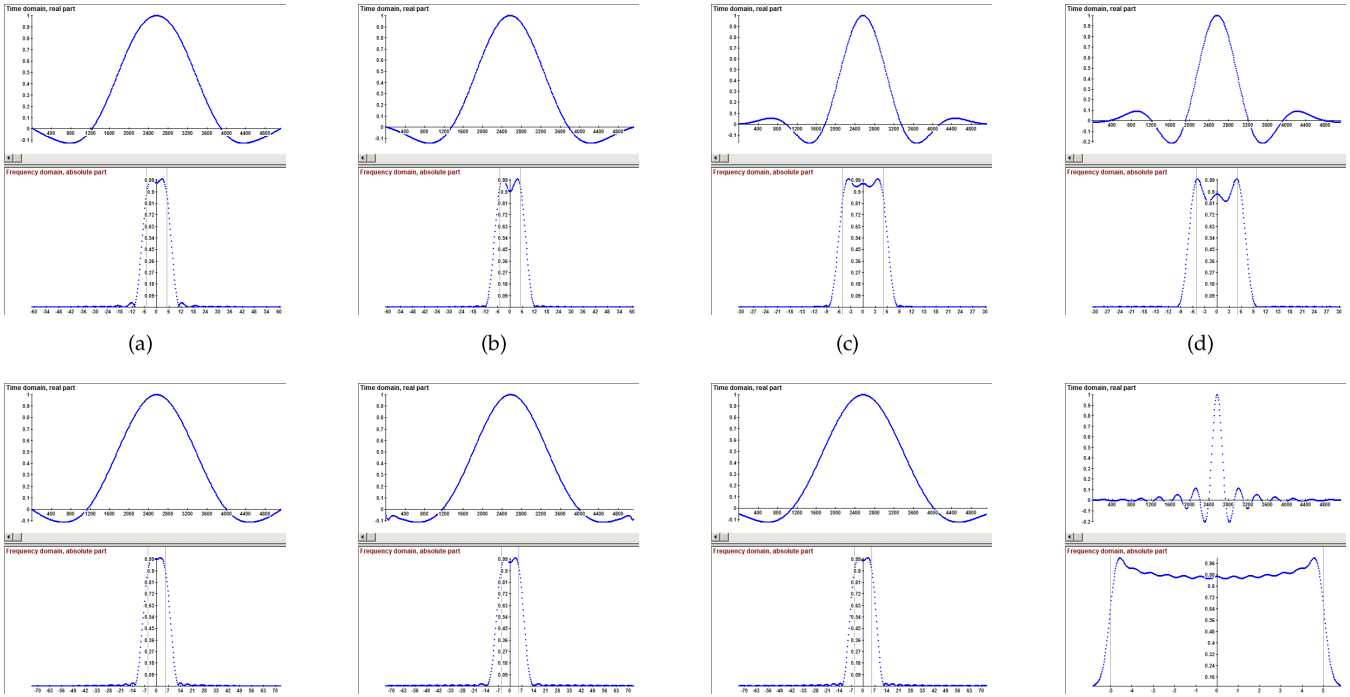

Fig. 3.14: Plots of the RF pulses profile. The top plot of each panel shows the real part of the pulse in the time domain, while the bottom plot shows its absolute part in the frequency domain (*i.e.* the slice profile). (a) and (b) show the standard pulses used in SE sequences for $\pi/2$ excitation and π refocusing respectively and for slice thickness ranging from $2.4\,\mathrm{mm}$ to $20\,\mathrm{mm}$. (c) and (d) show the respective pulses used when improved slice profile is required and for slice thickness ranging (nominally) from $1.0\,\mathrm{mm}$ to $500.0\,\mathrm{mm}$. These pulses are designed for 3D SE applications. (e) and (f) show alternative pulses for SE $\pi/2$ excitation recommended for slice thickness ranges $0.5\,\mathrm{mm}$ to $2.3\,\mathrm{mm}$ and $0.1\,\mathrm{mm}$ to $10.0\,\mathrm{mm}$ respectively. (g) shows an alternative pulse for π refocusing recommended for slice thickness ranging from $0.5\,\mathrm{mm}$ to $2.3\,\mathrm{mm}$. (h) shows a pulse designed for Turbo Spin Echo applications. Its recommended slice thickness range is $5.0\,\mathrm{mm}$ to $500.0\,\mathrm{mm}$. It is to note its large TBW and its smooth profile. This last pulse was used for 7 Tapplications illustrated in Sec. 3.4.3 and 3.4.4.

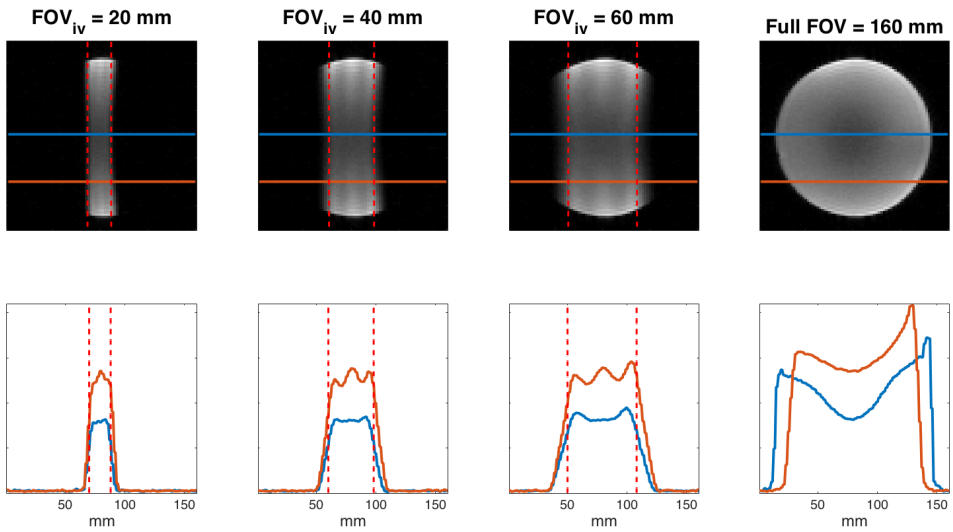

Fig. 3.15: Signal intensity across the acquired slice for different values of FOV_{iv}. A homogeneous cylindrical phantom was scanned at 3 T. The region is selected with the CO-ZOOM method, while acquiring the full FOV in the PE direction (160 mm, 2 mm isotropic voxels). Images are reported in the top row, where two horizontal lines are drawn. The signal intensity along these lines is reported in the respective plots in the bottom row. The dashed red lines represent the reduced FOV. The RF pulse shape is responsible for signal inhomogeneity across the selected region width. The shape of the pulse becomes more evident with increasing FOV_{iv}. The acquisition of the whole object is reported in the last column as a reference.

that the excited region outside the FOV_{iv} grows with increasing width of the slice. This means that, if the $\mathrm{FOV}_{\mathrm{PE}}$ is reduced to FOV_{iv} in a CO-ZOOM acquisition, there is the possibility to generate wrap-around artefacts in the selected region.

Both signal ripples and slice sharpness can be improved using RF pulses with better profiles, although this often leads to longer pulse durations and, hence, to longer TE.

Human Another effect relative to bad slice profile became evident with *in vivo* tests of the ZOOM sequence. An example is shown in Fig. 3.16, where coronal images of the cerebellum acquired at 3 T using ZOOM are displayed. A gap $G = 6\,\mathrm{mm}$ (corresponding to three slices) was used resulting in four interleaved sets of slices. In the displayed images the TBs have been already removed. It can be seen that the top of the first slice of each set exhibits a higher signal with respect to the remaining slices of the same set. As illustrated in Fig. 3.17, when slice I is excited by the oblique $\pi/2$ pulse, the top of slice V (which is the next slice to be acquired) is affected too and the magnetization of the red triangular region is moved away from the direction of the B_0 field. Therefore, when slice V is excited, if the magnetization in that area is not fully recovered, the signal is reduced. This mechanism is then repeated for all the following slices of the set.

There are different possible solutions to this problem. ZOOM parameters can be varied in order to reduce the extent of the affected regions of the following slices. For

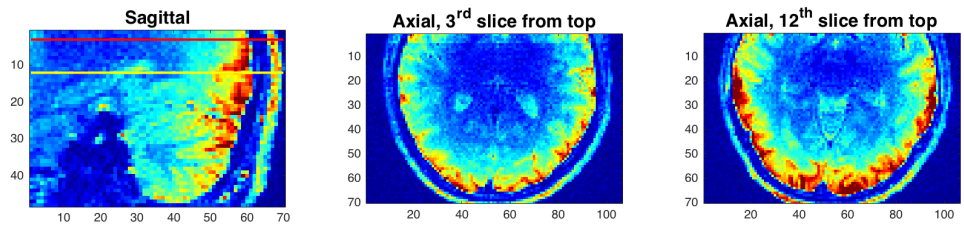

Fig. 3.16: Coronal image acquired with ZOOM. Here, the PE direction is feet - head (F→H), FOV reduction was achieved with a three slices gap and TBs were removed during post-processing. The first four slices (left of the sagittal view, top of the axial view) show higher signal at the top with respect to the following ones. This is caused by bad slice profile: Each of these four slices is the first of a set, as explained in Sec. 3.2 and in Fig. 3.7. The oblique pulse used to select the first slice of a set partially affects also the superior part of the next slice of the same set. The result is that a smaller amount of its magnetization is brought to the transverse plane, leading to reduced signal at the top of following slices.

example:

1. the gap G could be increased keeping the angle θ and the thickness of the oblique slice T_o fixed (this strategy was adopted for the protocol described in Sec. 3.4.1);

2. θ could be reduced keeping G and T_o fixed;

3. T_o could be reduced keeping G and θ fixed;

4. the slice acquisition order within a single slice set could be changed to minimize the effect of the oblique pulse on the next slice (*e.g.* from sequential to interleaved);

5. a combination of the previous solutions.

Unfortunately, most of these solutions has some disadvantages and the optimal acquisition must be evaluated on a case-by-case basis. An expanded G may lead to a further stretched TR, while a reduced θ means an extension of the TBs, thus reducing the impact of the reduced FOV on susceptibility-induced distortions and TE. The reduction of T_o could reduce the effect of the oblique pulse on the next slice at the cost of a partial excitation of the current slice. Alternatively, an RF pulse with a better profile could be chosen, but again with longer pulse duration and TE.

3.4 ZOOM imaging of the cerebellum and the brainstem

This section describes ZOOM and CO-ZOOM protocols for imaging of the cerebellum at 3 T and 7 T. Preliminary results from an application of ZOOM imaging of the brainstem are also presented.

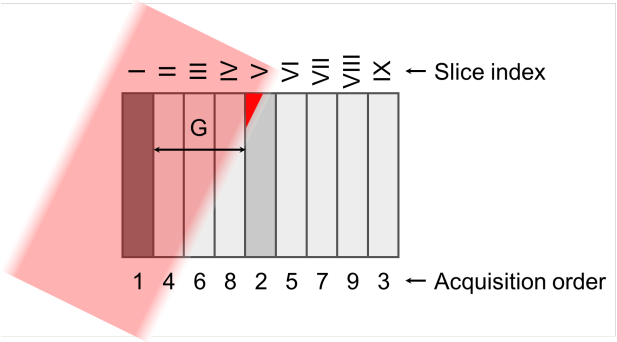

Fig. 3.17: Effect of broad slice profile. Slice I is excited by the $\pi/2$ RF pulse (red shaded regions). The planned gap is three slices thick, but the top of slice V (that according to the acquisition order is the second one to be acquired) is also partially excited (red triangle) because of broad pulse shape. This causes signal drop in that region is the magnetization is not fully recovered when slice V is excited.

3.4.1 Cerebellum at 3 T - ZOOM

As explained in the previous paragraphs, an imperfect slice profile can reduce the signal of certain slices in a ZOOM protocol. Among the proposed solutions there is the possibility to set a gap G larger than required by the remaining ZOOM parameters. Here, we report an example of such method. An healthy volunteer was scanned using a $3\,\mathrm{T}$ Prisma MRI scanner and a 32 channels head coil. Slice thickness was set to $1.5\,\mathrm{mm}$ and ZOOM parameters θ and T_o were set to allow $G \geq 3\,\mathrm{mm}$ (2 slices), but $G = 4.5\,\mathrm{mm}$ (3 slices) was set instead. Tab. 3.1 reports the protocol details and Fig. 3.18 shows the results. For each slice set no signal drop was observed in those slices acquired after the first one (*cf.* Fig. 3.16). However, setting $G = 3\,\mathrm{slices}$ instead of $G = 2\,\mathrm{slices}$ demanded proportionally longer TR.

3.4.2 Cerebellum at 3 T - CO-ZOOM

As mentioned in Sec. 3.2.2, the steady state signal produced by CO-ZOOM depends on the TR/n ratio, where n represents the number of slices. In Fig. 3.19 this dependency is illustrated in a scan of the cerebellum. An healthy volunteer was scanned using a $3\,\mathrm{T}$ Prisma MRI scanner and a 32 channels head coil. Protocol details are summarised in Tab. 3.1. The TR/n ratio ranges from $3800\,\mathrm{ms\,slice^{-1}}$ ($\mathrm{TR} = 3800\,\mathrm{ms}$ and 1 slice only, top left) to $84\,\mathrm{ms\,slice^{-1}}$ ($\mathrm{TR} = 3800\,\mathrm{ms}$ and 45 slices, bottom right). The SNR drastically drops for $\mathrm{TR}/n \lessapprox 500\,\mathrm{ms\,slice^{-1}}$. Despite the RF pulse used here for double refocusing is the same used in the phantom test (see Fig. 3.14d), its intensity profile is not visible (*cf.* Fig. 3.15).

3.4.3 Cerebellum at 7 T - ZOOM

UHF can bring considerable benefits in terms of enhanced signal intensity, improved contrast and resolution, but at the cost of greater field inhomogeneities and larger dis-

	ZOOM 3 T	CO-ZOOM 3 T	ZOOM 7 T
Voxel size (mm^3)	$1.5 \times 1.5 \times 1.5$	$2.0 \times 2.0 \times 2.0$	$1.3 \times 1.3 \times 1.3$
N. of slices	100	1 3 45 45	45
Distance factor (mm^3)	0	0	0
PE direction	A→P (Sagittal)	F→H (Coronal)	A→P (Axial)
FOV (mm^2) (RO × PE)	160.0×108.8	160.0×72.0	160.0×120.0
TR (ms)	20000	3800 3800 20000 3800	9000
TE (ms)	70	55	56
Acquisition matrix (RO × PE)	106×72	80×36	128×96
PPF	-	$6/8$	$6/8$
PAT	-	-	GRAPPA 2 (24 ref. lines PE)
Diffusion mode	Monopolar	Bipolar	Monopolar
b-values (s/mm^2)	0 - 2000	0	0 - 700 - 1000
N. of diff. dirs. per shell	30	-	30
BW (Hz/pixel)	1522	2016	1860
Reduced FOV method	ZOOM	CO-ZOOM	ZOOM
FOV_{iv} (mm)	72.0	72.0	80.0
Gap factor [G] (n. of slices)	3	-	2
Angle [θ]	2.4°	-	-
Obl. slice thk. [T_o] (mm)	45	-	-

Tab. 3.1: Protocol details for applications in Sec. 3.4.1, 3.4.2 and 3.4.3.

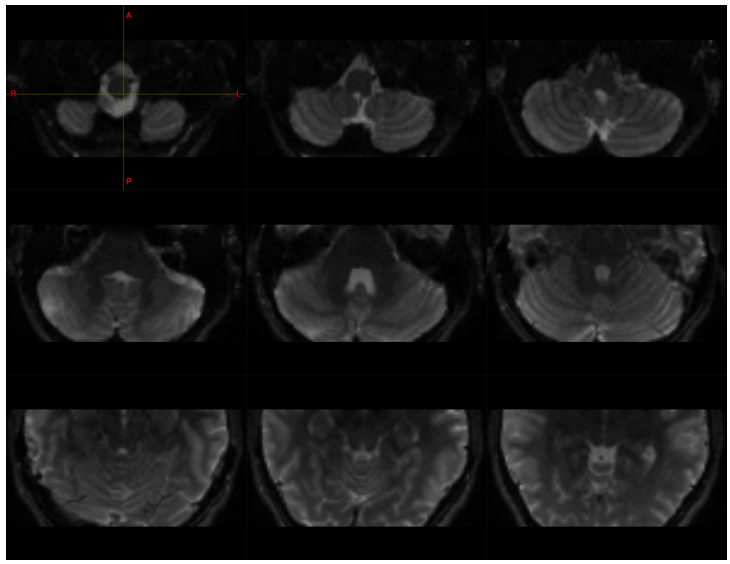

(a)

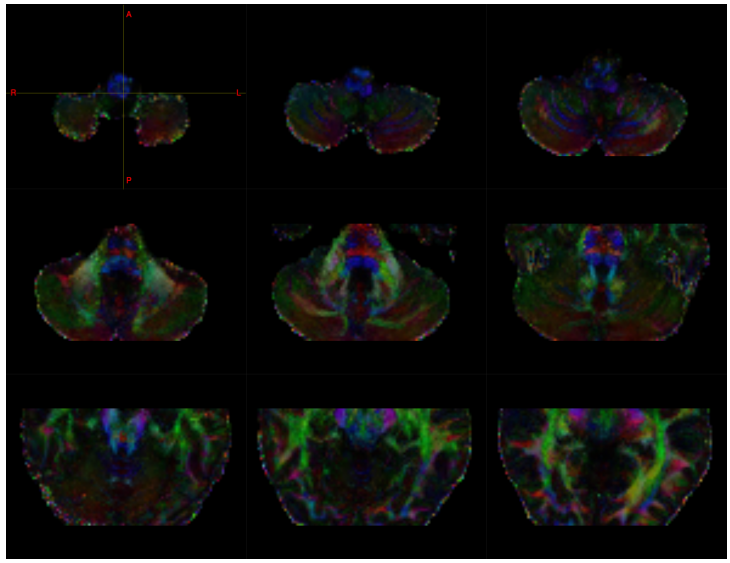

(b)

Fig. 3.18: ZOOM images of the cerebellum at $3\,\mathrm{T}$. (a) $b = 0\,\mathrm{s/mm^2}$ image of the cerebellum obtained after preprocessing and removal of the TBs. No signal loss due to poor slice profile can be observed. (b) Corresponding FA map colour coded according to the principal direction of the diffusion tensor.

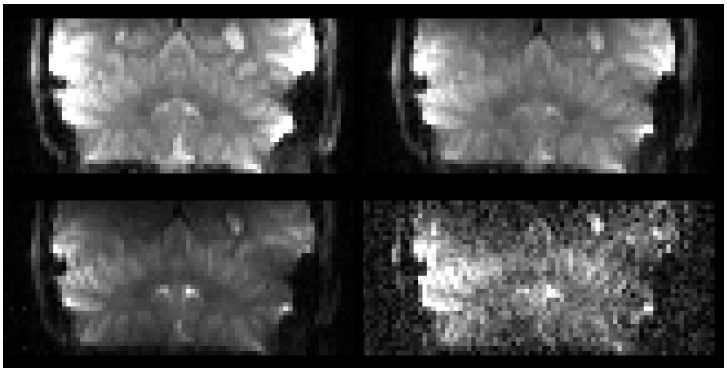

Fig. 3.19: CO-ZOOM images of the cerebellum at $3\,\mathrm{T}$. It is possible to note the signal dependency on the ratio TR/n, which assumes the values $3800\,\mathrm{ms/slice}$ (top left), $1267\,\mathrm{ms/slice}$ (top right), $444\,\mathrm{ms/slice}$ (bottom left) and $84\,\mathrm{ms/slice}$ (bottom right). The image windowing parameters are kept fixed for all images but the last one, where a lower maximum value was set for display purposes.

tortions.

Here, we show an application of the ZOOM method at $7\,\mathrm{T}$ for diffusion imaging of the whole cerebellum. An healthy volunteer was scanned using a $7\,\mathrm{T}$ Magnetom MRI scanner and a 32 channels head coil. The resolution is $1.3\,\mathrm{mm}$ isotropic. Protocol details are provided in Tab. 3.1. The strategy adopted here to avoid the signal drop explained in Sec. 3.3.3 was to use an RF pulse with a better slice profile (see Fig. 3.14h). Therefore, we set all ZOOM parameters for a gap as thick as two slices. Resulting $b = 0\,\mathrm{s/mm^2}$ image and FA map colour coded according to the tensor principal direction are shown in Fig. 3.20a and b respectively.

Despite the shimming procedure, relevant field inhomogeneities could still be observed. In particular, the region of the cerebellum is often characterised by low signal, probably also due to the geometrical arrangement of the receiver coil elements. Signal intensity in this region can be increased by using dielectric pads. These are envelops filled with conductive materials and they are placed between the subject and the receiver coil. However, remarkable experience is needed to position correctly the pads. In Fig. 3.20a it is possible to notice that the signal is more intense in the right hemisphere of the cerebellum (left of the picture) with respect to the left hemisphere. This signal inhomogeneity is due to misplacement of the pads. Although there is no evident effect in the resulting FA map, particular care should be taken when placing the pads, especially if quantitative measures are planned. Moreover, if not placed with care, they can be uncomfortable for the subject.

3.4.4 Brainstem at 7 T - ZOOM

The ZOOM sequence was also tested for a combined fMRI and dMRI study of the human brainstem at $7\,\mathrm{T}$.

The brainstem plays a pivotal role in the CNS. It links the spinal cord, the cerebellum

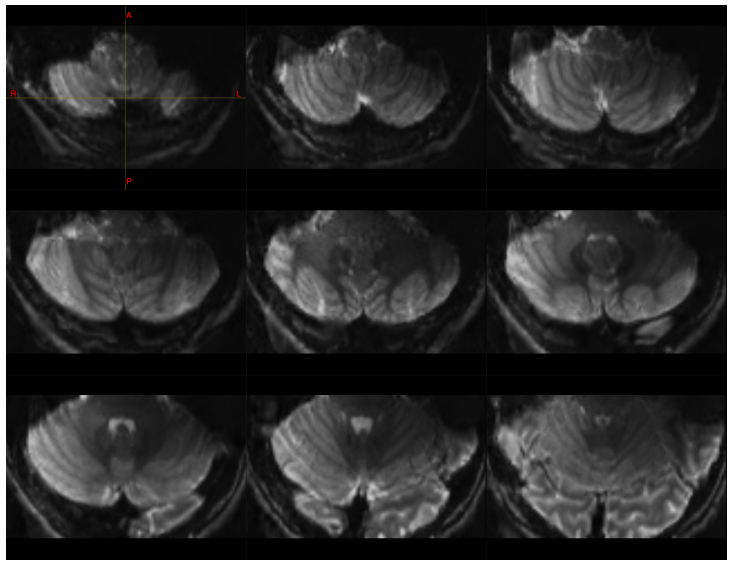

(a)

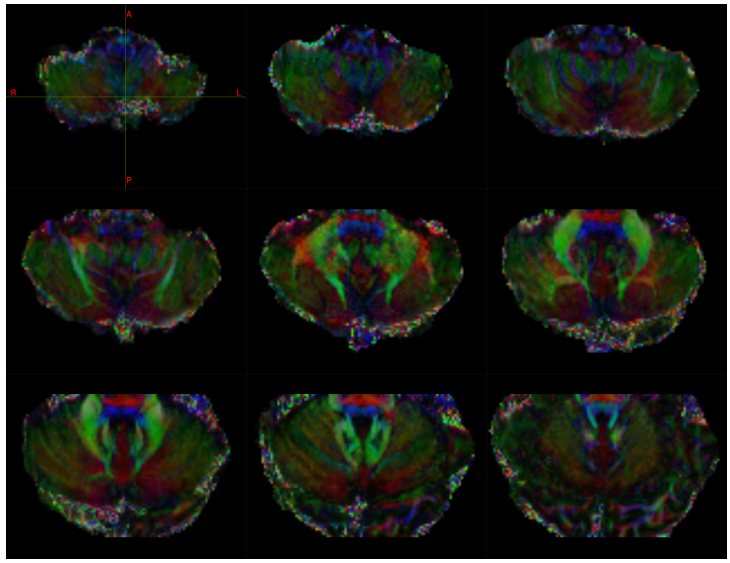

(b)

Fig. 3.20: ZOOM images of the cerebellum at 7 T. (a) $b = 0\,\mathrm{s/mm^2}$ image of the cerebellum obtained after preprocessing and removal of the TBs. It is possible to observe that the left hemisphere of the cerebellum is brighter than the right hemisphere. This could be caused by a misplacement of the dielectric pads, which were used during the acquisition to increase the signal in the cerebellum because of its poor coverage provided by the coil elements. Another plausible cause of this signal hypointensity may be field inhomogeneity, which could result in a non uniform flip angle of the refocusing pulse across the volume of interest. (b) Corresponding FA map colour coded according to the principal direction of the diffusion tensor.

	ZOOM	Full FOV
FOV (mm^2) (RO × PE)	70.0×52.5	220.0×220.0
Acquisition matrix (RO × PE)	64×48	200×200
FOV_{iv} (mm)	70.0×35.0	-
Gap factor [G] (n. of slices)	2	-
BW (Hz/pixel)	1924	1860

ZOOM	Z1	Z2	Z3	Z4
PPF	-	6/8	-	-
GRAPPA	-	-	2	3
TR (ms)	70	46	46	36
TE (ms)	9000	9000	9000	9000
Full FOV	F1	F2	F3	F4
PPF	6/8	-	6/8	6/8
GRAPPA	-	2	2	3
TR (ms)	122	120	70	54
TE (ms)	10800	8500	6200	5000

Tab. 3.2: Protocols details for the assessment of susceptibility-induced distortions at $7\,\mathrm{T}$ with different combinations of ZOOM, PPF and parallel imaging (see Sec. 3.4.4). The parameters common to all protocols are: A→P PE direction, $1.1 \times 1.1\mathrm{mm}^2$ in-plane resolution, $2.0\,\mathrm{mm}$ slice thickness, 46 slices, 8 averages. The table on the left illustrates parameters common to all ZOOM (Z1-Z4) and full FOV (F1-F4) protocols respectively. The table on the right shows the different combinations of parallel imaging and PPF. For F1-F4 protocols the minimum possible TR is set. For Z1-Z4 the TR is kept fixed to allow magnetization recovery in each set of slices.

and the cerebrum and it is made of a large number of small relay nuclei that regulate many of their functions (Sclocco et al., 2017). Consequently, it exhibits a very intricate fibre geometry. Despite its relevance from both a physiological and functional point of view, its investigation with MRI has always been hindered by many factors that include:

- the small size of its constituents that makes them hardly resolvable;
- its susceptibility to physiological (cardiac and respiratory) noise because of its proximity to the neck and to large blood vessels (Brooks et al., 2013);
- its proximity to the oral cavity where a strong air-tissue susceptibility gradient exists.

All these factors constitute a major limitation for fMRI and dMRI studies which make use of EPI-based sequences. As illustrated in Sec. 3.1, with UHF signal and resolution can be increased, but at the cost of larger susceptibility-induced distortions. Therefore, reduced FOV imaging can help in mitigating the effect of such distortions.

Therefore, here we compared image quality from full and reduced FOV protocols at $7\,\mathrm{T}$ using the developed ZOOM sequence for SE EPI with high in-plane resolution. The optimised protocol was then used for a pilot fMRI and dMRI study with matching distortions.

Measurements were performed on a 47 years old right-handed healthy subject. We tested eight different combinations of full (four protocols labelled F1-F4) and reduced FOV (four protocols labelled Z1-Z4), PPF and parallel imaging. Each of these protocols guaranteed full coverage of the brainstem; in-plane resolution was $1.1\,\mathrm{mm} \times 1.1\,\mathrm{mm}$ and slice thickness was $2.0\,\mathrm{mm}$. Protocols details are provided in Tab. 3.2. Fig. 3.21 shows the positioning of the subject and of the imaging slab for ZOOM imaging of the brainstem. In order to improve the slice profile, the RF pulse shown in Fig. 3.14h was used for oblique slices.

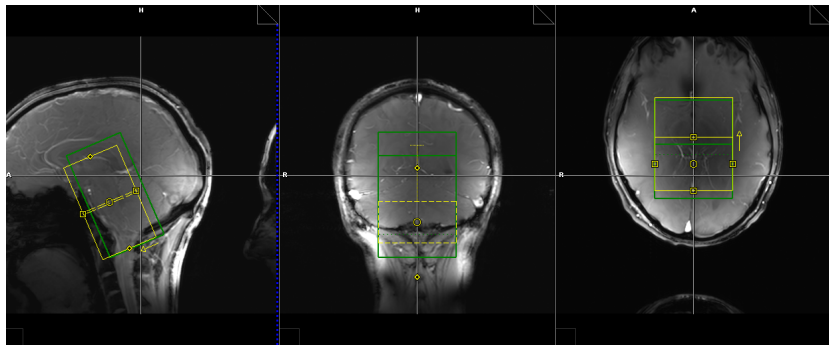

Fig. 3.21: Scan planning for ZOOM imaging of the brainstem.

Results are shown in Fig. 3.23 and 3.22. Full FOV images were cropped to match ZOOM acquisition FOV for display purposes. The protocol Z2 was judged to provide the best compromise in terms of SNR, distortions and absence of reconstruction artefacts from parallel imaging and it was then used for SE fMRI and dMRI of the brainstem.

For fMRI acquisition the subject performed a finger tapping task using his right hand. The paradigm followed a block design with block duration of $30\,\mathrm{s}$ and 150 volumes were acquired. In order to reduce the signal originating from large blood vessels, a $b = 50\,\mathrm{s/mm^2}$ monopolar diffusion weighting was applied along the z-axis. Physiological data (heart beat, respiration and concentration of O_2 and CO_2) were continuously recorded throughout acquisition for subsequent correction of fMRI data. Identical geometric parameters were maintained for dMRI acquisition. The protocol included also the acquisition of two volumes with no diffusion weighting ($b = 0\,\mathrm{s/mm^2}$) and reversed PE direction to correct remaining susceptibility distortions and a high resolution T1w scan for structural reference. The total duration of the scan was approximately $1\,\mathrm{h}$.

The analysis of functional data was performed according to the following pipeline: first, slice-by-slice RETROICOR was applied for physiological noise correction (Glover et al., 2000); it was followed by slice timing, smoothing and data processing performed with SPM [2]. Diffusion data analysis included correction for susceptibility-induced distortions, motion and eddy currents and it was performed with FSL [3] (Jenkinson et al., 2012). The diffusion tensor model was fitted to data and it was followed by CSD (Tournier et al., 2007) and probabilistic tractography performed with MRtrix [4] (Tournier et al., 2012).

Results obtained from fMRI analysis are shown in Fig. 3.24. High resolution imaging of the brainstem can be crucial to correctly identify small structures and can help to disentangle the BOLD signal of the nuclei from surrounding physiological noise sources. However, the lack of contrast between GM and WM in the brainstem in T2w (T2*w) and T1w images constitutes a further obstacle for the identification of small nuclei. The potential of diffusion maps and tensor derived metrics in this issue have been shown, for

[2] http://www.fil.ion.ucl.ac.uk/spm
[3] https://fsl.fmrib.ox.ac.uk/fsl/fslwiki
[4] http://www.mrtrix.org

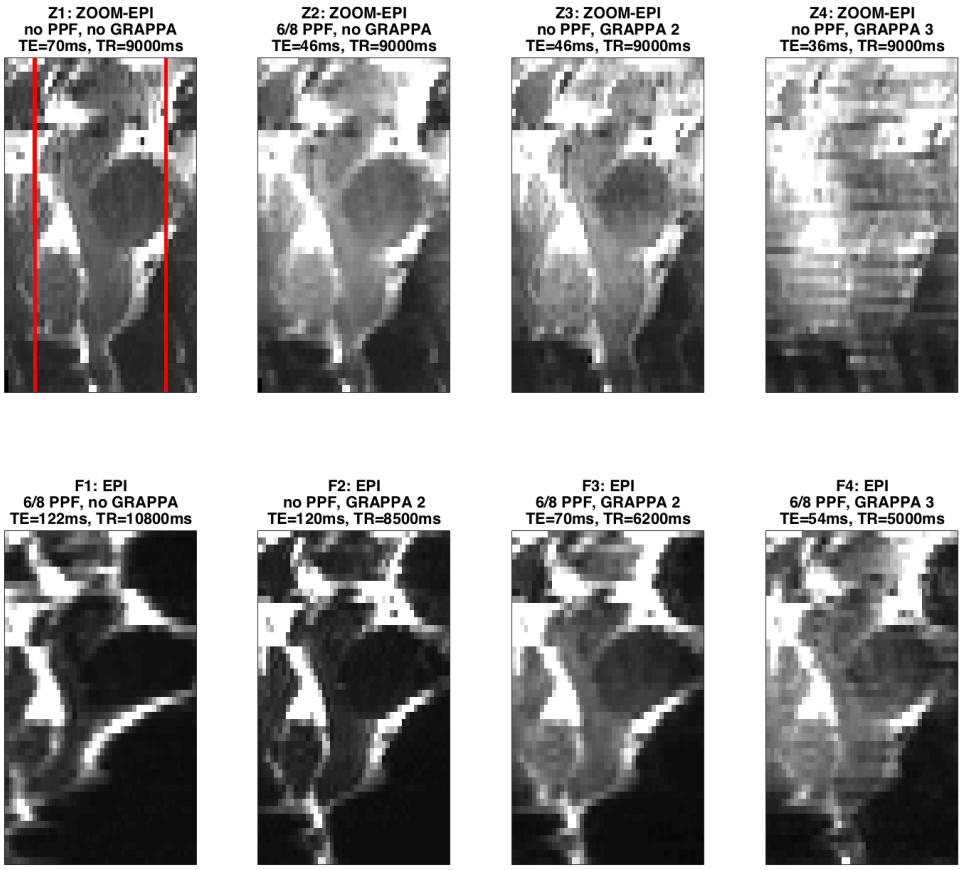

Fig. 3.22: Susceptibility-induced EPI distortions assessment with different combinations of parallel imaging (GRAPPA) and PPF. Top row: reduced FOV ZOOM EPI images: transition bands (side regions beyond red lines) can exhibit wraparound artefacts and must be removed. Bottom row: full FOV EPI images: these were cropped to match ZOOM acquisition FOV for display purposes.

example, by Bianciardi et al. (2015), who showed that some nuclei are more visible on FA maps. In addition to this, we reckon that fibre tracking may provide further anatomical details (see Fig. 3.25). Moreover, more advanced and/or complex microstructural models may provide new metrics for enhanced contrast and characterization of the brainstem nuclei.

Although this analysis was conducted in a single subject, our results are in line with findings previously reported in literature (Pattinson et al., 2009; Faull et al., 2015): we found significant activations in the *medulla oblongata* in correspondence to the pyramidal decussation (see Fig. 3.24a and 3.25a and c), which is pertaining to the motor pathway, and to the ipsilateral (right) *cuneate nucleus* (see Fig. 3.24b and 3.25b and d), which is

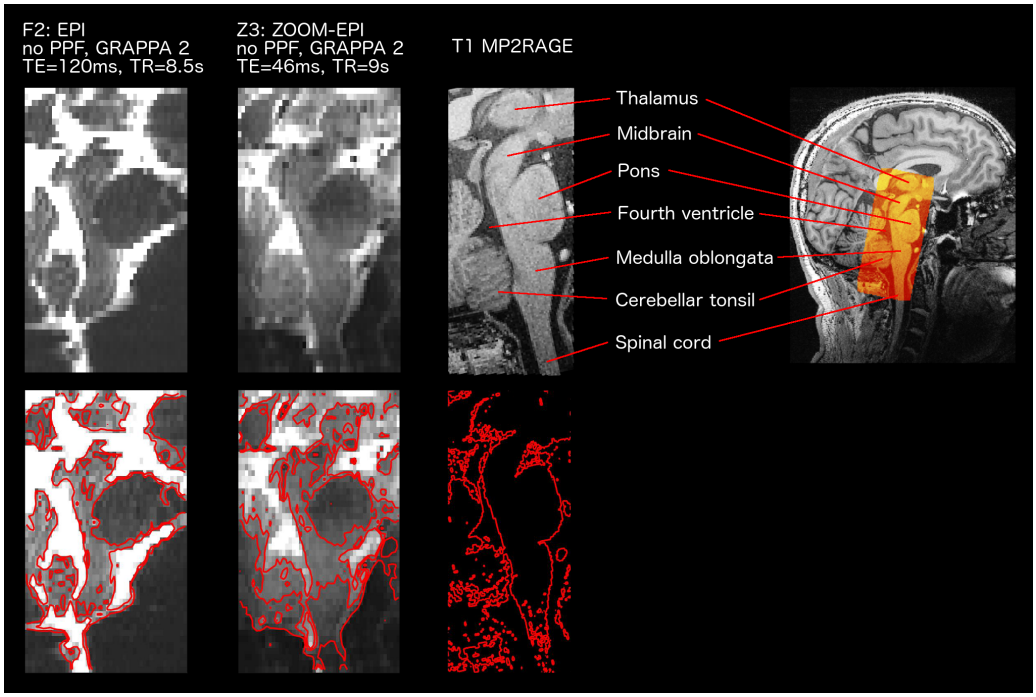

Fig. 3.23: Contour plot overlay showing the sagittal section of the pons obtained with full FOV EPI with GRAPPA factor 2 and no PPF (left), ZOOM EPI with with GRAPPA factor 2 and no PPF (centre) and T1w structural reference (right). The highlighted region shows the reduced FOV. The full FOV EPI image was cropped to match the ZOOM acquisition FOV for display purposes.

pertaining to the sensory pathway involved in fine touch and proprioception.

Compared to standard EPI acquisitions, reduced FOV techniques confer relevant enhancements for brainstem imaging in terms of shorter TE, increased SNR and mitigated distortions. These benefits can be successfully exploited for high resolution functional and diffusion imaging of the brainstem at UHF.

A final consideration is necessary: FOV reduction using ZOOM is based on SE EPI. Which one of SE and gradient echo (GRE) fMRI provides the best specificity and sensitivity to BOLD signal is still matter of debate. Within ZOOM technique, T2* weighting could be retrieved by shifting the readout echo train with respect to the formation of the SE peak. However, this would lead to much longer TEs with respect to standard GRE-based sequences and, therefore, different methods for FOV reduction could be advisable.

3.4.5 Limitations

To conclude, we summarise here the main limitations encountered for reduced FOV techniques ZOOM and CO-ZOOM, with a particular focus at cerebellar applications. The long TR represents probably the main limitation for both methods.

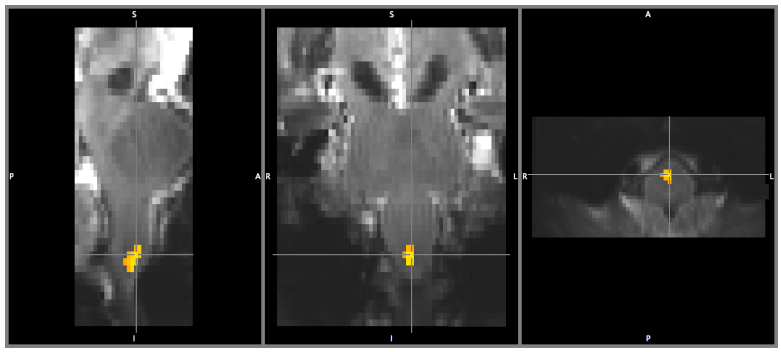

(a)

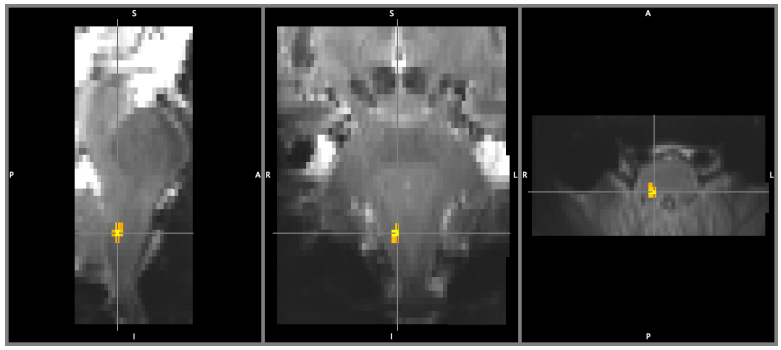

(b)

Fig. 3.24: fMRI activations in the medulla oblongata. (a) Ipsilateral cuneate nucleus. Bottom panel: pyramidal decussation. EPI distortion correction was not applied at this stage yet.

ZOOM In Sec. 3.2.1 we have shown that, in order to prevent cross-talk effects across slices, a gap of N slices is required, thus dividing the whole stack of slices in $N+1$ sets. One "standard" TR must then be dedicated to each set, resulting in an acquisition time equal to $(N+1)\times \mathrm{TR}$ for the whole volume of interest. This could hamper the applicability of the method in particular in fMRI experiments, where high temporal resolution is required to measure accurately the neuronal activity. Despite this, we have shown at 7 T that ZOOM SE fMRI is possible and that it provides reliable results. The long acquisition time needed for ZOOM affects of course also diffusion imaging. However, since there is no constrain for temporal resolution, ZOOM can be applied with no effect on data, even though it might not be suited for clinical settings where patients are involved.

Our specific implementation of ZOOM may lead to a partial reduction of the total scan time: considering that the $\pi/2$ excitation pulse is tilted (instead of the π refocusing pulse) and that, consequently, most of the magnetization should be recovered after $3\,\mathrm{T}_1$, the TR for the acquisition of the whole volume could be shortened approximately to $3(N+1)\mathrm{T}_1$. However, dummy scans preceding the proper acquisition should be run in order to allow the signal to reach the steady state and signal loss should be expected.

Let's consider now imaging of the cerebellum. The cerebellum is a "small" organ

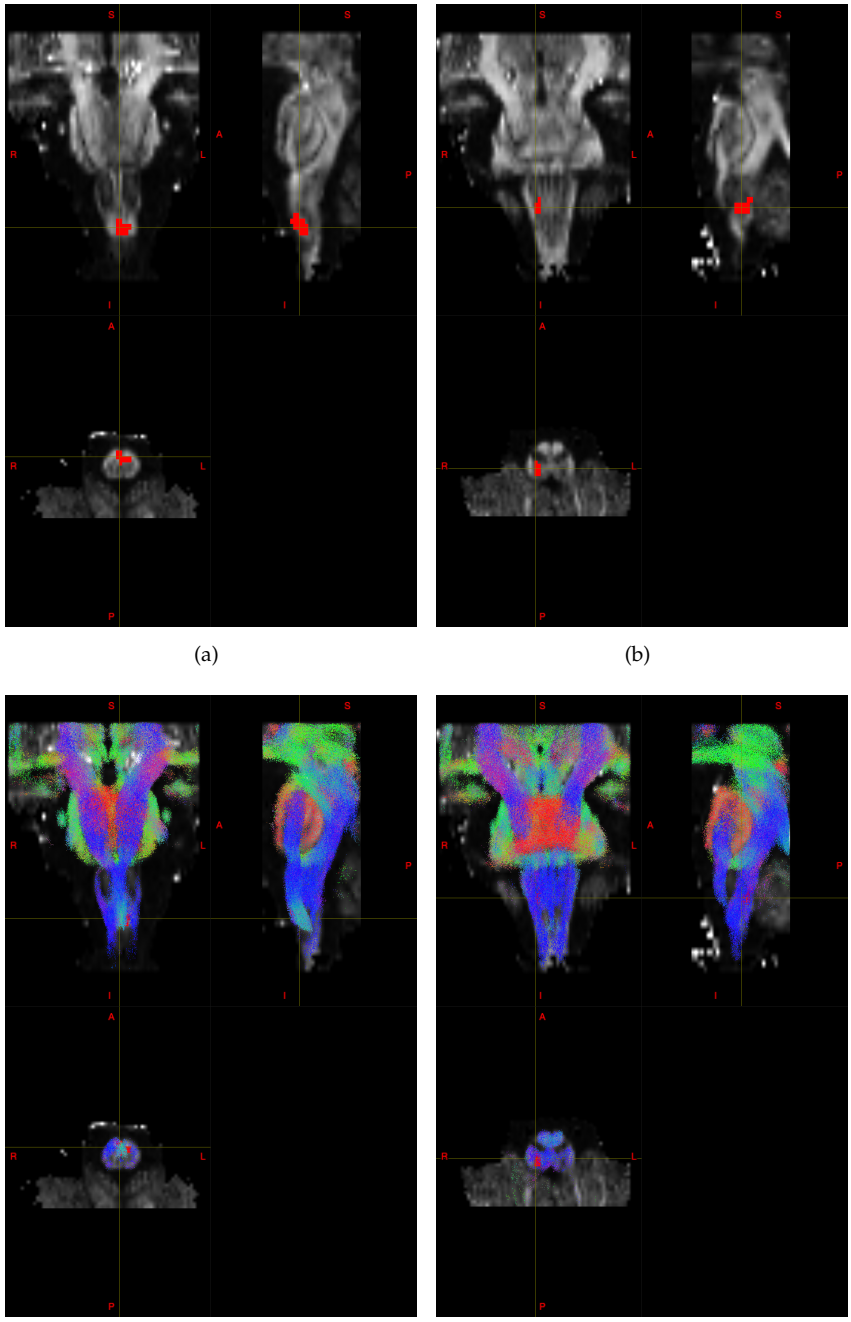

(a) (b)

(c) (d)

Fig. 3.25: fMRI activations in correspondence of the pyramidal decussation (a and c) and of the the cuneate nucleus (b and d) displayed overlaid on FA maps (a and b) and on probabilistic tractography of the brainstem (c and d) after EPI distortion correction. The cursor points at the activations.

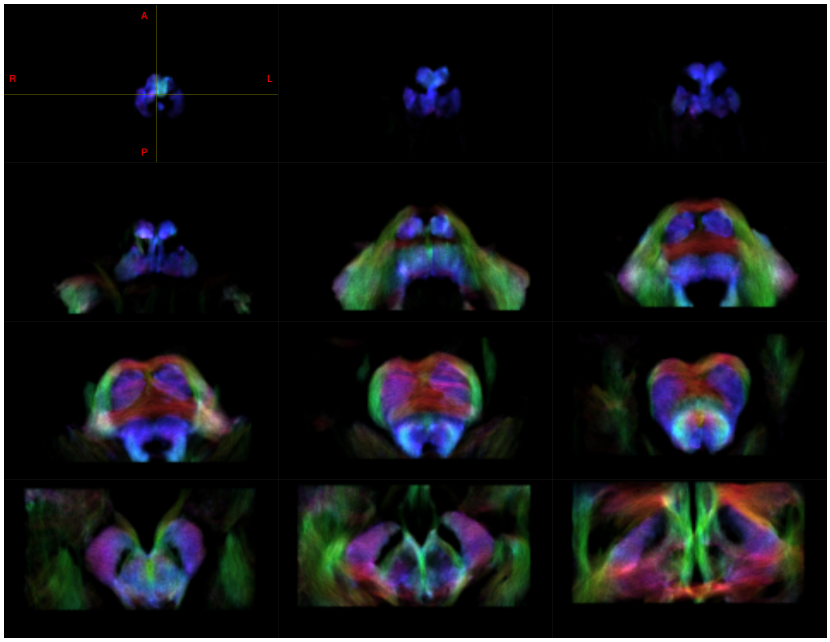

(a)

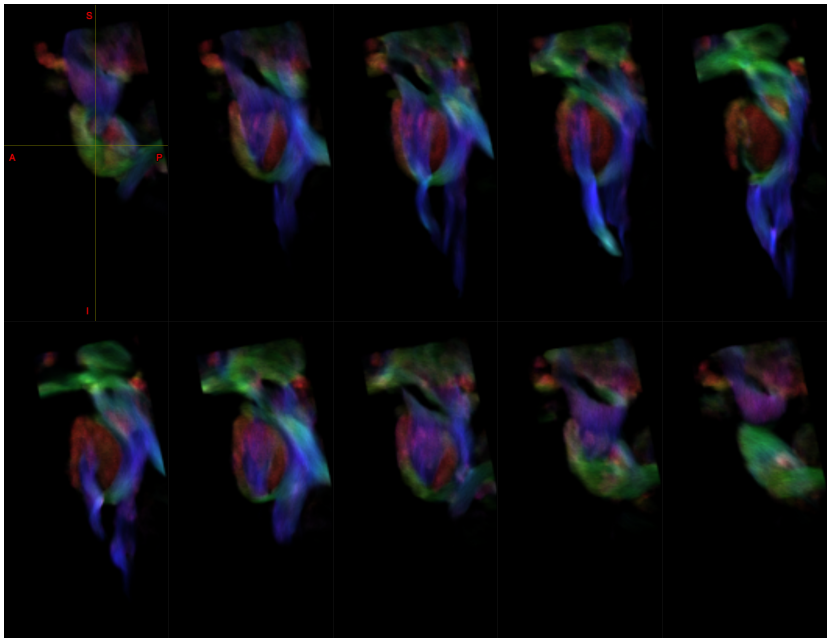

(b)

Fig. 3.26: TDI of the brainstem resampled at $0.5\,\mathrm{mm}$ isotropic resolution and colour encoded according to fibres direction (Calamante et al., 2010). (a) Axial view. (b) Sagittal view.

when compared to the brain, but its dimensions are on average $6\,\mathrm{cm} \times 5\,\mathrm{cm} \times 10\,\mathrm{cm}$ (anterior - posterior, superior - inferior, left - right directions respectively). Consider A→P PE direction. If, for the specific purpose of the scan, the pons must be included in the PE FOV_{iv} this should be increased by approximately $2\,\mathrm{cm}$. A one-slice gap leads to $\mathrm{FOV}_{min} = 2\,\mathrm{FOV}_{iv}$, a two-slice gap to $\mathrm{FOV}_{min} = 1.5\,\mathrm{FOV}_{iv}$ and so on (see Eq. 3.8). In case of imaging of the cerebellum and the pons, it means $\mathrm{FOV}_{min} = 16\,\mathrm{cm}$ and $\mathrm{FOV}_{min} = 12\,\mathrm{cm}$ respectively with acquisition times $\cong (N+1) \times \mathrm{TR}$ correspondingly increasing with the gap size N. Therefore, in order to maintain acceptable scan times, the gap size N must be kept small and a FOV_{min} nearly as large as the brain size must be acquired, thus nearly nullifying the reduction of distortions. Consequently, ZOOM may not be convenient to image the whole cerebellum, but it could be more suitable to investigate its substructures individually, like the pons, the cerebellar nuclei or its cortical convolutions.

One last limitation of the current implementation is that an appropriate image reconstruction that takes into account the TBs and the reduction of the FOV has not been developed yet. Consequently, at the moment, TBs must be manually removed by the user during image processing.

CO-ZOOM CO-ZOOM overcomes the issues of gap and TBs that occur with ZOOM. The absence of TBs allows the reduction of the FOV to the real size of the desired object and, consequently, the optimal reduction of distortions. However, despite the absence of a gap like in ZOOM, a long TR is still required for CO-ZOOM to allow signal recovery between two pairs of π refocusing pulses. When experimental requirements include high spatial resolution also in the SS direction, the total number of slices n can be high and this leads to low SNR, which depends on the quantity TR/n. Therefore, for fixed TR, SNR could be improved by reducing the number of slices (if possible) or the number of pairs of refocusing pulses. This could be achieved, for example, by applying recently developed simultaneous multi-slice (SMS) techniques (also known as multi-band (MB)) like CAIPIRINHA (Setsompop et al., 2012). If m slices can be excited and acquired simultaneously the number of refocusing pulse pairs is reduced too, thus leaving more time for magnetization recovery in the following slices. $m = 3$ can be considered a standard acceleration factor for MB acquisitions (higher factors are also possible) and, in this case, the ratio TR/n would be multiplied by a factor 3, thus improving the SNR.

We have seen that the quality of the slice profile is an important factor for CO-ZOOM: in case of poor slice profile quality, signal inhomogeneity may appear when the target object and FOV_{iv} are larger than few tens of millimetres, as in the case of the cerebellum. Therefore, RF pulses with good profile should be used, but they can lead to high SAR values, which could be critical at UHF. If a proper pulse shape can not be adopted, CO-ZOOM should be recommended for smaller structures only.

Parallel transmit technology can help in reducing the SAR caused by both MB excitation pulses and refocusing pulses with sharp slice profile.

Finally, CO-ZOOM must forcedly adopt a bipolar scheme for diffusion encoding. This is good in terms of distortions generated by eddy currents, but it also increases the minimum TE and, consequently, reduces the signal. Moreover, stronger diffusion

weightings imply longer duration of the diffusion encoding gradients, including those that are run between the two π pulses, thus separating them and leading to further signal decrease.

Conclusions

The cerebellum is one of the current great challenges of MRI and it represents an unexplored field in many respects. In this thesis we addressed different aspects of MRI of the cerebellum, starting from the its role in cognition in health and pathology, to cerebellar microstructure, to acquisition strategies.

In particular, we showed that cortico-cerebellar connectivity plays an important role in information processing speed performance. dMRI allowed us to track and reconstruct bundles of WM fibres connecting the cerebellum with brain cortical regions involved in the DMN. DTI measures combined with graph metrics of the reconstructed network provided an estimate of the network structural efficiency, which resulted to be reduced in MS pathology and to be associated with cognitive processing decline. Cerebro-cerebellar tracts strengthened the correlation between network structural efficiency and information processing speed performance in MS, thus indicating that MS-related structural alterations of these tracts affects cognition-relevant network functioning. However, the limitations of tractography algorithms met in regions of crossing fibres like the brainstem, where peduncles decussation takes place, and the use of DTI measures, which are sensitive but not specific to microstructural damage, may have limited the strength of results and their impact.

Therefore, we investigated cerebellar microstructure by analysing high quality $3\,\mathrm{T}$ MRI data with advanced computational models to gain a closer mapping of biologically relevant features. Both T1w and T2w images and diffusion maps were found to be sufficiently sensitive to detect significant differences in cerebellar cortex subregions. These inhomogeneities show evident similarities with maps of cerebellar functional topography and there are correspondences also with known local differences in cortical histology. However, comparison of MRI data with histology is necessary to establish a link between the MRI signal and microscopic features of cerebellar tissues and to validate these results. Despite the already great image quality of the Human Connectome Project Data used for this study, more efforts should be made to get an optimal cerebellum-specific acquisition: in particular, spatial resolution makes partial volume effects critical in small structures like cerebellar lobules and folia, thus affecting the computation and interpretation of regional average microstructural parameters, and susceptibility-induced distortions still made the 25% of data unusable. Therefore, it is advisable to

adopt reduced FOV sequences for imaging the cerebellum and of its substructures, thus allowing improved spatial resolution, reduced partial volume effect, shorter TE and mitigated distortions.

We showed that the acquisition of a reduced FOV is effective in mitigating distortions induced by susceptibility gradients in EPI-based sequences. ZOOM and CO-ZOOM sequences provide precious benefits also in terms of TE, and thus in terms of SNR, especially if compared to other sequences that make use of RF pulses to reduce the FOV. However, we have shown that the long TR represents the main limitation to their applicability in dMRI and fMRI studies. Moreover, ZOOM requires the acquisition of transition bands and, therefore, its use is recommended when a significant reduction of PE FOV is desired, as for imaging DCN. On the other hand, given the signal dependency on its TR/n ratio, CO-ZOOM is indicated when the number of slices n is small. As it commonly happens in MRI, a trade-off must be made between image quality and acquisition time. The target of the study determines the effectiveness and, consequently, the choice of the most appropriate reduced FOV method.

There are still several open questions regarding the cerebellum and its role in the CNS and multi-modal MRI can help to better understand how microscopic tissue properties integrate with each other and with distant regions to give rise to behaviour. Imaging of the cerebellum brings out new and different problems than those previously dealt with in the brain and these may require new technological solutions (*e.g.* dedicated sequences or coils). On the front of dMRI, new specific models should be developed and validated to better characterise cerebellar microstructure and to perform microstructurally-informed tractography of such an important, but complex, organ. It is appropriate therefore to conclude that there is still a long way to go to get to the complete characterization cerebellar structure and function, creating exciting challenges to the neuroimaging community.

APPENDIX A

The cerebellum

Here is provided a brief overview about cerebellar anatomy, cyto-architecture, connectivity and functions, to serve as reference for contents in Chap. 1 and 2.

Regarding principles, theory and applications of MRI and dMRI and pulse sequence design, the reader is referred to the following excellent textbooks.

- For physical principles of MRI Paul T. Callaghan (1993) (more focused on nuclear magnetic resonance principle) and Brown et al. (2014b) (more specific for MR imaging principles).
- For MRI pulse sequence design Brown et al. (2014b) for a more introductory text, Bernstein et al. (2004) for a comprehensive text and Schmitt et al. (1998) for a monograph on EPI.
- For dMRI theory, modelling, tractography and applications Jones (2010), Mori & Tournier (2014) and Johansen-Berg & Behrens (2014).

A.1 Gross anatomy

The cerebellum is an organ of the CNS located in the posterior cranial fossa, below the cerebrum, at the back of the brainstem and protected by the occipital bone (see Fig. A.1). The cerebellum represents about the 10% of the whole brain in terms of weight and volume, but, despite this, it contains up to about the 80% of all CNS neurons (Herrup & Kuemerle, 1997; Herculano-Houzel, 2009).

At the gross anatomical level, the cerebellum is a bilaterally symmetric structure. In the medio-lateral direction, it is divided into a central region called vermis (paleocerebellum) and two lateral hemispheres (neocerebellum). In the anterior-posterior direction, two major transversal fissures divide it into three regions called respectively anterior cerebellum, posterior cerebellum and flocculonodular lobe (archicerebellum) (Herrup & Kuemerle, 1997) (see Fig. A.2).

The cerebellar cortex is made of a tightly folded layer of GM. These folds exhibit a regular transversal arrangement; shallower fissures further divide the cerebellar surface into lobules, each of which comprises a variable number of finer ridges called folia. The

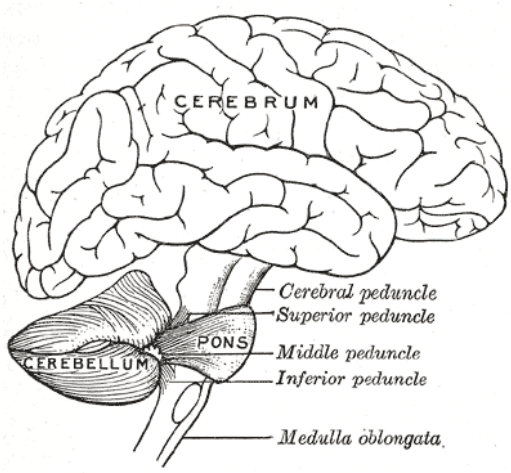

Fig. A.1: Anatomical illustration of the cerebellum and of its connections with the CNS. Image obtained from `https://commons.wikimedia.org/wiki/File:Gray677.png`, released into the public domain for any purpose and without any condition via Wikimedia Commons.

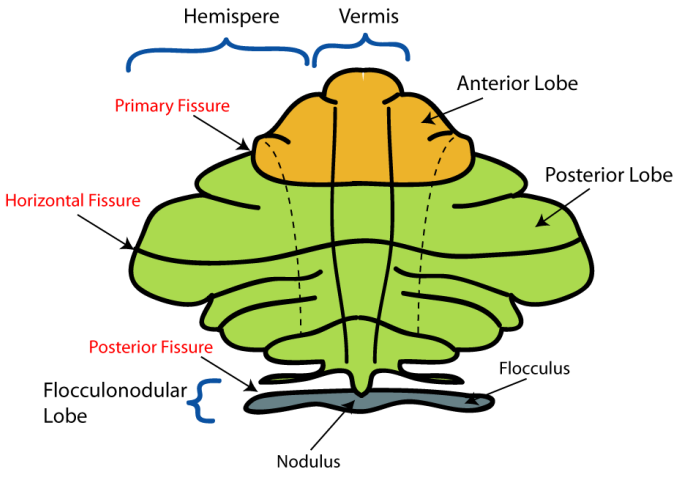

Fig. A.2: Illustration of the main divisions of the cerebellar cortex shown on the flattened cerebellum. Image obtained from `https://commons.wikimedia.org/wiki/File:CerebellumDiv.png`, released into the public domain for any purpose and without any condition via Wikimedia Commons.

cerebellar cortex is made from three layers: the molecular layer, the Purkinje cell layer and the granular layer.

Underneath the GM layers lies WM, which infiltrates lobules and folia and forms the arbor vitae. Embedded within the cerebellar WM are the DCN, GM structures called (from medial to lateral) fastigial, globose, emboliform and dentate nuclei. Globose and emboliform nuclei are often grouped and referred to as interposed nucleus. Three pairs of WM fibre bundles connect the cerebellum with the brainstem and, through this, with the cerebrum and the spinal cord. These are called cerebellar peduncles.

A.2 Cerebellar cyto-architecture

The cerebellar cortex is made of seven principal types of neuronal cells that are Purkinje cells, granule cells, Golgi cells, Lugaro cells, unipolar brush cells, basket cells and stellate cells (see Fig. A.3). Granule cells, Golgi cells, Lugaro cells and unipolar brush cells are found in the granular layer. Purkinje cells bodies form the thin Purkinje cell layer and their dendritic trees lie in the molecular layer. The molecular layer also contains stellate cells and unipolar brush cells.

The connectivity pattern of the cerebellum is relatively simple and stereotyped and it is repeated throughout its structure (D'Angelo & Casali, 2013). Mossy fibres and climbing fibres represent the two main channels through which inputs enter the cerebellum and they give rise to two main different signal pathways. Mossy fibres arise from several nuclei (including pontine nuclei, vestibular nuclei, brainstem reticular formation, and thalamic nuclei) and enter the cerebellum: there they diverge to form excitatory synapses with the DCN and to activate the granular layer of the cerebellar cortex. Each granule cell receives inputs from 4-5 mossy fibres. Each mossy fibre form excitatory synapses with hundreds of granule cells, which, in turn, send thin unmyelinated axons perpendicularly to the cerebellar cortex and toward its surface. In the molecular layer, these axons fork in two branches that run parallel to the cerebellar surface (parallel fibres) along the medio-lateral direction and form excitatory synaptic connections with dendritic trees of Purkinje cells. Golgi cells have inhibitory effects on granule cells, while inhibition to Purkinje cells is provided by stellate and basket cells in the molecular layer.

The inferior olivary nucleus is structure that lies in the medulla oblongata and collects inputs from the spinal cord, the brainstem and the cerebral cortex. It contains cell bodies of the second cerebellar input source: the climbing fibres. Climbing fibres enter the cerebellum and form excitatory projections with DCN and with Purkinje cells of the cerebral cortex.

Finally Purkinje cells send inhibitory projections to DCN. Therefore, both pathways terminate in the DCN, which are regulated by the described mechanisms and represent the major sources of output from the cerebellum. The only alternative output sources from the cerebellum are the vestibular nuclei (located in the medulla oblongata), which receive projections directly from the cortex of the flocculonodular lobe.

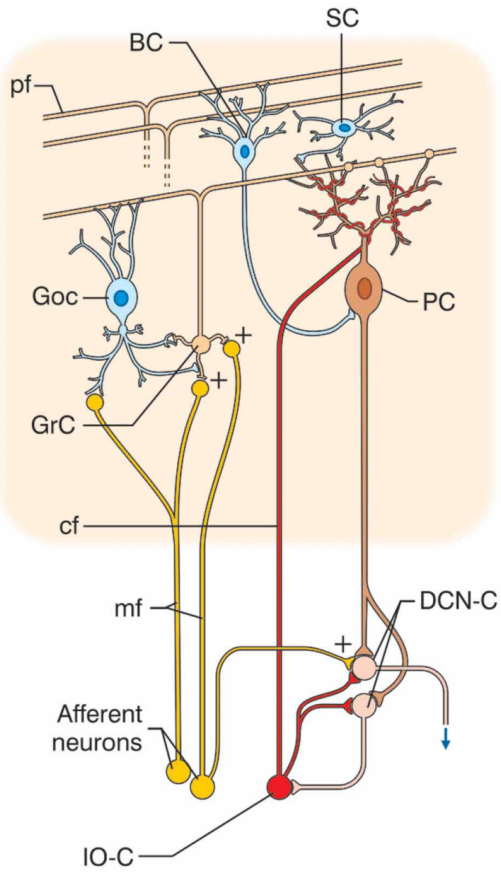

Fig. A.3: Classical view of cerebellar cyto-architecture. The principal types of neurons are displayed: granule cells (GrC), Golgi cells (GoC), Purkinje cells (PC), stellate and basket cells (SC, BC). Lugaro cells and unipolar brush cells are not shown here. mf: mossy fibres; cf: climbing fibres; pf: parallel fibres; IO: inferior olivary nucleus. Image obtained from D'Angelo & Casali (2013).

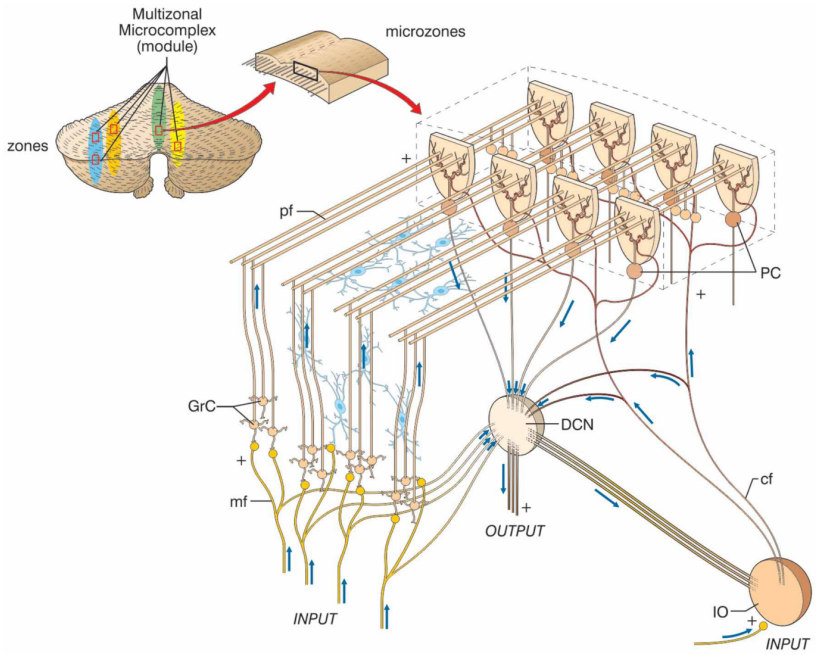

Fig. A.4: The modular organisation of the cerebellum. Image obtained from D'Angelo & Casali (2013).

A.3 Cerebellar connectivity

The cerebellum is organised in longitudinal connectivity modules (or microzones) that could be considered the cerebellar functional units (Apps & Hawkes, 2009) (see Fig. A.4). A microzone comprises a conglomerate of about 1000 Purkinje cells, which are arranged in a narrow rostro-caudally oriented strip of the cerebellar cortex. These cells share the same somatotopic receptive field, along with its corresponding olivo-cerebellar and cortico-nuclear connections. Purkinje cells within a microzone receive climbing fibres projections from a specific subregion of the inferior olivary nucleus. Then, the same Purkinje cells project to a specific region of DCN.

The plane identified by the cortical strip of Purkinje cells and the corresponding climbing fibre receptive field contains also the flattened Purkinje cell dendritic trees. Parallel fibres run perpendicularly to this plane and, therefore, they represent the main form of inter-modular communication.

Similarly to climbing fibres, mossy fibres projecting to Purkinje cells in a specific microzone through granule cells also project to the same DCN area that receives inputs from those Purkinje cells (D'Angelo & Casali, 2013). However, mossy fibres from a given source exhibit larger transverse branching with respect to climbing fibres and their terminal fields connect with multiple longitudinal zones.

Afferent and efferent fibres of the cerebellum are organised in three pairs of cerebellar peduncles. Efferent fibres from DCN make the superior cerebellar peduncles, WM

structures connecting the cerebellum to the midbrain. Superior cerebellar peduncles cross the midline at the level of the inferior colliculi and project to contralateral thalamus and red nucleus. The two major pathways running through these peduncles are the dentatorubrothalamocortical and the cerebellothalamocortical tracts. Middle cerebellar peduncles originate from the pontine nuclei and project to the contralateral hemisphere of the cerebellar cortex. They are part of the corticopontocerebellar tract, which carries information from the contralateral cerebral cortex to the cerebellum. Inferior cerebellar peduncles group afferent fibres carrying many types of inputs from the spinal cord and efferent fibres originating from the cortex of the cerebellar flocculonodular lobe and projecting to the vestibular nuclei. Afferent fibres included therein originate from the ipsilateral spinal cord and comprise the posterior spinocerebellar tract, the cuneocerebellar tract, the trigeminocerebellar tract and the vestibulocerebellar tract. These tracts are made of mossy fibres that project to the vermis and the flocculonodular lobe. Moreover, inferior cerebellar peduncles include also climbing fibres originating from the contralateral inferior olivary nucleus and forming the olivocerebellar tract.

The cerebellum is connected with the cerebrum through different bidirectional circuits, thus forming functional loops (see Fig. A.5). Efferent projections from the cerebellum are enclosed within the cerebellothalamocortical and the dentatorubrothalamocortical tracts. Through the thalamus, the cerebellum is connected with many cerebral cortical regions involved in motor, sensory and associative functions. These regions include the motor, premotor and somatosensory areas, the parietal cortex, the prefrontal cortex, the temporal cortex. Moreover it is connected to the basal ganglia and the limbic system and to the oculomotor system.

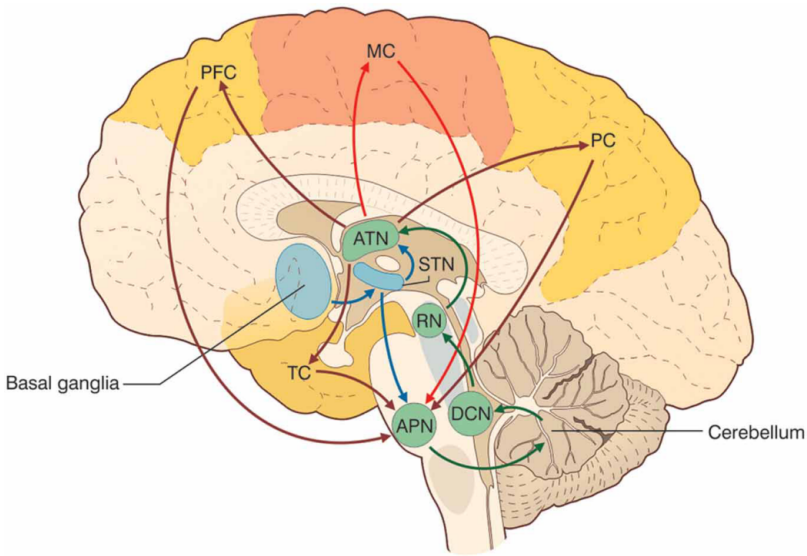

Fig. A.5: The cerebellothalamocortical and the dentatorubrothalamocortical pathways. STN: subthalamic nucleus; APN: anterior pontine nuclei; DCN: deep cerebellar nuclei; RN: red nucleus; ATN: anterior thalamic nucleus; MC: motor cortex; PFC: prefrontal cortex; PC: parietal cortex; TC: temporal cortex. Image obtained from D'Angelo & Casali (2013).

Bibliography

Andersson J. L. & Sotiropoulos S. N. 2016. An integrated approach to correction for off-resonance effects and subject movement in diffusion MR imaging. *NeuroImage*, **125**(jan), 1063–1078.

Andersson J. L. et al. 2003. How to correct susceptibility distortions in spin-echo echo-planar images: application to diffusion tensor imaging. *NeuroImage*, **20**(2), 870–888.

Apps R. & Hawkes R. 2009. Cerebellar cortical organization: a one-map hypothesis. *Nature Reviews Neuroscience*, **10**(9), 670–681.

Baizer J. S. 2014. Unique Features of the Human Brainstem and Cerebellum. *Frontiers in Human Neuroscience*, **8**(April), 1–17.

Basser P. J. & Pierpaoli C. 2011. Microstructural and physiological features of tissues elucidated by quantitative-diffusion-tensor MRI. *Journal of Magnetic Resonance*, **213**(2), 560–570.

Benedict R. H. B. et al. 2017. Validity of the Symbol Digit Modalities Test as a cognition performance outcome measure for multiple sclerosis. *Multiple Sclerosis Journal*, **23**(5), 721–733.

Bernstein M. A. et al. 2004. *Handbook of MRI pulse sequences*. Elsevier Academic Press.

Bianciardi M. et al. 2015. Toward an In Vivo Neuroimaging Template of Human Brainstem Nuclei of the Ascending Arousal, Autonomic, and Motor Systems. **5**(10), 597–607.

Boillat Y. et al. 2018. Surface-based characteristics of the cerebellar cortex visualized with ultra-high field MRI. *NeuroImage*, **172**(May 2017), 1–8.

Bonavita S. et al. 2015. Computer-aided cognitive rehabilitation improves cognitive performances and induces brain functional connectivity changes in relapsing remitting multiple sclerosis patients: An exploratory study. *Journal of Neurology*, **262**(1), 91–100.

Bonnet M. C. et al. 2010. Cognitive compensation failure in multiple sclerosis. *Neurology*, **75**, 1241–1248.

Bozzali M. et al. 2013. Anatomical brain connectivity can assess cognitive dysfunction in multiple sclerosis. *Multiple sclerosis (Houndmills, Basingstoke, England)*, **19**(9), 1161–8.

Braak H. & Braak E. 1983. Morphological studies of local circuit neurons in the cerebellar dentate nucleus of man. *Human neurobiology*, **2**(2), 49–57.

Brooks J. C. W. et al. 2013. Physiological Noise in Brainstem fMRI. *Frontiers in Human Neuroscience*, **7**(October), 1–13.

Brown R. W. et al. 2014a. *Magnetic resonance imaging : physical properties and sequence design*. Wiley.

Brown R. W. et al. 2014b. *Magnetic Resonance Imaging: Physical Principles and Sequence Design*. John Wiley & Sons Ltd.

Broyd S. J. et al. 2009. Default-mode brain dysfunction in mental disorders: A systematic review. *Neuroscience & Biobehavioral Reviews*, **33**(3), 279–296.

Buckner R. L. et al. 2008. The Brain's Default Network: Anatomy, Function, and Relevance to Disease. *Annals of the New York Academy of Sciences*, **1124**(1), 1–38.

Buckner R. L. et al. 2011. The organization of the human cerebellum estimated by intrinsic functional connectivity. *Journal of Neurophysiology*, **106**, 2322–2345.

Bullmore E. T. & Sporns O. 2009. Complex brain networks: graph theoretical analysis of structural and functional systems. *Nature reviews. Neuroscience*, **10**(3), 186–198.

Calamante F. et al. 2010. Track-density imaging (TDI): Super-resolution white matter imaging using whole-brain track-density mapping. *NeuroImage*, **53**(4), 1233–1243.

Canto C. B. et al. 2016. Whole-cell properties of cerebellar nuclei neurons in vivo. *PLoS ONE*, **11**(11), 1–19.

Caruyer E. et al. 2013. Design of multishell sampling schemes with uniform coverage in diffusion MRI. *Magnetic Resonance in Medicine*, **69**(6), 1534–1540.

Cercignani M. & Gandini Wheeler-Kingshott C. A. M. 2018. From micro- to macrostructures in multiple sclerosis: what is the added value of diffusion imaging. *NMR in Biomedicine*.

Cerminara N. L. et al. 2015. Redefining the cerebellar cortex as an assembly of non-uniform Purkinje cell microcircuits. *Nature Reviews Neuroscience*, **16**(2), 79–93.

Chard D. T. et al. 2010. Reducing the Impact of White Matter Lesions on Automated Measures of Brain Gray and White Matter Volumes. *Journal of Magnetic Resonance Imaging*, **32**, 223–228.

Chiaravalloti N. D. & DeLuca J. 2008. Cognitive impairment in multiple sclerosis. *The Lancet Neurology*, **7**(12), 1139–1151.

Christodoulou C. et al. 2003. Cognitive performance and MR markers of cerebral injury in cognitively impaired MS patients. *Neurology*, **60**(11), 1793–1798.

D'Angelo E. & Casali S. 2013. Seeking a unified framework for cerebellar function and dysfunction: from circuit operations to cognition. *Frontiers in Neural Circuits*, **6**(January), 1–23.

Dell'Acqua F. et al. 2013. MR Diffusion Histology and Micro-Tractography Reveal Mesoscale Features of the Human Cerebellum. *Cerebellum*, **12**, 923–931.

Deppe M. et al. 2015. Evidence for early, non-lesional cerebellar damage in patients with multiple sclerosis: DTI measures correlate with disability, atrophy, and disease duration. *Multiple Sclerosis Journal*, 1–12.

Diedrichsen J. et al. 2011a. Imaging the deep cerebellar nuclei : A probabilistic atlas and normalization procedure. *NeuroImage*, **54**, 1786–1794.

Diedrichsen J. et al. 2011b. Imaging the deep cerebellar nuclei: A probabilistic atlas and normalization procedure. *NeuroImage*, **54**(3), 1786–1794.

Diedrichsen J. 2006. A spatially unbiased atlas template of the human cerebellum. *Neuroimage*, **33**(1), 127–138.

Diedrichsen J. et al. 2009. A probabilistic MR atlas of the human cerebellum. *NeuroImage*, **46**(1), 39–46.

Dineen R. A. et al. 2009. Disconnection as a mechanism for cognitive dysfunction in multiple sclerosis. *Brain*, **132**(1), 239–249.

D'Mello A. M. & Stoodley C. J. 2015. Cerebro-cerebellar circuits in autism spectrum disorder. *Frontiers in Neuroscience*, **9**.

Dowell N. G. et al. 2009. Contiguous-slice zonally oblique multislice (CO-ZOOM) diffusion tensor imaging: Examples of in vivo spinal cord and optic nerve applications. *Journal of Magnetic Resonance Imaging*, **29**(2), 454–460.

Essen D. C. V. et al. 2013. The WU-Minn Human Connectome Project : An overview. *NeuroImage*, **80**, 62–79.

Fatemi S. H. et al. 2012. Consensus paper: Pathological role of the cerebellum in Autism. *Cerebellum*, **11**(3), 777–807.

Faull O. K. et al. 2015. Functional subdivision of the human periaqueductal grey in respiratory control using 7 tesla fMRI. *NeuroImage*, **113**, 356–364.

Feinberg D. A. et al. 1985. Inner volume MR imaging: technical concepts and their application. *Radiology*, **156**(3), 743–747.

Fischer H. & Ladebeck R. 1998. Echo-Planar Imaging Image Artifacts. *Pages 179–200 of: Echo-Planar Imaging*. Springer, Berlin, Heidelberg.

Forn C. et al. 2013. Analysis of "task-positive" and "task-negative" functional networks during the performance of the Symbol Digit Modalities Test in patients at presentation with clinically isolated syndrome suggestive of multiple sclerosis. *Experimental Brain Research*, **225**(3), 399–407.

Fukunaga M. et al. 2010. Layer-specific variation of iron content in cerebral cortex as a source of MRI contrast. *Proceedings of the National Academy of Sciences*, **107**(8), 3834–3839.

Glasser M. F. & Van Essen D. C. 2011. Mapping Human Cortical Areas In Vivo Based on Myelin Content as Revealed by T1- and T2-Weighted MRI. *The Journal of Neuroscience*, **31**(32), 11597–11616.

Glover G. H. et al. 2000. Image-based method for retrospective correction of physiological motion effects in fMRI: RETROICOR. *Magnetic Resonance in Medicine*, **44**(1), 162–167.

Granziera C. et al. 2009. Diffusion Spectrum Imaging Shows the Structural Basis of Functional Cerebellar Circuits in the Human Cerebellum In Vivo. *PLoS ONE*, **4**(4), 1–6.

Griffa A. et al. 2013. Structural connectomics in brain diseases. *NeuroImage*, **80**, 515–526.

Habas C. et al. 2009. Distinct Cerebellar Contributions to Intrinsic Connectivity Networks. *Journal of Neuroscience*, **29**(26), 8586–8594.

Hawellek D. J. et al. 2011. Increased functional connectivity indicates the severity of cognitive impairment in multiple sclerosis. *PNAS*, 1–7.

He Y. et al. 2009. Impaired small-world efficiency in structural cortical networks in multiple sclerosis associated with white matter lesion load. *Brain*, **132**, 3366–3379.

Herculano-Houzel S. 2009. The human brain in numbers: a linearly scaled-up primate brain. *Frontiers in Human Neuroscience*, **3**, 1–11.

Herrup K. & Kuemerle B. 1997. The compartmentalization of the cerebellum. *Annual review of neuroscience*, **20**, 61–90.

Hulst H. E. et al. 2013. Cognitive impairment in MS: Impact of white matter integrity, gray matter volume, and lesions. *Neurology*, **80**, 1025–1032.

Inglese M. 2006. Multiple Sclerosis : New Insights and Trends. *American Journal of Neuroradiology*, **27**(5), 954–957.

Jacobs H. I. L. et al. 2018. The cerebellum in Alzheimer's disease: evaluating its role in cognitive decline. *Brain*, **141**, 37–47.

Jenkinson M. et al. 2012. Fsl. *NeuroImage*, **62**(2), 782–790.

Jensen J. H. & Helpern J. A. 2010. MRI quantification of non-Gaussian water diffusion by kurtosis analysis. *NMR in Biomedicine*, **23**(7), 698–710.

Jensen J. H. et al. 2005. Diffusional kurtosis imaging: The quantification of non-Gaussian water diffusion by means of magnetic resonance imaging. *Magnetic Resonance in Medicine*, **53**(6), 1432–1440.

Johansen-Berg H. & Behrens T. E. J. 2014. *Diffusion MRI : from quantitative measurement to in vivo neuroanatomy*. Elsevier Academic Press.

Jones D. K. 2010. *Diffusion MRI : theory, methods, and applications*. Oxford University Press.

Jones D. K. et al. 2013. White matter integrity, fiber count, and other fallacies: The do's and don'ts of diffusion MRI. *NeuroImage*, **73**(jun), 239–254.

Kaiser M. 2011. A tutorial in connectome analysis: Topological and spatial features of brain networks. *NeuroImage*, **57**(3), 892–907.

Koziol L. F. et al. 2014. Consensus Paper : The Cerebellum' s Role in Movement and Cognition. *Cerebellum*, **13**, 151–177.

Krienen F. M. & Buckner R. L. 2009. Segregated fronto-cerebellar circuits revealed by intrinsic functional connectivity. *Cerebral Cortex*, **19**, 2485–2497.

Küper M. et al. 2011. Evidence for a motor and a non-motor domain in the human dentate nucleus — An fMRI study. *NeuroImage*, **54**(4), 2612–2622.

Küper M. et al. 2012. Structural and Functional Magnetic Resonance Imaging of the Human Cerebellar Nuclei. *Cerebellum*, **11**, 314–324.

Kutzelnigg A. et al. 2005. Cortical demyelination and diffuse white matter injury in multiple sclerosis. *Brain*, **128**(11), 2705–2712.

Llufriu S. et al. 2017. Structural networks involved in attention and executive functions in multiple sclerosis. *NeuroImage: Clinical*, **13**, 288–296.

Lorio S. et al. 2016. New tissue priors for improved automated classification of subcortical brain structures on MRI. *NeuroImage*, **130**(apr), 157–166.

Louapre C. et al. 2014. Brain networks disconnection in early multiple sclerosis cognitive deficits: An anatomofunctional study. *Human Brain Mapping*, **35**(9), 4706–4717.

Lublin F. D. & Reingold S. C. 1996. Defining the clinical course of multiple sclerosis: Results of an international survey. *Neurology*, **46**(4), 907–911.

Marques J. P. et al. 2010. Cerebellar cortical layers: in vivo visualization with structural high-field-strength MR imaging. *Radiology*, **254**(3), 942–948.

Menon V. 2011. Large-scale brain networks and psychopathology : a unifying triple network model. *Trends in Cognitive Sciences*, **15**(10), 483–506.

Mori S. S. & Tournier J.-D. 2014. *Introduction to diffusion tensor imaging and higher order models*. Elsevier Academic Press.

Moroso A. et al. 2017a. Microstructural analyses of the posterior cerebellar lobules in relapsing-onset multiple sclerosis and their implication in cognitive impairment. *PLoS ONE*, 1–15.

Moroso A. et al. 2017b. Posterior lobules of the cerebellum and information processing speed at various stages of multiple sclerosis. *Journal of Neurology, Neurosurgery and Psychiatry*, **88**, 146–151.

Muhlert N. et al. 2013. Diffusion MRI-based cortical complexity alterations associated with executive function in multiple sclerosis. *Journal of magnetic resonance imaging*, **38**(1), 54–63.

Novellino F. et al. 2016. Cerebellar involvement in Essential Tremor with and without resting tremor: a Diffusion Tensor Imaging study. *Parkinsonism and Related Disorders*, **27**, 61–66.

O'Reilly J. X. et al. 2010. Distinct and overlapping functional zones in the cerebellum defined by resting state functional connectivity. *Cerebral Cortex*, **20**, 953–965.

Pagani E. et al. 2005. A method for obtaining tract-specific diffusion tensor MRI measurements in the presence of disease: Application to patients with clinically isolated syndromes suggestive of multiple sclerosis. *NeuroImage*, **26**(1), 258–265.

Palesi F. et al. 2015. Contralateral cerebello-thalamo-cortical pathways with prominent involvement of associative areas in humans in vivo. *Brain Structure and Function*, **220**(6), 3369–3384.

Palesi F. et al. 2017. Contralateral cortico-ponto- cerebellar pathways reconstruction in humans in vivo: implications for reciprocal cerebro-cerebellar structural connectivity in motor and non-motor areas. *Scientific reports*, 1–13.

Pardini M. et al. 2014. Network Efficiency As A Final Common Pathway For Cognitive Deficits In Multiple Sclerosis: A Single Network Graph Theory Study (P6.128). *Neurology*, **82**(10 Supplement).

Pardini M. et al. 2015. Motor network efficiency and disability in multiple sclerosis. *Neurology*.

Parmenter B. a. et al. 2007. Screening for cognitive impairment in multiple sclerosis using the Symbol digit Modalities Test. *Multiple sclerosis (Houndmills, Basingstoke, England)*, **13**(1), 52–7.

Pattinson K. T. S. et al. 2009. Opioids Depress Cortical Centers Responsible for the Volitional Control of Respiration. *The Journal of Neuroscience*, **29**(25), 8177–8186.

Paul T. Callaghan. 1993. *Principles of nuclear magnetic resonance microscopy.* Oxford: Oxford University Press.

Port J. D. & Pomper M. G. 2000. Quantification and Minimization of Magnetic Susceptibility Artifacts on GRE Images. *Journal of Computer Assisted Tomography*, **24**(6), 958–964.

Powell E. et al. 2018. Edge Weights and Network Properties in Multiple Sclerosis. *Pages 1–8 of: Medical Image Computing and Computer-Assisted Intervention – MICCAI 2018*.

Ramnani N. 2006. The primate cortico-cerebellar system: Anatomy and function. *Nature Reviews Neuroscience*, **7**, 511–522.

Ramnani N. et al. 2006. The evolution of prefrontal inputs to the cortico-pontine system: Diffusion imaging evidence from macaque monkeys and humans. *Cerebral Cortex*, **16**, 811–818.

Rao S. M. et al. 2014. Correlations between MRI and Information Processing Speed in MS : A Meta-Analysis. *Multiple Sclerosis International*, **2014**.

Ristanović D. et al. 2010. Morphology and classification of large neurons in the adult human dentate nucleus: A qualitative and quantitative analysis of 2D images. *Neuroscience Research*, **67**(1), 1–7.

Rocca M. A. et al. 2007. Altered functional and structural connectivities in patients with MS: A 3-T study. *Neurology*, **69**(23), 2136–2145.

Rocca M. A. et al. 2010. Default-mode network dysfunction and cognitive impairment in progressive MS. *Neurology*, **74**(16), 1252–1259.

Romascano D. et al. 2015. Multicontrast connectometry: A new tool to assess cerebellum alterations in early relapsing-remitting multiple sclerosis. *Human Brain Mapping*, **36**(4), 1609–1619.

Roosendaal S. D. et al. 2009. Regional DTI differences in multiple sclerosis patients. *NeuroImage*, **44**(4), 1397–1403.

Roosendaal S. D. et al. 2010. Resting state networks change in clinically isolated syndrome. *Brain*, **133**(6), 1612–1621.

Rubinov M. & Sporns O. 2010. Complex network measures of brain connectivity: uses and interpretations. *NeuroImage*, **52**(3), 1059–69.

Rudick R. A. et al. 1999. Use of the brain parenchymal fraction to measure whole brain atrophy in relapsing-remitting MS. Multiple Sclerosis Collaborative Research Group. *Neurology*, **53**(8), 1698–704.

Schmahmann J. D. 2010. The Role of the Cerebellum in Cognition and Emotion: Personal Reflections Since 1982 on the Dysmetria of Thought Hypothesis, and Its Historical Evolution from Theory to Therapy. *Neuropsychology Review*, **20**(3), 236–260.

Schmitt F. et al. 1998. *Echo-Planar Imaging: Theory, Technique and Application*. Springer-Verlag Berlin Heidelberg.

Schoonheim M. M. et al. 2015. Network collapse and cognitive impairment in multiple sclerosis. *Frontiers in Neurology*, **6**(April), 1–5.

Sclocco R. et al. 2017. Challenges and opportunities for brainstem neuroimaging with ultrahigh field MRI. *NeuroImage*, 1–15.

Setsompop K. et al. 2012. Blipped-controlled aliasing in parallel imaging for simultaneous multislice echo planar imaging with reduced g-factor penalty. *Magnetic resonance in medicine : official journal of the Society of Magnetic Resonance in Medicine / Society of Magnetic Resonance in Medicine*, **67**(5), 1210–24.

Shu N. et al. 2011. Diffusion Tensor Tractography Reveals Disrupted Topological Efficiency in White Matter Structural Networks in Multiple Sclerosis. *Cerebral Cortex*, **21**, 2565–2577.

Shu N. et al. 2016. Disrupted topological organization of structural and functional brain connectomes in clinically isolated syndrome and multiple sclerosis. *Scientific Reports*, 1–11.

Smith A. 1982. Symbol digit modalities test (SDMT) manual (revised) Western psychological services. *Los Angeles*.

Smith S. M. et al. 2004. Advances in functional and structural MR image analysis and implementation as FSL. *NeuroImage*, **23**(jan), S208–S219.

Smith S. M. et al. 2009. Correspondence of the brain's functional architecture during activation and rest. *Proceedings of the National Academy of Sciences of the United States of America*, **106**(31), 13040–5.

Sokolov A. A. et al. 2017. The Cerebellum: Adaptive Prediction for Movement and Cognition. *Trends in Cognitive Sciences*, **21**(5), 313–332.

Stankiewicz J. M. et al. 2011. Brain MRI Lesion Load at 1.5T and 3T versus Clinical Status in Multiple Sclerosis. *Journal of Neuroimaging*, **21**(2), 50–56.

Steele C. et al. 2016. Human Cerebellar Sub-millimeter Diffusion Imaging Reveals the Motor and Non-motor Topography of the Dentate Nucleus. *Cerebral Cortex*, 1–12.

Stoodley C. J. 2014. Distinct regions of the cerebellum show gray matter decreases in autism, ADHD, and developmental dyslexia. *Frontiers in Systems Neuroscience*, **8**.

Stoodley C. J. & Schmahmann J. D. 2010. Evidence for topographic organization in the cerebellum of motor control versus cognitive and affective processing. *Cortex*, **46**(7), 831–844.

Strick P. L. et al. 2009. Cerebellum and nonmotor function. *Annual Review of Neuroscience*, **32**, 413–434.

Strober L. et al. 2009. Sensitivity of conventional memory tests in multiple sclerosis: comparing the Rao Brief Repeatable Neuropsychological Battery and the Minimal Assessment of Cognitive Function in MS. *Multiple sclerosis (Houndmills, Basingstoke, England)*, **15**(9), 1077–1084.

Sumowski J. F. et al. 2010. Intellectual enrichment is linked to cerebral efficiency in multiple sclerosis : functional magnetic resonance imaging evidence for cognitive reserve. *Brain*, **133**, 362–374.

Symms M. 2000. Zonally-magnified oblique multislice (ZOOM) EPI. *Proceedings of the 8th Annual Meeting of the ISMRM*, **8**, 2000.

Tedesco A. M. et al. 2011. The cerebellar cognitive profile. *Brain*, **134**(12), 3669–3683.

Tellmann S. et al. 2015a. Cytoarchitectonic mapping of the human brain cerebellar nuclei in stereotaxic space and delineation of their co-activation patterns. *Frontiers in Neuroanatomy*, **09**(May), 1–14.

Tellmann S. et al. 2015b. Cytoarchitectonic mapping of the human brain cerebellar nuclei in stereotaxic space and delineation of their co-activation patterns. *Frontiers in Neuroanatomy*, **9**, 1–14.

Tournier J.-D. et al. 2007. Robust determination of the fibre orientation distribution in

diffusion MRI: Non-negativity constrained super-resolved spherical deconvolution. *NeuroImage*, **35**(4), 1459–1472.

Tournier J.-D. et al. 2012. MRtrix: Diffusion tractography in crossing fiber regions. *International Journal of Imaging Systems and Technology*, **22**(1), 53–66.

Tukey J. W. 1977. *Exploratory data analysis*. Vol. 2. Reading, Mass.

Valentino P. et al. 2009. Cognitive deficits in multiple sclerosis patients with cerebellar symptoms. *Multiple Sclerosis*, **15**(December 2008), 854–859.

van Baarsen K. M. et al. 2016. A probabilistic atlas of the cerebellar white matter. *NeuroImage*, **124**, 724–732.

Van Schependom J. et al. 2014. The Symbol Digit Modalities Test as sentinel test for cognitive impairment in multiple sclerosis. *European Journal of Neurology*, **21**(9), 1219–1225.

Veraart J. et al. 2013. Weighted linear least squares estimation of diffusion MRI parameters: Strengths, limitations, and pitfalls. *NeuroImage*, **81**, 335–346.

Voogd J. 2003. The human cerebellum. *Journal of Chemical Neuroanatomy*, **26**(4), 243–252.

Voogd J. 2011. Cerebellar zones: A personal history. *Cerebellum*, **10**(3), 334–350.

Wargo C. J. et al. 2013. A comparison and evaluation of reduced-FOV methods for multi-slice 7T human imaging. *Magnetic Resonance Imaging*, **31**(8), 1349–1359.

Weier K. et al. 2014. Cerebellar abnormalities contribute to disability including cognitive impairment in multiple sclerosis. *PLoS ONE*, **9**(1).

Weier K. et al. 2015. The Role of the Cerebellum in Multiple Sclerosis. *Cerebellum*, **14**(3), 364–374.

Werring D. J. et al. 1999. Diffusion tensor imaging of lesions and normal-appearing white matter in multiple sclerosis. *Neurology*, **52**(8), 1626–32.

Wheeler-Kingshott C. a. M. et al. 2002. ADC mapping of the human optic nerve: Increased resolution, coverage, and reliability with CSF-suppressed ZOOM-EPI. *Magnetic Resonance in Medicine*, **47**, 24–31.

Wilm B. J. et al. 2009. Diffusion-weighted imaging of the entire spinal cord. *NMR in Biomedicine*, **22**(2), 174–181.

Wu T. & Hallett M. 2013. The cerebellum in Parkinson's disease. *Brain*, **136**(3), 696–709.

Yamaguchi K. & Goto N. 1997. Three-dimensional structure of the human cerebellar dentate nucleus: a computerized reconstruction study. *Anatomy and Embriology*, **196**, 343–348.

Yeo B. T. et al. 2011. The organization of the human cerebral cortex estimated by intrinsic functional connectivity. *Journal of neurophysiology*, **106**, 1125–1165.

Zhao L. et al. 2016. Cerebellar microstructural abnormalities in bipolar depression and unipolar depression: A diffusion kurtosis and perfusion imaging study. *Journal of Affective Disorders*, **195**, 21–31.

Zhou F. et al. 2014. Altered inter-subregion connectivity of the default mode network in relapsing remitting multiple sclerosis: A functional and structural connectivity study. *PLoS ONE*, **9**(7).

Zigmond A. S. & Snaith R. P. 1983. The Hospital Anxiety and Depression Scale. *Acta*

Psychiatrica Scandinavica, **67**(6), 361–370.

List of Publications

The work of this thesis and my involvement in the labs of Prof. D'Angelo (University of Pavia, Italy) and Prof. Gandini Wheeler-Kingshott (University of Pavia, Italy and UCL, UK) has led to the following scientific contributions.

Refereed publications

G. Castellazzi, S. D. Bruno, A. T. Toosy, L. Casiraghi, F. Palesi, **G. Savini**, E. D'Angelo and C. A. M. Gandini Wheeler-Kingshott. Prominent changes in cerebro-cerebellar functional connectivity during continuous cognitive processing, *Frontiers in Cellular Neuroscience*, 2018,12:331. doi: 10.3389/fncel.2018.00331

L. Casiraghi, A. A. S. Alahmadi, A. Monteverdi, F. Palesi, G. Castellazzi, **G. Savini**, K. Friston, C. A. M. Gandini Wheeler-Kingshott and E. D'Angelo. I see your effort: force-related BOLD effects in an extended action execution-observation network involving the cerebellum, *Cerebral Cortex*, in press.

Publications under review

G. Savini, M. Pardini, G. Castellazzi, A. Lascialfari, D. Chard, E. D'Angelo and C. A. M. Gandini Wheeler-Kingshott. Default mode network structural integrity and cerebellar connectivity predict information processing speed deficit in multiple sclerosis.

V. Nath, K. G. Schilling, A. E. Hainline, Y. Huo, P. Parvathaneni, J. A. Blaber, M. Rowe, P. Rodrigues, V. Prchkovska, D. B. Aydogan, W. Sun, Y. Shi, W. A. Parker, A. A. O. Ismail, R. Verma, R. P. Cabeen, A. W. Toga, A. T. Newton, J. Wasserthal, P. Neher, K. Maier-Hein, **G. Savini**, F. Palesi, E. Kaden, Y. Wu, J. He, Y. Fen, M. Barakovic, D. Romascano, J. Rafael-Patino, M. Frigo, G. Girard, A. Daducci, J. P. Thiran, M. Paquette, F. Rheault, J. Sidhu, C. Lebel, A. Leemans, M. Descoteaux, T. B. Dyrby and B. A. Landman. Tractography Reproducibility Challenge with Empirical Data (TraCED): The 2017 ISMRM Diffusion Study Group Challenge .

Publications in preparation

G. Savini, S. Marchese, F. Palesi, L. Casiraghi, G. Castellazzi, A. Lascialfari, E. D'Angelo and C. A. M. Gandini Wheeler-Kingshott. Exploratory study of cerebellar microstructure with diffusion MRI.

S. Marchese, F. Palesi, **G. Savini**, E. De Vita, E. D'Angelo and C. A. M. Gandini Wheeler-Kingshott. Characterisation and reproducibility of cerebellar metabolites in crus I-II using MRS.

Indexed proceedings

G. Savini, F. Palesi, G. Castellazzi, L. Casiraghi, F. Grussu, A. Lascialfari, E. D'Angelo and C. A. M. Gandini Wheeler-Kingshott. Investigation of cerebellar microstructure with two-compartment Spherical Mean Technique and T1w/T2w myelin weighting, *Frontiers in Cellular Neuroscience*, 2017. doi: 10.3389/conf.fncel.2017.37.000026

F. Palesi, F. Calamante, **G. Savini**, G. Castellazzi, E. D'Angelo and C. A. M. Gandini Wheeler-Kingshott. Characterization of cerebro-cerebellar structural connections using high-quality diffusion MRI data, *Frontiers in Cellular Neuroscience*, 2017.
doi: 10.3389/conf.fncel.2017.37.000032

Presentations at conferences and schools

G. Savini, F. Fasano, J. Whittaker, L. Casiraghi, F. Palesi, G. Castellazzi, A. Lascialfari, E. D'Angelo, D. Jones, R. Wise and C. A. M. Gandini Wheeler-Kingshott. Distortion-matched high-resolution reduced-FoV functional and diffusion MRI of the human brainstem at 7T, *Joint Annual Meeting ISMRM-ESMRMB 2018*, Paris, France (e-poster).

G. Savini, F. Palesi, G. Castellazzi, L. Casiraghi, F. Grussu, A. Lascialfari, E. D'Angelo and C. A. M. Gandini Wheeler-Kingshott. Characterisation of cerebellar microstructure with two-compartment Spherical Mean Technique, *ISMRM 25$^{\text{th}}$ Annual Meeting 2017*, Honolulu, Hawai'i, USA (oral presentation).

G. Savini, F. Palesi, G. Castellazzi, L. Casiraghi, F. Grussu, A. Lascialfari, E. D'Angelo and C. A. M. Gandini Wheeler-Kingshott. Investigation of cerebellar microstructure with two-compartment Spherical Mean Technique and T1w/T2w myelin weighting, *School of Brain Cells & Circuits "Camillo Golgi" 2016 - The cerebellum inside-out: cells, circuits and functions*, Erice, Italy (poster).

G. Savini, M. Pardini, A. Lascialfari, D. Chard, D. Miller, E. D'Angelo and C. A. M. Gandini Wheeler-Kingshott. Cerebellar-cerebral connections with the default mode network influence working memory performance in MS. *ISMRM 24$^{\text{th}}$ Annual Meeting 2016*, Singapore (oral presentation).

G. Savini, M. Pardini, A. Lascialfari, D. Chard, D. Miller, E. D'Angelo and C. A. M. Gandini Wheeler-Kingshott. Cerebellar-cerebral connections with the default mode network influence working memory performance in MS. *ISMRM Italian Chapter 7$^{\text{th}}$ Annual Meeting 2016*, Bologna, Italy (oral presentation).